Realization of a spin-1 Bose-Einstein condensation experiment

by

Daniel Benedicto-Orenes

A thesis submitted to
The University of Birmingham
for the degree of
DOCTOR OF PHILOSOPHY

Ultracold Atoms Group
School of Physics and Astronomy
College of Engineering and Physical Sciences
The University of Birmingham

Sep 2017

Abstract

This thesis is devoted to the construction, optimization and characterization of an experimental apparatus, capable of creating spinor condensates of $\simeq 1 \times 10^5$ atoms with a repetition rate of 10s, using an all-optical evaporation technique. I report a complete description of the experimental apparatus and techniques used in the experiment and a characterization of the BEC sample. We study the transmission of absorption imaging pictures through a coherent fiber bundle. We show that the fiber bundle introduces spurious noise in the picture mainly due to the strong core-to-core coupling. We demonstrate that we can retrieve exact quantitative information about the atomic system using this technique. We also explore the equilibration dynamics of ferromagnetic spin-1system as a function of the initial magnetization of the sample and the external magnetic field. We show that the magnetization of the system is conseverd despite of the presence of dissipative processes that are intrinsic to any experiment. We investigated the formation of the BEC in a spin-1 quantum gas in the presence of an external magnetic field. We report on the spontaneous magnetization of the condensate fraction during the evaporation process at low magnetic fields. We as well observe multi-step condensation, and found signatures of a possible interspecies Feshbach resonance.

ACKNOWLEDGEMENTS

Before the reader starts putting up with my terrible writing style and shares all these four years of suffering which I hope will be reflected in this work, I would like to take the opportunity to acknowledge all the people that, in different ways, have supported me over these years, and inspired me to become a better person. To start with, I want to thanks Professor Kai Bongs for giving me the opportunity to join this project. Dr. Anna Kowalczyk, for being one of my pillars through these years. Without her support and patience, I would not have learned many things. She will keep inspiring me to work hard and keep trying no matter how desperate the situation looks like. I enjoyed every minute working with you, although I am not sure if it was the most efficient approach :-) I am want to thanks to Dr. Giovanni Barontini. Although he joined us later, during the last two years he has become a great supervisor. Without his guidance and stimulating comments the author, probably, would not be able to present this work. Last but not least, I would like to thank my collegue Jaime, who joined us three months ago, and started to work hard from the beginning, helping me to keep the experiment running smoothly during my writing up time.

On the personal side, I want to tremendously thanks my parents for educating and loving me endlessly. Obviously, also to my sister and brother, that I have missed each and every minute that I have spent away from home. Big thanks to my friend Rocío, for putting up with my mood, every time I see one of your e-mails in the inbox folder, I smile. She has remained close, despite being far away.

To Thaïs, my partner, the most unexpected and pleasant part of this journey. The best is yet to come...

CONTENTS

LIST OF FIGURES

LIST OF TABLES

INTRODUCTION

At temperatures close to the absolute zero, the wave nature of particles becomes apparent and quantum mechanics plays a dominant role. In this regime, bosonic particles occupy macroscopically the lowest energy state and a phase transition to the Bose-Einstein condensate occurs. Below the critical temperature (T_c) of such transition the dynamic presents coherence and collective behaviour, and the condensate can be described by a macroscopic wave-function that is given by the product of N identical single-particle wave-functions in their ground state, $\Phi(\vec{x}) = \prod_i \phi_i(\vec{x})$. This scalar function characterizes the condensed phase of the system, and it is zero above T_c.

The experimental realization of Bose-Einstein condensates was pursuit for many years since the early 1970's, especially in liquid Hydrogen, but it was not finally achieved until 1995 by [1] and [2] in dilute atomic gases of Rubidium and Sodium respectively, and in Hydrogen finally in 1998 [3]. These first experimental realizations of Bose-Einstein condensation were possible in dilute atomic gases due to the advances carried out in the 1980's in the field of laser cooling and magnetic trapping of neutral atoms. The first manipulation of suspended particles using radiation pressure is due to A.Ashkin in 1970 [4], and the first observation of optically trapped atoms was at Bell laboratories [5] in 1986. These advances are summarized and historically reviewed in the Nobel lectures given by S.Chu [6], C.Cohen-Tanoudjii [7] and William E.phillips [8] in 1998 and by W.Ketterle [9] later in 2002. It is important to emphasize the work of Pritchard in the study of collisions and relaxation processes in these cold atomic systems. It allowed to understand and optimize the cooling process for different atomic species. Multicomponent condensates started to be investigated in 1997 at Jila [10], where two Bose-Einstein condensates of ^{87}Rb particles in different hyperfine states of the $F = 1$ and $F = 2$ manifold where mixed [11]. Unlike magnetic traps, optical traps are not sensitive to the magnetic sublevels of the atoms, and condensation can be achieved using only optical means [12]. This allows the formation of spinor condensates, with a richer physical picture due to the interplay between the different componenets of the system. Indeed, if the particles within the condensate belong to different states, they can not be described by the same particle wave-function. In case these condensates possess an internal degree of freedom they are called *spinor condensates* and their wave-function is a spherical tensor in spin space [13, 14].

Thesis overview

This thesis describes the steps that I have followed to build an experimental apparatus to study spinor condensates of ^{87}Rb atoms. At the time I started working in this project, the research direction was set towards the construction of an experimental setup to produce spinor Bose-Einstein condensates of ^{87}Rb atoms in ultra-low magnetic fields ($\sim$nT), aiming to look for signatures of magnetic dipole-dipole interactions (DDI) [15–18]. DDI are due to the permanent magnetic moment of alkali atoms and present interesting properties such as long-range order and anisotropy [19]. The magnetic DDI energy can be expressed as:

$$U_{dd} = A_{dd}\frac{\vec{F}_1 \cdot \vec{F}_2 - 3(\vec{F}_1 \cdot \hat{r})(\vec{F}_2 \cdot \hat{r})}{(\vec{r} \cdot \vec{r})^{3/2}} \tag{1}$$

where A_{dd} is a constant which depends on the atomic specie. $\vec{F}_{1,2}$ are the spin vectors of two interacting particles, and $\vec{r}$ is the relative position vector between the two. The need to work in such ultra-low magnetic field regime arises because ^{87}Rb possess a small permanent magnetic moment of $\mu = 1\mu_B$ compared with other species like Dy($\mu = 10\mu_B$) or Er ($\mu = 7\mu_B$). Therefore, the effects of the DDI interactions ($\sim h \times 1$Hz) are completely ruled out by the Zeeman shift of the levels in the presence of a non zero magnetic field ($\simeq h \times 7 \times 10^9$ Hz/T).

The process of building an experimental apparatus to produce spinor BEC in ultra-low magnetic fields was really challenging. The system had to be designed according to stringent constrains, for example the materials of the vacuum chamber and the optical elements surrounding the chamber had to be non-magnetic, and special fibers with non-magnetic connectors were purchased. Additionally, a custom science cell was bought with a long arm ($\approx$ 30cm) capable of accomodating several layers of $\mu-$metal shielding around it. All these special features of our system have consequences on the planification of light delivery to the experiment, the accommodation of a compatible imaging system in a reduced space and many other technical considerations. Shortly after the project started, Bose-Einstein condensation of Dy and Er atoms were achieved [20, 21]. These species are more suitable to study dipolar effects in quantum degenerate gases than ^{87}Rb , due to their larger magnetic moment. Another major event during the time I spent in this project was a change of supervisor. Dr. Giovanni Barontini become the PI in our project. Although the goal of building a state of the art experiment to produce spinor condensates persisted, due to the advances that other groups had in cooling highly magnetic species, the research direction was modified. The main focus is now on the spinor dynamics of the system, and we are looking at implementing a Digital Mirror Device (DMD) to imprint different phases on the the condensate to study vortex dynamics and use the system as a simulator of complex quantum processes.

The setup comprises a double 2D-3D MOT system to collect and pre-cool the atoms in the glass cell before they are loaded into the dipole trap. The path towards quantum degeneracy is all-optical, and exploits a crossed dipole trap. The all-optical technique and the use of a glass cell permits to have a good optical access. This gives our experiment the flexibility to accomodate different optical elements around it, such as high resolution imaging optics. New experimental paths can be implemented quickly and with simplicity.

The second part of the thesis is dedicated to present the first experimental results obtained with the setup that I built. Within the spirit of the first experimental proposal, we have investigated the transmission of absorption imaging pictures through a fiber bundle. Additionally we have explored the thermalization dynamics and the formation of spontaneous magnetization in ferromagnetic spin-1 systems in presence of an external magnetic field.

The thesis is organized in the following way:

- To put our research into context and provide the necessary theoretical background to understand the techniques and results presented through this thesis, **Chapter 1** reviews the mean field description of weakly interacting Bose-Einstein condensates, and its generalization to the multicomponent spin-1 case.

- **Chapter 2** contains the detailed description of the experimental setup that I built, and all the techniques that I have used to create a Bose-Einstein condensate. I will describe the vacuum system, the computer control that I have implemented, the laser systems and the detection scheme. A brief overview of the laser cooling theory is also presented here.

- In **Chapter 3** I present the experimental sequence for the realization of spin-1 Bose-Einstein condensates of ^{87}Rb . This represents the fundamental milestone of my thesis work and it is the starting point for all subsequent results achieved. I will present and discuss the evaporation in the crossed beam configuration and I dedicate the last section to present and discuss the most important measurements that characterize the BEC.

- **Chapter 4** is dedicated to the first results obtained with this experimental setup: an investigation of the transmission of absorption images of the BEC through a fiber bundle.The contents of this chapter have been published in [22].

- **Chapter 5** contains the results of our investigation of the equilibrium state of a ferromagnetic spin-1 system in an external magnetic field. The study of the thermalization properties of the system is

importat to confirm that we are accessing the true equilibrium state, and it has been investigated with detail.

- In **Chapter 6** I will present the preliminary investigation of the spontaneous magnetization of a spin-1 ^{87}Rb condensate in an external magnetic field. We have investigated the process of the BEC formation during the forced evaporation when this is realized in the presence of an external magnetic field up to $\simeq$ 40G. Although preliminary, we have already observed some interesting phenomena that will be subject to further investigations.

CHAPTER 1

THEORETICAL BACKGROUND

Spinor quantum gases are characterized by possesing an internal degree of freedom, which corresponds to the orientation of the spin. As a consequence, the order parameter describing the system is not a scalar but a multicomponent or vectorial order parameter. Under rotations, they transform according to the laws of the symmetry group they belong to. This means that the particle number of each substate is not fixed, offering a richer dynamics than the scalar condensates. They also differ from multicomponent quantum gases. The latter ones are formed of Bose-Einstein condensates in different hyperfine manifolds [23], with different species [24], or even condensates formed in spatially separated locations which are later brought together [25]. In atomic Bose-Einstein condensates, spinorial samples are typically created by forming the condensate in all the different Zeeman substates of the corresponding hyperfine manifold. The non-linear and complex coupling induced by the interactions between the different hyperfine substates introduces interesting properties to the dynamics, and the enhancement of the interaction energy due to the macroscopic occupation of the ground state can compete with the kinetic energies that usually dominate the behaviour of such systems.

Since the achievement of Bose-Einstein condensation in 1995 [26], the study of spinor condensates was a natural next step to follow. Early theoretical work are the seminal papers from Ho [27] and Ohmi and Machida [28]. More theoretical work on spinor BECs can be found in [29, 30]. The experimental work on spinor condensates was first stablished at MIT, where they studied the spin-domain dynamics of a Spin-1 condensate [31–33] creating magnetically trapped condensates of Na atoms which were later transfered into an optical dipole trap. Spin domain dynamics was further studied theoretically [34, 35] and experimentally [36–38]. These systems provide a good ground to study non-equilibrium physics [39–42]. The realization of higher spin-F quantum gases have been achieved for spin-2 using ^{87}Rb in the $|F = 2\rangle$ hyperfine manifold [43], and spin-3 with ^{52}Cr [44]. The all-optical evaporation technique developed at Georgia University [12], allows to directly condense the atoms independently of their internal magnetic

state, allowing for a faster and more direct route to create spinor samples. Since then, several experiments have explored the spin mixing collision phenomena giving rise to spin oscillations [45, 46], spin squeezing and entanglement [47–49]. Also, spinor vortices [50] and solitons [51] have been observed. The ground state properties of spin-1 condensates have been subject of many theoretical [52–54] and experimental [55–57] studies.

Another interesting regime is when the system is in the ultra-low magnetic field regime. For the particular case of ^{87}Rb , the dipole-dipole interactions $\simeq h \times 1$Hz, while the Zeeman shift of the levels is $\simeq h \times 10^9$Hz/T. The DDI are predicted to play a major role in determining the ground state properties in a regime where the Zeeman splitting is comparable to the interaction energy i.e for magnetic fields $\simeq$pT-nT. Dipolar effects and quantum magnetism are predicted to appear under certain conditions in a number of theoretical works [58**?** –61].

In this chapter, I will introduce the basic theory supporting the rest of this work. The single-particle quantum mechanical description of the ^{87}Rb atoms in the presence of a static and time dependent magnetic field is reviewd. The basic theory of scalar Bose-Einstein condensation in the mean field approximation is presented before generalizing the description to the case of multicomponent spin-1condensates.

1.1 Energy level structure of ^{87}Rb and spin-1 physics

Rb is an alkali mtetal with two natural isotopes, ^{85}Rb and ^{87}Rb. We will concentrate on ^{87}Rb . It has $Z = 37$ electrons and $N + Z = 87$ nucleons, where N is the number of neutrons. Its principal quantum number is $n = 5$, and it has a single valence electron. The interaction of this outer electron with the nuclear spin, and the angular momentum of the whole atom will give rise to the fine energy level structure. The nuclear spin is I= 3/2 the ground state is $n^{2s+1}L_J \rightarrow 5^2S_{1/2}$, where L is the angular momentum of the atom, S is the spin of the outermost electron. The spin orbit coupling between the spin of the last electron and the magnetic field created by its movement around the core makes it convenient to introduce the quantum number $J = L+S$, that can take the values $\frac{1}{2} + \{0, 1, 2...\} = \{\frac{1}{2}, \frac{3}{2}....\}$. This means that the first two excited states of ^{87}Rb are $5^2P_{1/2}$ and $5^2P_{3/2}$. And the corresponding transitions from the ground state to the latter ones are called D_1 and D_2 lines respectively. Under this description, the projections m_J corresponding to the eigenvalues of the J_z operator are degenerate. The coupling between the spin of the atom and the spin of the nucleus I lifts the degeneracy and gives rise to the hyperfine level structure, characterized by the total angular momentum

$$F = I + J \qquad \text{with} \qquad |J - I| \leq F \leq J + I \qquad \text{in integer steps}$$

The energy shift of this coupling mechanism for the ground state of ^{87}Rb is ~ 6.8GHz, while for the first excited states is $\sim$300MHz. The states are labelled by the quantum numbers $|I, J, F, m_F\rangle$. The different hyperfine levels can be calculated [62]

$$\Delta E_{hfs} = \frac{1}{2}KA_{hfs} + B_{hfs}\frac{\frac{3}{2}K(K+1) - 2I(I+1)J(J+1)}{2I(2I-1)2J(2J-1)} \tag{1.1}$$

$$+ C_{hfs}\frac{5K^2(K/4+1) + K[I(I+1) + J(J+1) + 3 - 3I(I+1)J(J+1)] - 5I(I+1)J(J+1)}{I(I-1)(2I-1)J(J-1)(2J-1)} \tag{1.2}$$

Where A_{hfs} is the magnetic dipole constant, B_{hfs} is the electric quadrupole constant, C_{hfs} is the magnetic octupole consatant and $K = F(F+1) - I(I+1) - J(J+1)$. The corresponding levels for the D_2 line of ^{87}Rb are depicted in figure 1.1.

The single atom Hamiltonian describing the interaction with an external magnetic field is

$$\hat{H}_B = \frac{\mu_B}{\hbar}\left(g_S\mathbf{S} + g_L\mathbf{L} + g_I\mathbf{I}\right)\cdot\mathbf{B} \tag{1.3}$$

where g_S, g_L and g_I are the electron spin, orbital and nuclear g-factors, and μ_B is the Bohr magneton. The presence of an external field induces a shift in the energy levels of the atom. If the energy shift is small compared to the hyperfine energy splitting, F is a good quantum number and the Hamiltonian can be written

$$H = \mu_B g_F \cdot \left(B_x f_x + B_y f_y + B_z f_z\right) \tag{1.4}$$

where $(f_x, f_y, f_z) = \vec{F}$ are the spin-1 pauli matrices

$$f_x = \frac{1}{\sqrt{2}}\begin{pmatrix} 0 & 1 & 0 \\ 1 & 0 & 1 \\ 0 & 1 & 0 \end{pmatrix} \quad f_y = \frac{i}{\sqrt{2}}\begin{pmatrix} 0 & -1 & 0 \\ 1 & 0 & -1 \\ 0 & 1 & 0 \end{pmatrix} \quad f_z = \begin{pmatrix} 1 & 0 & 0 \\ 0 & 0 & 0 \\ 0 & 0 & -1 \end{pmatrix} \tag{1.5}$$

In the case of a magnetic field oriented along the $\hat{z}$ quantization axis $\vec{B} = B_z\hat{z}$, the Hamiltonian is $\hat{H}_B = g_F\mu_B f_z B_z$, which lifts the degeneracy of the energy levels corresponding to the m_F projections of the quantum operator F_z as shown in figure 1.3.

$$\Delta E_{|F,m_F\rangle} = g_F\mu_B m_F B_z = -\frac{1}{2}\mu_B m_F B_z = -\hbar p \tag{1.6}$$

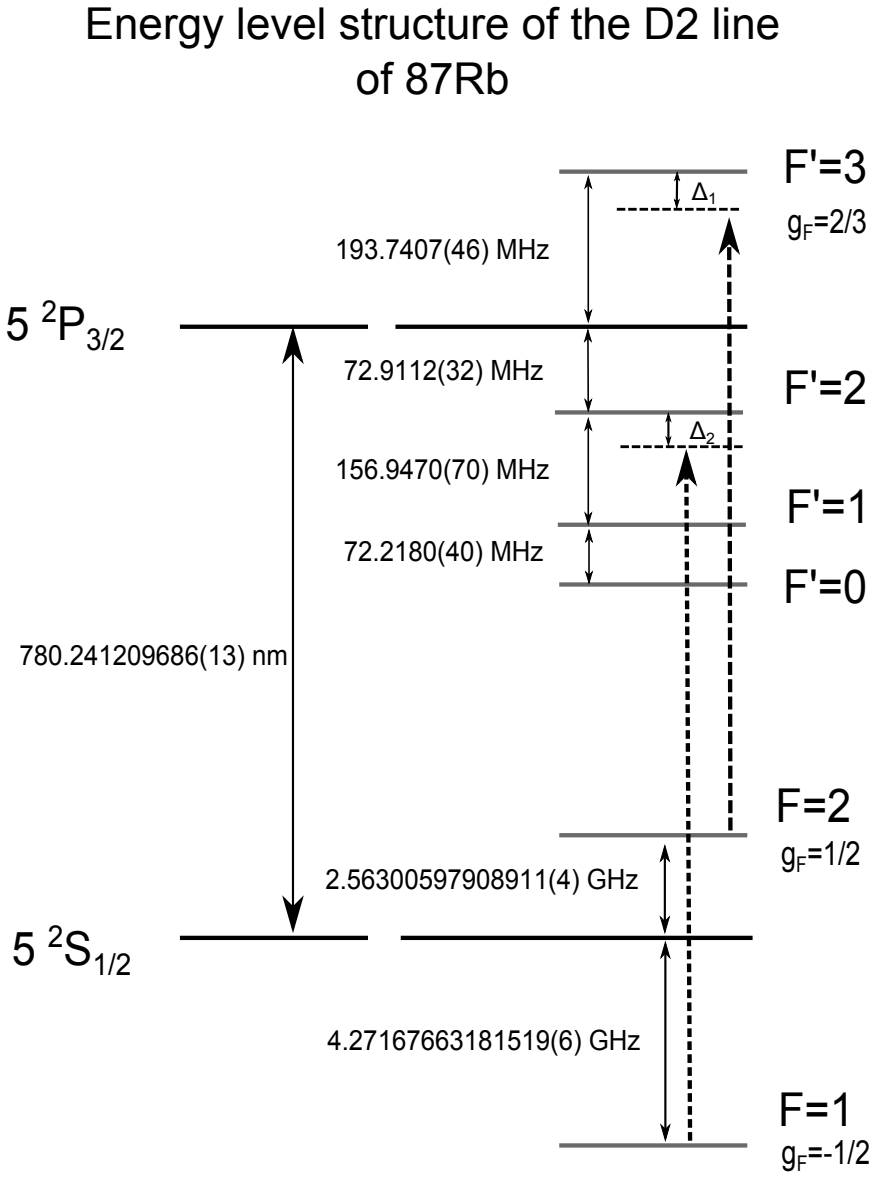

Figure 1.1: Energy levels representation of the D_2 atomic line transition in ^{87}Rb. The values of the transitions are taken from [62]. The two transitions used for laser cooling are indicated with the dashed arrows. g_F indicates the Landé factor of the levels.

whith $p = \frac{\mu_B B_z}{2\hbar}$. In the case of alkali atoms in the $L = 0$ states with $J = \frac{1}{2}$, as ^{87}Rb atoms in the $|F = 1\rangle$ manifold, the so-called "Breit-Rabi" formula allows to diagonalize the Hamiltonian in equation 1.3 and obtain analytical results for the energy levels for the case of bigger fields. The analytical expression can be found in [62]

$$E_{+1} = -\frac{E_{hfs}}{8} - g_I \mu_I B_z - \frac{E_{hfs}}{2}\sqrt{1 + x + x^2} \tag{1.7a}$$

$$E_0 = -\frac{E_{hfs}}{8} - \frac{E_{hfs}}{2}\sqrt{1 + x^2} \tag{1.7b}$$

$$E_{-1} = -\frac{E_{hfs}}{8} + g_I \mu_I B - \frac{E_{hfs}}{2}\sqrt{1 - x + x^2} \tag{1.7c}$$

where $x = \frac{g_I \mu_I B + g_J \mu_B B}{E_{hfs}}$.

Another important situation is the presence of a time varying small magnetic field in one of the perpendicular $\hat{x}, \hat{y}$ directions, like the one produced using a small radio frequency antenna, for instance $\vec{B} = B_{rf} \cos\big(\omega_{rf} \cdot t\big)\hat{x}$. Usually, such fields are small enough to be treated well within the linear regime. Therefore, the Hamiltonian can be expressed

$$\hat{H}_{rf} = -g_F \mu_B B_{rf} \cos\big(\omega_{rf} \cdot t\big) f_x \tag{1.8}$$

The total Hamiltonian $H = H_B + H_{rf}$ up to linear terms reads

$$\hat{H} = \hbar \begin{pmatrix} -p & \frac{g_F \mu_B B_{rf}}{\hbar\sqrt{2}} \cos\big(\omega_{rf} \cdot t + \phi\big) & 0 \\ \frac{g_F \mu_B B_{rf}}{\hbar\sqrt{2}} \cos\big(\omega_{rf} \cdot t + \phi\big) & 0 & \frac{g_F \mu_B B_{rf}}{\hbar\sqrt{2}} \cos\big(\omega_{rf} \cdot t + \phi\big) \\ 0 & \frac{g_F \mu_B B_{rf}}{\hbar\sqrt{2}} \cos\big(\omega_{rf} \cdot t + \phi\big) & p \end{pmatrix} \tag{1.9}$$

This Hamiltonian describes the Zeeman energy shift of the ground state levels of the atoms $\propto f_z$, and a coupling between the m_F energy levels induced by the time varying field $\propto f_x$.

If $|\phi_\alpha\rangle$ forms a complete orthogonal basis, in the Schrödinger picture the state vector describing the quantum state of a system $|\psi\rangle = \sum_\alpha c_\alpha |\phi_\alpha\rangle$, evolves according to the Schrödinger equation

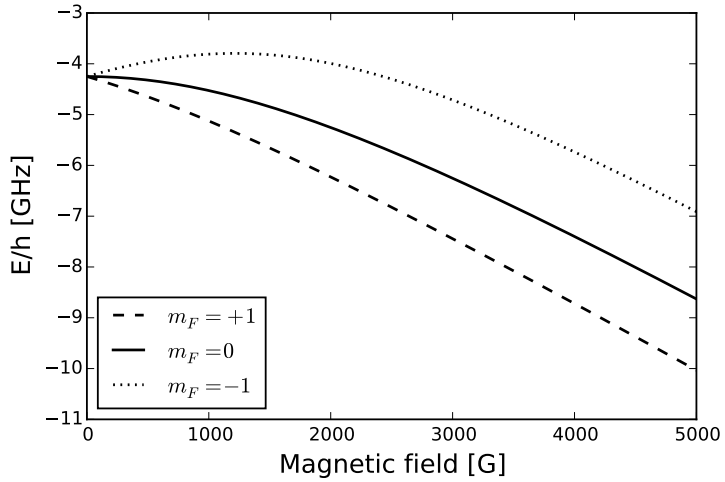

(a)

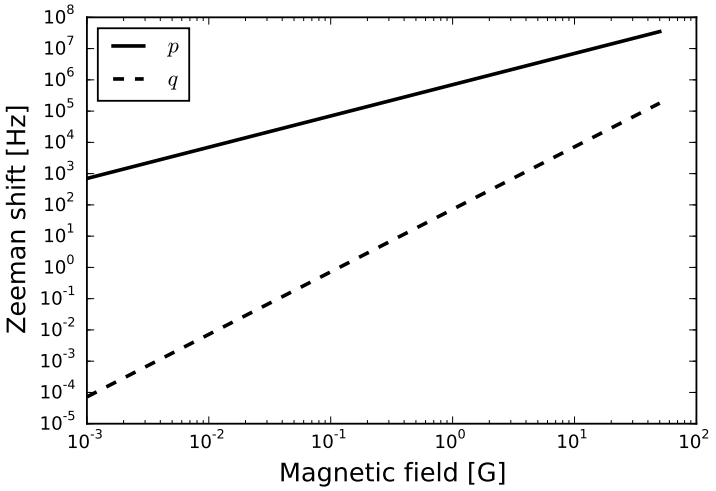

(b)

Figure 1.2: In a) a plot of the energy of the Zeeman substates of the $|F = 1\rangle$ manifold of ^{87}Rb as a function of the magnetic field. In figure b), a comparison between the linear and quadratic part of the Zeeman shift. As we can appreciate, for magnetic fields $\sim$ 1G, the linear shift is more than 4 orders of magnitud bigger than the quadratic shift.

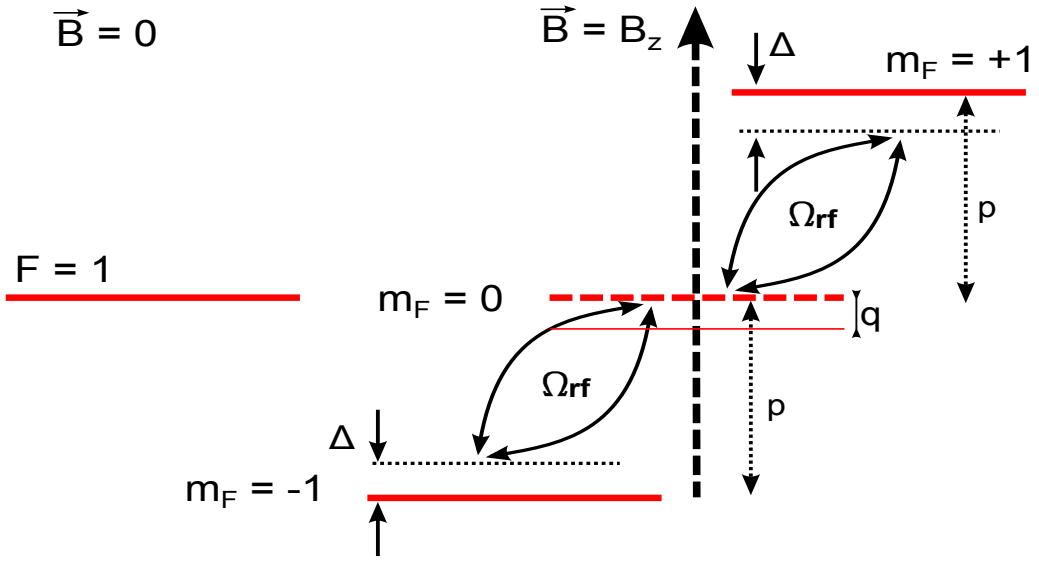

Figure 1.3: Pictorial representation of the Zeeman splitting of the ^{87}Rb $|F=1\rangle$ manifold in the presence of an external magnetic field. p, q indicate the linear and quadratic zeeman shifts of the levels. Ω_{rf} refers to the Rabi frequency coupling strength between the levels due to an oscillating magnetic field, with Δ being the detuning of the oscillating field with respect to the transition energy $\Delta = \hbar p - \hbar\omega_{rf}$.

$$i\hbar\frac{d\,|\psi\rangle}{dt} = \hat{H}\,|\psi\rangle \rightarrow i\hbar \begin{pmatrix} .. \\ .. \\ \partial_t c_\alpha \\ .. \\ .. \end{pmatrix} = \hat{H} \begin{pmatrix} .. \\ .. \\ c_\alpha \\ .. \\ .. \end{pmatrix} \tag{1.10}$$

To better understand the dynamical behaviour of the atom under the Hamiltonian in Eq. 1.9 it is convenient to use the *interaction picture*. In this picture, we transform the coordinate system into a rotating frame at the frequency ω_{rf} in order to remove the time dependence of the Hamiltonian. The transformation that we will use is given by the unitary operator

$$T = \begin{pmatrix} 1 & 0 & 0 \\ 0 & e^{iw_{rf}t} & 0 \\ 0 & 0 & e^{2iw_{rf}t} \end{pmatrix} \tag{1.11}$$

The Hamiltonian transforms according to $\hat{H}' = T^{-1}\left(\hat{H} - i\hbar\frac{dT^{-1}}{dt}\right)T$. The Hamiltonian resulting

from this transformation is time independent under the *rotating wave approximation*[1] (RWA), and can be written as

$$\hat{H} = \hbar \cdot \begin{pmatrix} -\Delta & \frac{\Omega_{rf}}{\sqrt{2}} & 0 \\ \frac{\Omega_{rf}}{\sqrt{2}} & 0 & \frac{\Omega_{rf}}{\sqrt{2}} \\ 0 & \frac{\Omega_{rf}}{\sqrt{2}} & \Delta \end{pmatrix} \tag{1.12}$$

Where $\Delta = \hbar p - \hbar\omega_{rf}$ is the detuning between the energy levels splitting and the energy of the coupling field, and $\Omega_{rf} = \frac{\mu_B B_{rf}}{\hbar 2}$ is the Rabi frequency that characterizes the coupling strength between the levels, as depicted in figure 1.3

The time evolution of the atomic state under this Hamiltonian gives rise to the so-called Rabi oscillations. The probability of an atom to be in each m_F state is given by solving the corresponding Schrödinger equation

$$i\hbar \frac{d\,|\psi\rangle}{dt} = H\,|\psi\rangle \rightarrow |\psi(t)\rangle = |\psi(t=0)\rangle\, e^{-\frac{i}{\hbar}Ht} \tag{1.13}$$

Two simple cases are considered here because they are of practical use in the experiment. I will consider the initial samples to be completely *magnetized* i.e all the atoms populating the $m_F = +1$ state, or to be completely *polarized*, meaning that all the atoms populate the $m_F = 0$ state.

To find analyticall solutions we solve the system of coupled differential equations

$$i\hbar \begin{pmatrix} \partial_t c_{+1} \\ \partial_t c_0 \\ \partial_t c_{-1} \end{pmatrix} = \hbar \cdot \begin{pmatrix} -\Delta & \frac{\Omega_{rf}}{\sqrt{2}} & 0 \\ \frac{\Omega_{rf}}{\sqrt{2}} & 0 & \frac{\Omega_{rf}}{\sqrt{2}} \\ 0 & \frac{\Omega_{rf}}{\sqrt{2}} & \Delta \end{pmatrix} \begin{pmatrix} c_{+1} \\ c_0 \\ c_{-1} \end{pmatrix} \tag{1.14}$$

with initial conditions $(c_{+1}, c_0, c_{-1}) = \big\{(1,0,0),(0,1,0)\big\}$. The solutions are found using standard linear algebra methods. In particular, for the simpler case of the polarized sample, the system behaves as an effective two-level system due to the symmetry of the initial conditions. The pobabilities of finding

[1] The RWA is a general procedure to simplify time dependent Hamiltonians discarding the terms whose contribution to the dynamics, within the relevant timescales of the problem, can be averaged to zero. It is widely used in the light matter interaction problem when the detuning of the light from the transition of interes is sufficiently large.

an atom in each substate are [63]:

$$c_{+1}^2 = c_{-1}^2 = \frac{1}{2}\frac{\Omega^2}{\Omega_{eff}^2}\sin\left(\frac{\Omega_{eff}t}{2}\right)^2 \tag{1.15a}$$

$$c_0^2 = 1 - \frac{\Omega^2}{\Omega_{eff}^2}\sin\left(\frac{\Omega_{eff}t}{2}\right)^2 \tag{1.15b}$$

where $\Omega_{eff} = \sqrt{\Omega_{rf}^2 + \Delta^2}$. On the other hand, for the case of the magnetized sample, the solution is found as in [64]:

$$c_{+1}^2 = \frac{\Omega^4}{\Omega_{eff}^4}\sin^4(\frac{1}{2}\Omega_{eff}t) \tag{1.16a}$$

$$c_0^2 = \frac{1}{2}\left[\frac{4\Delta^2\Omega^2}{\Omega_{eff}^4}\sin^4(\frac{1}{2}\Omega_{eff}t) + \frac{\Omega^2}{\Omega_{eff}^2}\sin^2(\Omega_{eff}t)\right] \tag{1.16b}$$

$$c_{-1}^2 = 1 - c_{+1}^2 - c_0^2 \tag{1.16c}$$

In figure 1.4 I have plotted the probabilities of each Zeeman substate with the same initial conditions $(1, 0, 0)$ for different detunings {a),c),e)} and different Rabi frequencies with a fixed detuning {b),d),f)}. In the case of different detunings (left column), we can observe how at $\Delta = 0$, the population is fully transfered from the $|m_F = +1\rangle \rightarrow |m_F = -1\rangle$ with a frequency Ω_{rf}. As the detuning increases, the population transfer to the $|m_F = -1\rangle$ is never complete, and some atoms remain in the $|m_F = 0\rangle$ state. The frequency of the oscilations in the probability distribution increases with the detuning, because $\Omega_{eff} = \sqrt{\Delta^2 + \Omega_{rf}^2}$. For the case of fixed detuning and increasing Ω_{rf} (right column), the population transfer from the $|m_F = +1\rangle$ to $|m_F = -1\rangle$ is always the same, but as Ω_{rf} increases, the transfer occurs faster.

1.2 Spin-1 Bose-Einstein condensation

Up to now, the physical description of single spin-1 atoms have been reviewed. Now we will consider what happens in the many particle regime. I will first review the basic concepts of single species Bose-Einstein condensation, which we will extend to the spin-1 case.

In this section I will review the theoretical description of a Spin-1 condensate. The collisional properties of the Zeeman sub-states determine the ground state properties of the spin-1 gases. They can be classified into *ferromagnetic* or *antiferromagnetic* depending on the sign of c_2 that is related to the

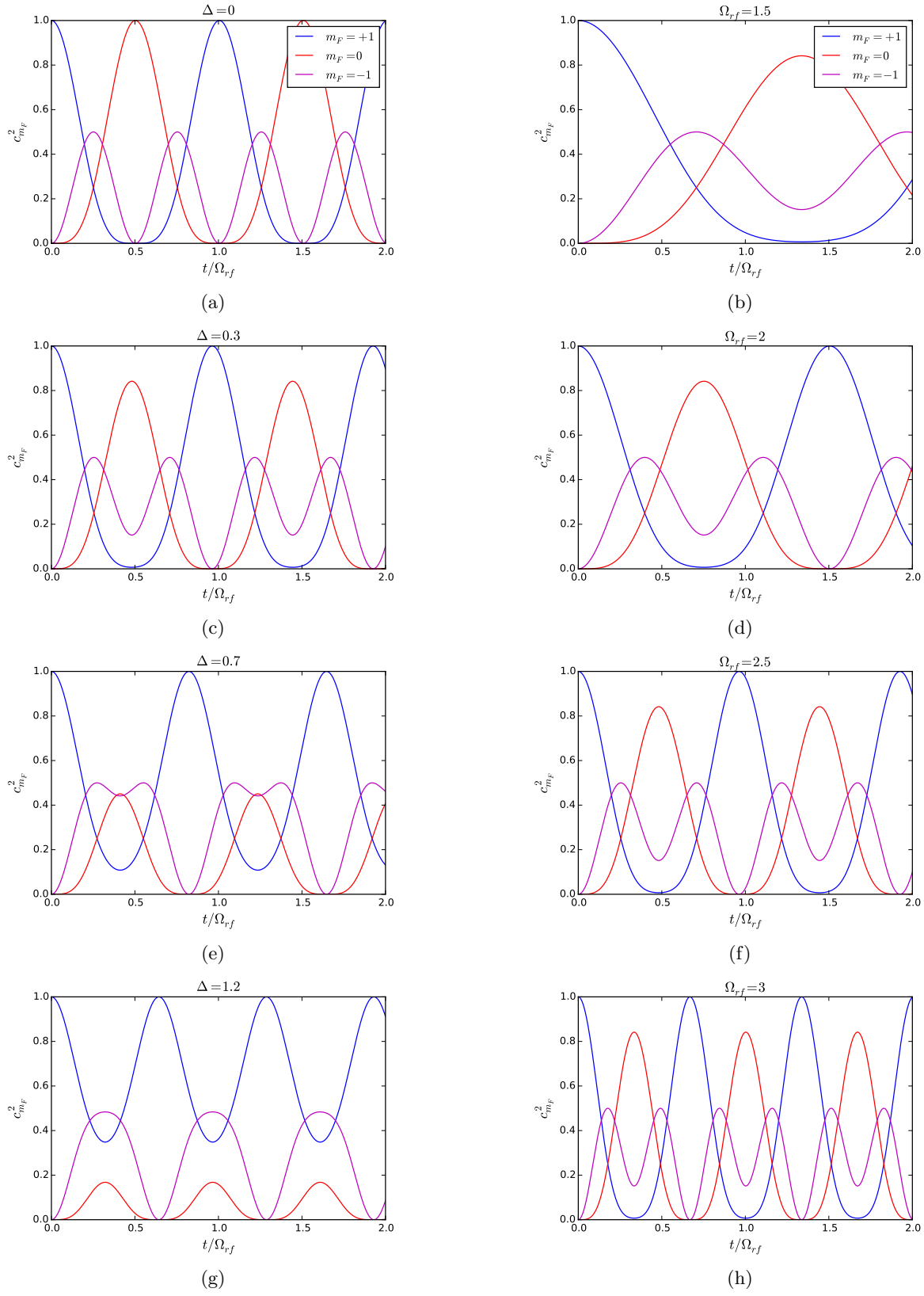

Figure 1.4: Theoretical plots of Rabi oscillations. The blue, red and magenta lines correspond to the $m_F = +1$, $m_F = -1$, and $m_F = 0$ states respectively. In the left column, typical Rabi oscillations for different values of the detuning are shown. On the right column, the detuning is constant, and the rabi frequency is increased.

difference between the scattering lenghts associated with the two collisional channels present on the system. In the case of ^{87}Rb , the spin dependent interactions make $c_2 < 0$, that in turns determine the ferromagnetic character of its ground state. This has been confirmed by several groups [43, 65, 66]. First, I will introduce the most general description of the system using the second quantization language. We will use the Mean-Field (MF) approximation to simplify the description. I will mainly follow [27, 28]. For a review on the subject with a more advanced and detailed mathematical description, see [67]. The Single-Mode-Approximation will be discussed, which consists in assuming that the three components of the order parameter share the same spatial wavefunction. This approximation can be made when the size of the condensate is less than the *spin healing length* $\xi_s = \sqrt{\frac{\hbar}{2mc_2 n}}$ [68].

1.2.1 Overview of Bose-Einstein Condensation

It is known that a system of bosons at temperature T is well described using the grand canonical ensemble, with the partition function and number of atoms given by

$$\mathcal{Z} = \prod_i \frac{1}{1 - ze^{-\beta\epsilon_i}} \tag{1.17a}$$

$$N = \sum_i \frac{ze^{-\beta\epsilon_i}}{1 - ze^{-\beta\epsilon_i}} = \sum_i N_i \tag{1.17b}$$

where i runs over all energy levels of the system with energy ϵ_i, with N_i atoms occupying each level. The reduced temperature is $\beta = \frac{1}{k_B T}$, and the fugacity $z = e^{\beta\mu}$, with μ being the chemical potential. In the case of a weakly interacting gas of bosons with N particles confined in a 3D harmonic potential, the system undergoes a transition at a temperature T_c given by [69]:

$$k_B T_c = 0.94\hbar\bar{\omega}\sqrt[3]{N} \tag{1.18}$$

where $\bar{\omega}$ is the geometric average of the trapping frequencies characterizing the harmonic potential and k_B is the Boltzmann constant. Below this temperature, the occupation of the lowest energy state becomes macroscopically large $N_0 \sim N$, while the occupation of the excited levels is $N_{i>0} \sim 1$. The total number of atoms in the excited states is $N - N_0 = 1.202\left(\frac{k_B T}{\hbar\bar{\omega}}\right)$.

The Hamiltonian of the system in the second quantization language is

$$\hat{H} = \int d\vec{x}\hat{\psi}^\dagger(\vec{x})\left(-\frac{\hbar^2\nabla^2}{2m} + U_{ext}(\vec{x})\right)\hat{\psi}(\vec{x}) + \frac{1}{2}\int d\vec{x}d\vec{x'}\hat{\psi}^\dagger(\vec{x})\hat{\psi}^\dagger(\vec{x'})V(\vec{x}-\vec{x'})\hat{\psi}(\vec{x'})\hat{\psi}(\vec{x}) \tag{1.19}$$

where $U_{ext}(\vec{x})$ is the external trapping potential, m is the mass of the atoms, $V(\vec{x}-\vec{x'})$ is the interaction potential between atoms in the condensate. In the case of low energy collisions, as it is the case, it can be reduced to a contact potential of the form $V(\vec{x}-\vec{x'}) = g\delta(\vec{x}-\vec{x'})$ with $g = \frac{4\pi\hbar^2 a}{m}$ where a is the s-wave scattering length. $\hat{\psi}^\dagger(\vec{x})$ is the boson field operator that creates a particle in $\vec{x}$.

The equations for the time evolution of the condensate wavefunction under the Heisenberg picture can be obtained from the expression:

$$i\hbar\frac{\partial\hat{\psi}}{\partial t} = \left[\hat{\psi}, \hat{H}\right] \tag{1.20}$$

The mean field approach to describe Bose-Einstein condensation was first stablished by Bogoliubov in 1974. Within this approximation, we replace the field operator by its expectation value $\phi(\vec{x},t) = \langle\hat{\psi}(\vec{x})\rangle$ i.e, replacing a complex quantum field by a classical field. $\phi(\vec{x},t)$ is also called the order parameter of the condensate. Following the previous relations, the scalar wave function of a Bose-Einstein condensate is generally described in the mean field approach by the *Gross-Pitaevskii equation*:

$$i\hbar\partial_t\phi(\vec{x},t) = \left(-\frac{\hbar^2\nabla^2}{2m} + U(\vec{x}) + \hbar g|\phi(\vec{x},t)|^2\right)\phi(\vec{x},t) \tag{1.21}$$

The ground state of the condensate is derived following a variational approach from the energy functional:

$$H = \int d^3\vec{x}\left[\phi^*(\vec{x})\left(-\frac{\hbar^2\nabla^2}{2m} + U(\vec{x})\right)\phi(\vec{x}) + \frac{\hbar g}{2}|\phi(\vec{x})|^4\right] \tag{1.22}$$

1.2.2 Mean-field description of a Spin-1 BEC

In the case of a spin-1 BEC, the interaction term in the Hamiltonian needs to be revisited, since the different internal states interact with each other in different ways. This interaction between the particles in the different substates plays a major role in the dynamics of the condensate. As in the case of the scalar BEC considered before, we only consider two-body collisions in the s-wave scattering limit. This is a valid assumption at low energies in dilute gases. Every particle in the system has an individual spin $\vec{f}$. When two atoms collide, the total angular momentum of the two-particle system is $\vec{F} = \vec{f_1} + \vec{f_2}$. In the s-wave scattering limit and for bosonic particles, there are only two allowed scattering channels for total spins $F = 0$ and $F = 2$. This can be deduced by symmetry arguments about the rotational symmetry of the spin and the symmetry of the wave-functions with respect to the interchange of particles [67]. The

general form of the interaction can be written as

$$V_{int} = \delta(\vec{x}_1 - \vec{x}_2) \sum_{F=0}^{2F} g_F P_F \tag{1.23}$$

where P_F is the projector of the subspaces of the total momentum space F, $P_F = \sum_{m_F} |F, m_F\rangle \langle F, m_F|$ [27]. For a system of $f = 1$ particles, $V = g_0 P_0 + g_2 P_2$. The projectors $P_{0,2}$ can be written in terms of products of the individual spin operators $\vec{f_1} \cdot \vec{f_2}$ [27]. Then it is easy to rewrite the interaction potential as

$$V_{int} = \delta(\vec{x}_1 - \vec{x}_2) \left(c_0 + c_2 \vec{f_1} \cdot \vec{f_2} \right) \tag{1.24}$$

where c_0, c_2 parameters describe the spin-independent and spin-dependent parts of the atomic interactions. They are given by:

$$c_0 = \frac{4\pi\hbar^2}{m} \frac{a_0 + 2a_2}{3} \tag{1.25}$$

$$c_2 = \frac{4\pi\hbar^2}{m} \frac{a_2 - a_0}{3} \tag{1.26}$$

with a_0, a_2 being the s-wave scattering lengths of binary collisions with total spin $F = 0, 2$ respectively (see Tab. 1.1). Using the second quantization formalism, the total Hamiltonian of a spin-1 Bose condensed gas can be writen:

$$\hat{H} = \int d\vec{x} \left\{ \sum_{i,j} \hat{\psi}_i^\dagger \left(-\frac{\hbar^2 \nabla^2}{2m} + U_{ext}(\vec{x}) \right) \hat{\psi}_j + \frac{c_0}{2} \hat{\psi}_i^\dagger \hat{\psi}_j^\dagger \hat{\psi}_j \hat{\psi}_i + \frac{c_2}{2} \sum_{\alpha,i,j,k,l} (f_\alpha)_{i,j} (f_\alpha)_{k,l} \hat{\psi}_i^\dagger \hat{\psi}_k^\dagger \hat{\psi}_l \hat{\psi}_j \right\} \tag{1.27}$$

The field operator $\hat{\psi}_i(\vec{x}, t)$ destroys a particle in the state i at position $\vec{x}$. The subscripts $i, j, k, l = -1, 0, +1$ specify the magnetic substate of the atom.

This Hamiltonian gives us already useful information about the system:

- The actual values of a_0, a_2 determine the ground state properties of the spin-1 BEC. When $a_0 > a_2 \rightarrow c_2 < 0$. This favours a state in which the spin-dependent interaction term of the Hamiltonian (equation 1.27) is maximized. This makes the ground state show ferromagnetic properties i.e it favours the alignment of the spins in the same direction.

- On the other hand, for $a_0 < a_2 \rightarrow c_2 > 0$. And therefore, a state in which the spin-dependent

interaction is minimized is more favorable. In this case the system will have antiferromagnetic properties, and the more energetically favorable configuration will be that in which the spin of the atoms are aligned in opposite directions.

- In the interaction term (second and third terms in equation 1.27) we can distinguish between two types of collisions: intra-species and inter-species collisions, and spin-exchange collisions. In the first kind, the two particles collide and exchange their internal angular momentum $|f=1,m_f=i\rangle + |f=1,m_f=j\rangle \longleftrightarrow |f=1,m_f=j\rangle + |f=1,m_f=i\rangle$. In the second case, the pair of atoms that result from the collisional process have different internal angular momentum, while conserving the total. This corresponds to collisions $2\times|f=1,m_f=0\rangle \longleftrightarrow |f=1,m_f=+1\rangle + |f=1,m_f=-1\rangle$. These are called spin-exchange collisions.

- In ^{87}Rb the mean-field energy associated with the spin-dependent part of the Hamiltonian $|c_2|n \simeq 200$pK for densities in the order of 10^{14}cm^{-3}. This energy scale is typically much smaller than the temperature of the gas, or the scalar mean field energy, but nonetheless, it induces a non-negligible coupling between the magnetic substates that induces a rich variety of dynamical trajectories of the spinor condensates.

- The U_{ext} potential represents the trapping potential, but it can be modified to include the effect of external magnetic fields by adding $U_{ext}^B = -pm+qm^2$, where p,q represent the linear and quadratic Zeeman terms, and m is the internal state of the particle.

The presence of an external magnetic field $\vec{B}$, as mentioned above, has important consequences for the evolution of the system. In the first place, it sets a quantization axis and lifts the degeneracy of the Zeeman substates. It is convenient to choose the quantization axis to be along the $\hat{z}$ direction. The energy of each Zeeman state under such a field $\vec{B}=B_z\hat{z}$, including the quadratic Zeeman effect is given by $E_m^{Zeeman} = -pm+qm^2$ with $p=\frac{1}{2}\frac{\mu_B B_z}{\hbar}$ and $q=\frac{p^2}{w_{hfs}}$. We can check that the total number of atoms and the magnetization, defined as

$$N = \int d\vec{x}\left(|\psi_1|^2+|\psi_0|^2+|\psi_{-1}|^2\right) \tag{1.28}$$

$$M = \int d\vec{x}\left(\hat{\psi}_i^\dagger (f_z)_{i,j}\hat{\psi}_j\right) = \int d\vec{x}\left(|\psi_1|^2-|\psi_{-1}|^2\right) \tag{1.29}$$

commute with the Hamiltonian in equation 1.27 [52]. Therefore they are conserved quantities. This has important consequences. In principle, the Zeeman energy associated with the presence of an external magnetic field is much higher than the spin-dependent mean-field energy. This means that the dynamics

	^{87}Rb	^{23}Na
a_0	101.8±0.2a_B	47.36±0.8a_B
a_2	100.4±0.1a_B	52.98±0.4a_B
$a_2 - a_0$	-1.45±0.32a_B	3.5±1.5a_B

Table 1.1: Measured s-wave scattering lengths for ^{87}Rb and ^{23}Na. The direct values of a_2, a_0 have been measured using molecular spectroscopy in [70] for ^{23}Na and [65] for ^{87}Rb . The value given for the difference was inferred from measurements of the spin dynamics for ^{87}Rb [46] and ^{23}Na [31]. a_B = 0.0529nm is the Bohr radius.

due to the spin-exchanging collisions should be suppressed unless the magnetic field present on the system would be on the order of $\sim \mu$G. Nevertheless, the conservation of the magnetization makes the spin-mixing collisions the only path that the system can take to lower its energy in the presence of an external magnetic field. This enhances this collisional processes and allows the observation of spin-mixing dynamics for fields up to $\simeq$ 100mG.

1.2.3 Dyamical equations and Single Mode Approximation

The dynamics of a spin-1 system can be derived as a set of three coupled equations by applying the Heisengberg equation of motion to each $\hat{\psi}_i$ separately

$$i\hbar\frac{\partial\hat{\psi}_i}{\partial t} = \left[\hat{\psi}_i, \hat{H}\right] \quad \text{for } i = 0, \pm 1 \tag{1.30}$$

In the mean-field description, the dynamical equations for this three components order parameter are

$$i\hbar\frac{\partial\phi_{+1}}{\partial t} = \mathcal{L}_{+1}\phi_{+1} + c_0 n\phi_{+1} + c_2(n_1 + n_0 - n_{-1})\phi_1 + c_2\phi^*_{-1}\phi_0\phi_0 \tag{1.31}$$

$$i\hbar\frac{\partial\phi_0}{\partial t} = \mathcal{L}_0\phi_0 + c_0 n\phi_0 + c_2(n_1 + n_{-1})\phi_0 + 2c_2\phi^*_0\phi_{+1}\phi_{-1} \tag{1.32}$$

$$i\hbar\frac{\partial\phi_{-1}}{\partial t} = \mathcal{L}_{-1}\phi_{-1} + c_0 n\phi_{-1} + c_2(n_{-1} + n_0 - n_{+1})\phi_{-1} + c_2\phi^*_1\phi_0\phi_0 \tag{1.33}$$

where $\mathcal{L}_{\pm,0} = \left(\frac{-\hbar^2\nabla^2}{2m} + U^{ext}_{\pm,0}\right)$. n is the total density and n_i is the density of each spin component. Some remarks from the above equations:

- The first two terms of the rhs of these equations describe the spin-independent part of the dynamics, accounting for the spatial dynamics of the wave-function.
- The third term couples the spatial dynamics of the three components.
- The last term drives the coherent spin-mixing dynamics of the system, leading to population ex-

change between different spin components.

A great simplification of the above equations is possible if we assume that the spatial degrees of freedom are not coupled to the spin degrees of freedom [68]. The assumption is valid when the spin dependent energy is small compared to the spin independent energy. The criterion can be expressed in terms of the spin healing length. The SMA approximation will be valid if the size of the condensate is smaller than the spin healing length $R_{TF} < \xi_s$. This can be expressed formally writing the spinor order parameter as a product of two decoupled functions:

$$\phi_i = \phi(\vec{x})e^{-\frac{i\mu t}{\hbar}}\chi_i(t), \text{ subject to the normalization } |\vec{\chi}|^2 = 1, \text{ and } \int d\vec{x}|\phi(\vec{x})|^2 = N \tag{1.34}$$

where μ is the chemical potential and $\vec{\chi}$ is the internal state vector. We can substitute this ansatz into equation 1.33. Then, we can solve separately the spatial and internal dynamics. The spatial wave-function can be found using the same methods that are applicable to the scalar Bose-Einstein condensates. For the spin-dependent part, we arrive at the coupled equations [46]:

$$i\hbar\partial_t\chi_1 = E_1\chi_1 + c\left(\rho_1 + \rho_0 - \rho_{-1}\right)\chi_1 + \chi_0^2\chi_{-1}^* \tag{1.35}$$

$$i\hbar\partial_t\chi_0 = E_0\chi_0 + c\left(\rho_1 + \rho_{-1}\right)\chi_0 + 2\chi_0^*\chi_{-1}\chi_1 \tag{1.36}$$

$$i\hbar\partial_t\chi_{-1} = E_{-1}\chi_{-1} + c\left(-\rho_1 + \rho_0 + \rho_{-1}\right)\chi_{-1} + \chi_0^2\chi_1^* \tag{1.37}$$

with ρ_i is the fractional population of each spin component and $c = c_2\int d\vec{x}|\phi(\vec{x})|^4$.

CHAPTER 2

EXPERIMENTAL SETUP

In this chapter I will present a detailed description of the experimental apparatus that I have built during my time in this project. The main building blocks of the setup are the vacuum system, the laser system and the computer control. The vacuum system is formed by two different vacuum chambers that are connected through a differential pumping stage, the 2D MOT chamber and the science chamber. The atoms are collected in the 2D MOT chamber before we push them to the science chamber where we cool them using standard laser cooling techniques to 50μK in a 3D Magneto Optical Trap (MOT) before transfering them to an optical dipole trap, where we perform evaporative cooling to achieve condensation.

The chapter is organized as follows. In section section 2.1 I give a brief overview of the laser cooling and trapping techniques to better understand the requirements of the experiment. In section 2.2 I will describe the vacuum setup. I will explain the need of using two chambers, the differential pumping stage that we implemented and the sealing technique that we used. In section 2.3 I will present with detail the laser system used to cool, trap and probe the atoms, including the locking techniques required for tuning and stabilization of their frequency. Here I will also describe the laser system used for the optical dipole trap (ODT), which is composed of two different wavelengths. Section 2.5 is dedicated to describe the detection scheme and to present the absorption imaging technique that we use to acquire information about the atomic sample. To finalize, section 2.6 gives an overview of the computer control system and software implemented in the experiment.

2.1 Laser cooling

Light-matter interaction at the single atom level is a very complex quantum mechanical problem that I do not intend to cover here. For the purposes of this thesis, we just need to understand how we use coherent light to manipulate the external and internal degrees of freedom of the atoms. Let's consider an atom with only two levels, a ground state represented by $|0\rangle$ and an excited state $|1\rangle$. When the atom absorbs

a photon with energy $\hbar\omega$ corresponding to the transition energy between $|0\rangle \rightarrow |1\rangle$ and momentum $\hbar\vec{k}$, it acquires a recoil momentum $\vec{p}_{recoil} = -\hbar\vec{k}$ in the opposite direction of the propagating photon. The change of momentum is equivalent to a force that pushes the atom in the opposite direction. After absorbing the photon, the atom will re-emit it in a random direction and decay to its ground state. This decay process has a natural lifetime τ associated with it. The lifetime depends on the atomic properties and the particular transition which has been excited. Associated with the lifetime, the linewidth of the transition is defined as $\Gamma = \tau^{-1}$. For the D_2 line of ^{87}Rb has a value of $\Gamma = 2\pi \cdot 6.0666$MHz [62]. When the absorption/emission process occurs many times, there is a net force applied to the atoms in the direction of the wave-vector $\vec{k}$ of the photons:

$$F_{sc} = R_{sc}\hbar\vec{k} \tag{2.1}$$

where $R_{sc} = \frac{\Gamma}{2}\frac{I/I_s}{1+4(\Delta/\Gamma)^2+(I/I_s)}$ is the scattering rate. Γ is the linewidth of the transition, $\Delta = \omega - \omega_0$ is the detuning of the light from the transition frequency, I is the intensity of the light and I_s is the saturation intensity of the transition.

We can consider an atom and two counterpropagating red detuned beams. Due to the Doppler effect, the atom will preferentially absorb photons from the beam propagating in the opposite direction to its velocity. This will exert a slowing force that will eventually make the atom travel in the opposite direction. In that moment, it will start to feel the force in the opposite direction due to the other beam. The force resulting from this cooling mechanism is velocity dependent, as shown in figure Fig. 2.1b. The minimum temperature achievable using this method has intrinsic limits, the *Doppler temperature*, that for ^{87}Rb is $T_D = \frac{\hbar\Gamma}{2k_B} \approx 146\mu$K.

Using the described configuration, one can slow down an atomic ensemble, but there is no trapping force. We need a position dependent force mechanism to trap the atoms in a particular point in space. This is realized applying a quadrupole magnetic field. The presence of such field introduces a position dependent energy landscape for atoms in different magnetic substates due to the linear Zeeman effect (see section 1.1). The transitions induced between states with different m_F quantum numbers need to be compatible wiht the conservation of angular momentum. The state of polarization of the photons needs to be taken into account. *Right handed* circularly polarized light σ^+, will induce transitions from $m_F \rightarrow m_{F'} + 1$, while *left haded* polarized light σ^- will induce $m_F \rightarrow m_{F'} - 1$. Transitions between states with the same m_F number are induced by *linearly* polarized light π. The polarization of the beams can be chosen in a way that the atoms feel a scattering force that depends on their velocity and position, and that points towards the centre of the magnetic field gradient. The generalization of this scheme to the three spatial dimensions creates a Magneto-Optical Trap (MOT) that constitutes the basic tool of cold

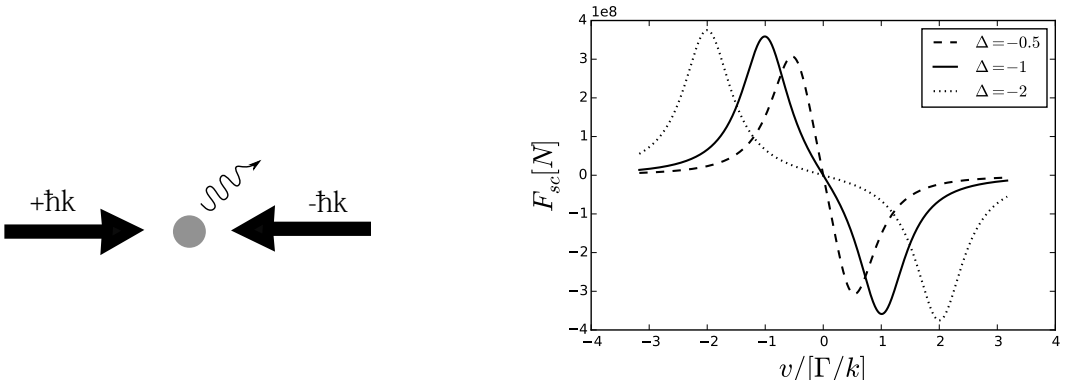

(a) (b)

Figure 2.1: In a), a schematic drawing of the cooling technique using the scattering force from two counterpropagating beams. In figure b), a plot of the scattering force (equation 2.1) that an atom experiences in the previous configuration as a function of its velocity and for three different detunings of the light with respect to the transition frequency.

atoms experiments.

2.2 Vacuum system

The typical energy scale of cold atoms experiments is ∼100nK. At room temperature, gas molecules have a typical energy ∼300K, around 9 orders of magnitude higher. This means that any collision between cold atoms and thermal atoms will completely destroy the properties of the cold atom system. To avoid collisions with background particles, ultra-cold atoms experiments need to be perform in UHV environments, ranging from $\sim 10^{-7}$mbar for typical atom interferometers to $\leq 10^{-10}$mbar for Bose-Einstein condensate experiments. To achieve the low pressure needed, the vacuum system has to be carefully designed. In this section I will describe the vacuum system that we have designed and implemented in our experimental set up.

Our vacuum system, sketched in figure 2.3b is formed of two chambers. The two chambers configuration is needed to keep a differential pressure between both of them. In the 2D MOT chamber, the vapour pressure of ^{87}Rb atoms needs to be sufficiently high ($\simeq 10^{-7}$mbar) to load the MOT from background gas. However, in the science chamber, we need to keep a pressure lower than 10^{-10}mbar. This is achieved by connecting the two chambers with a differential pumping stage. The differential pumping stage is a tube-like hole in between the two chamber of the vacuum system. It has a diameter of 1.1 mm and it is 21 mm long. The conductance of the tube is very low, and can be calculated as:

(a) (b)

Figure 2.2: Figure (a) shows a picture of the titanium vacumm chamber wit the indium wire placed on the groove to allow proper sealing. Figure (b) shows the vacuum chamber after the windows and the compression flanges have been attached.

$$C = \left[1 + \frac{3l}{8r}\right]^{-1} \cdot \frac{\pi \bar{v} r^2}{4} \approx 8 \times 10^{-6} m^3 s^{-1} \tag{2.2}$$

Where $\bar{v}$ is the average velocity of air molecules at 25°C, l is the length of the tube and r is the radius of the tube. This allows to maintain a pressure difference between the two chambers of at least three orders of magnitude, as it is indicated by the reading from our ion-pumps. This differential pumping stage also acts as a collimation pathway for the ^{87}Rb atoms that are transfered from the 2D to the science chamber, where the experiments are performed. The 2D MOT chamber and the differential pumping stage are custom designed and have been machined from a single titanium block in the workshop at the University of Birmingham. The material choice was determined by two main factors. First, the low outgassing rate of the material. In the second place, titanium was chosen because it is non-magnetic.

On the back side of the 2D MOT chamber there is a viewport to allow optical access to the chamber. We use this viewport to send a weak resonant beam to push the atoms to the science chamber. A 20 l/s ion pump (Vinci Technologies) is connected through a "T" to the 2D MOT chamber. On the other arm of the "T" we connected a UHV valve. This valve is used to rough out the system using a turbo pump.

The elliptical windows on the four sides of the titanium chamber allow for the optical access necessary to create the 2D MOT. They are approximately $8cm \times 2.5cm$ to allow big elliptical beams to pass through, since bigger beams allow for a more efficient loading, cooling and transfer of the atoms to the science chamber. These windows are sealed to the titanium chamber using a sealing technique in which a thin Indium wire is squashed between two different materials to provide sealing. A thin groove was machined along the window frame of the chamber to allow the Indium wire to be easily set, as shown in figure 2.2a. The groove has a rectangular shape of 1.1mm wide and 0.5mm depth. The indium wire (GoodFellow) has a diameter of 1.8mm. To attach the window to the chamber, the coated window was positioned over the chamber frame, and an uniform pressure of $\simeq 0.4$N was applied over the sides of the

window using custom designed compression flanges, which are attached to the main chamber using 26 M-3 screws as shown in figure 2.2b. The atoms are collected into the 2D MOT from the background gas. To deliver the atoms, a flexible metal bellow that contains a glass ampule of $\approx$ 1gr of Rb is connected to the 2D chamber using a valve. This tube is bent after the baking, breaking the glass ampule and allowing the Rb to flow into the chamber with a vapour pressure corresponding to the temperature of the room. The conductance ($C < 1$) between the bellow and the chamber reduces the available vapour pressure on the 2D side. To obtain a higher Rb pressure, we heat up the tube to about 50°C, which corresponds to $\simeq 4 \times 10^{-6}$mbar within the valve, calculated according to the formula given in [62].

The science chamber is a glass cell (Precision-Glassblowing) attached to the titanium chamber at the end of the pumping stage. It is a glass tube of $\simeq$ 30 cm ending in a rectangular laser bonded glass cell. The size of the cell is $2.5 \times 2.5 \times 10$ cm. The cell is coated on the outside for 780nm and 1550nm wavelength light to minimize reflections. The long tube is a peculiarity of our set up, as compared to other similar experiments. The reason for the glass cell to be so long is to allow for the accomodation of several layers of magnetic shielding material as mentioned before. The glass chamber is connected to the titanium chamber using a CF-40 flange. We attached a NEXTorr-100D (SAES Getters) pump to the titanium chamber on the science side of the chamber to pump the glass chamber. It has a pumping speed of 6l/s and a "getter" attached to it. It is attached to the titanium chamber through a special "nipple" tube (SAES Getters) with a conical shape to increase the performance of the pumping.

2.3 Laser system

In this section I will present the general layout of the set up that we use to combine, distribute and modulate the laser light used for cooling and detection of the ^{87}Rb atoms. This laser system is based on commercial ECDL's and tappered amplifiers (TA) for light amplification. Their central wavelength is around 780nm, close to the D2 line transition of ^{87}Rb. To correctly control and tune the frequency of the lasers, we use two locking techniques. The two locking schemes will be described in detail. Later, I will describe the laser system used for the dipole trap and evaporative cooling stage, the last step to reach the quantum degenerate regime. This laser system is formed by two different lasers: an Ytterbium fiber laser (IPG photonics) with a wavelenght of 1070nm, and an external cavity laser (Thorlabs) with 1550nm wavelength working as a seed for a fiber amplifier (Nufern).

The cooling scheme presented in section 2.1 requires the use of two different light wavelengths. The *cooling light* drives transitions between $|F = 2\rangle \rightarrow |F' = 3\rangle$ hyperfine states. The *repumper light* acts

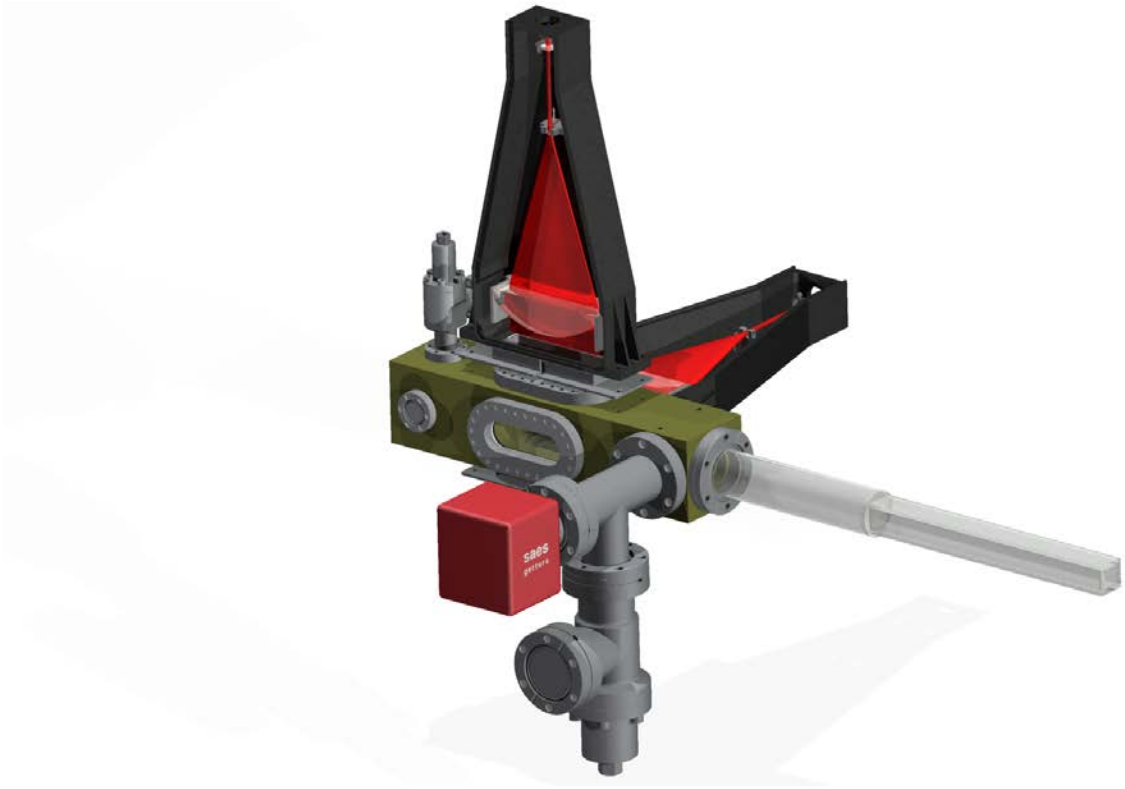

(a)

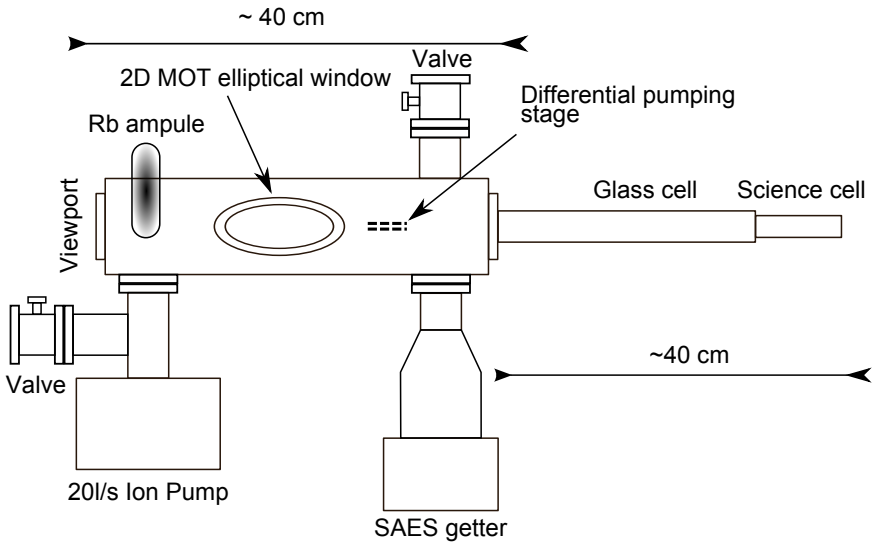

(b)

Figure 2.3: Figure (a) shows the CAD design of the vacuum chamber. A more detailed schematics of the chamber is showed in figure (b). The two valves are used to rough out the system before the baking stage. They are UHV valves from VAT. The total length of the set up is $\approx$ 80cm. The differential pumping tube was machined directly on the titanium chamber, and it is shown with dash lines in the sketch.

on the $|F = 1\rangle \rightarrow |F' = 2\rangle$ (see figure 1.1). If the polarization of the cooling light is chosen to be σ^+ polarized, it will drive a cyclic transition between the states $|F = 2, m_F = 2\rangle \rightarrow |F' = 3, m_F = 3\rangle$. However, the decay of atoms from the $|F = 2\rangle$ to the $|F = 1\rangle$ state is unavoidable. In order to 'close' the transition and increase the efficiency of the cooling mechanism, we need to introduce the repumper light to bring the atoms that are lost in the $|F = 1\rangle$ state back into the cooling cycle. The light that we use needs to be precisely controlled both in power and frequency to address the correct transition. The bandwith of the light source needs to be smaller than the linewidths of the transitions. In the case of ^{87}Rb the linewidth of the cooling transition is $\Gamma \approx 6.066$MHz. External Cavity Diode Lasers (ECDL) are a common choice for atomic physics experiments because they usually have a narrow linewidth $\sim$ 1MHz and an acceptable power output $\sim$ 50mW. Their frequency can be tuned by changing the voltage applied to a piezo-transducer. This allows for an easy implementation of a frequency locking technique using an electronic servo loop.

2.3.1 780nm laser system

As mentioned before, the laser system of light with a wavelength of 780nm is used to trap, cool and transfer the atoms in the 2D-3D MOT stages and also to probe them. The light sources are three commercial TLB-6900 VortexII^{TM} ECDL's from New Focus. Their output power ranges from 15mW to 35mW. They have single mode, linearly polarized outputs, and their linewidth was measured to be $\simeq$1 MHz. In order to stabilize their frequency we adopt the following locking scheme: one laser acts as a *master* laser and it is locked to the peak of the cross-over transition of the $|F = 2\rangle \rightarrow |F' = 3\rangle$ absorption line (CO23) of a frequency modulated (FM) spectrum of ^{85}Rb (see figure 2.4). A commercial LB1005 PID controller box from New Focus is used to close the feedback loop. The other two *slave* lasers are locked to the master laser using an offset-lock technique based on [71]. The general locking scheme for the master and one of the slave lasers is shown in figure 2.6a.

The error signal is derived from a beat signal between the master laser and each one of the slave lasers. The signal is generated by beating a small fraction of the two laser outputs to a fast photodiode with a wide bandwidth of 7GHz (Hamamatsu), connected to a bias-Tee (Mini-Circuits). The electronic signal generated by the photodiode will contain the sum of the two signals $\nu_1 + \nu_2$ and its multiples, and the difference $\nu_1 - \nu_2$ and its multiples. We require the signal to be at a frequency corresponding to the difference between the ^{85}Rb cooling transition and the ^{87}Rb cooling(repumper) transition, which is $\approx 1.7(5.3)$GHz respectively. The difference signal is mixed with a reference signal provided by a VCO using a frequency mixer (ZMX-10G+). The error signal is generated by the electronic circuit shown in

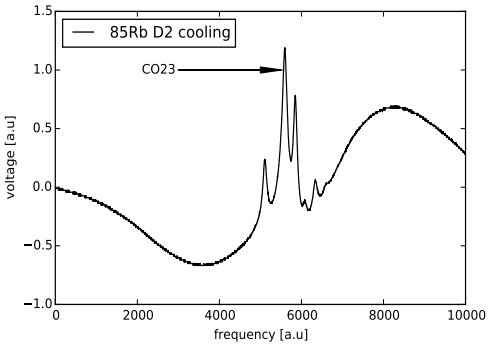

Figure 2.4: Saturated absorption spectrum of ^{85}Rb showing the hyperfine transitions of the cooling line. We lock our master laser to the CO23 feature in the cooling of the ^{8}5Rb D2 line.

figure 2.6a, that has been adapted from in [71]. The DC output of this board is the frequency dependent error signal that we use to lock the slave lasers to the master. To produce the error signal, on the board, the mixed signal (reference and beat signal) is split in two branches. In one of the branches, the signals passes through a high pass filter and converts it into a DC frequency dependent signal with a steep slope and a zero crossing point (set by the filter). The other branch is also converted into a DC signal using the same configuration of diode, resistors and capacitors. The second branch is used for normalization. The error signal as a function of the input frequency is shown in figure 2.6b for different input powers. The zero crossing point of the DC output does not depend on the input power and it is $\approx 171\,\mathrm{MHz}$. It is set by the high pass filter frequency of the circuit, which is controlled by the attenuation of the two branches. On the other hand, the slope of the signal depends on the input power. A higher slope allows for faster and more robust corrections of the frequency deviations.

The actual frequency of the laser can be calculated combining all the changes applied to the frequency in the lock scheme and the ones introduced by the AOM's in the optical setup. Fig. 2.5 summarizes these changes. The green arrow is located at the frequency of the master lock, in the CO23 resonance of the D2 line of ^{8}5Rb. The purple arrows are located at the cooling and repumper frequencies. The actual frequency of the lasers is detuned to the red of those transitions by few MHz, indicated in the figure by $\Delta_{1,2}$.

Once the lock is acquired, the frequency of the lasers can be easily tuned by changing the reference frequency, that is provided by a VCO. This technique gives the possibility of tuning the slave laser frequency directly by changing the voltage applied to the VCO (ZX95-1600-W+ for cooling, and ZX95-5540-C+ for the repumper). A drawback of this method can be the limited speed to tune the VCO frequency. This locking scheme allows the locking range to be wider than what we need for this experiment. Our

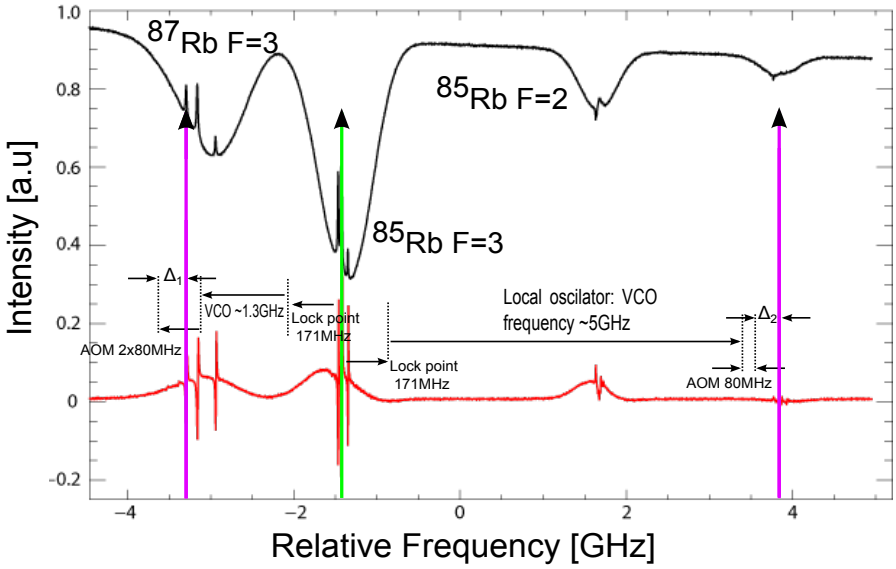

Figure 2.5: Summary of the laser locking and frequency set points in the experiment to lock the repumper and cooling lasers with respect to the master.

typical frequency shifts in the cooling frequency to perform the different stages of the cooling and probing sequence are on the order of $\sim$ 10MHz. The biggest frequency shift is applied to the cooling laser during the dark MOT stage that we use to compress the atoms for efficient loading into the dipole trap, when we have to detune the cooling laser to the red in a linear way by 80 MHz during 100ms before we bring the laser back to resonance for imaging purposes. In the case of the repumper frequency, we do not change its frequency, so it is sufficient to set a constant value to the VCO that is maintanied throught all the experimental sequence.

Once we have fixed the frequency output of the lasers, in order to achieve an acceptable optical power to perform the experiments we need to amplify the laser outputs. Both the cooling and repumper lasers are amplified using two tappered amplifiers TA-700 from New Focus with output powers $\simeq$600mW and $\simeq$100mW. After being amplified, the beams are sent through an AOM in double pass configuration and further split, recombined and coupled into fibers to deliver the light to the experiment. The shcematic of this set up is displayed in figure 2.7 and figure 2.8.

In figure 2.7, the three lasers and two TA are displayed. The Master laser is split in three beams. The first beam is sent to the Rb vapor cell to obtain the FM spectroscopy signal for the lock. The rest of the light is split in two, each beam is mixed with a small fraction of the cooling/repumper laser

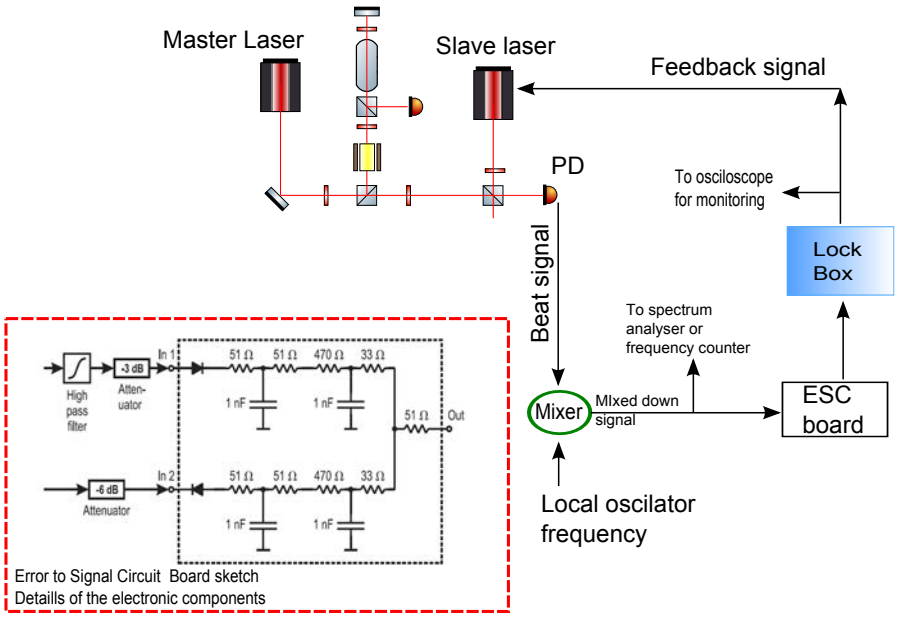

(a)

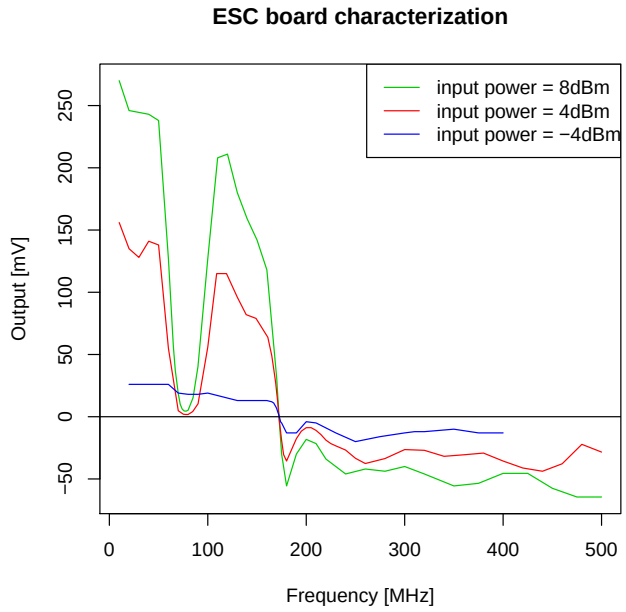

(b)

Figure 2.6: Figure (a) shows the general scheme for the offset lock system. A fast Hamamatsu photodiode connected to a Bias-Tee generates the beat signal between the master and slave lasers (cooling and repumper). This signal is latter mixed with a LO signal generated with a VCO which is controlled from the computer, providing a fast, continuous control over the frequency of the lasers. The error signal is generated in the ESC board from the mixed signal, and sent to the lockbox. The output signal from the lockbox is fed back into the slave laser to close the servo loop. In figure (b) I plotted the output signal from the ESC board as a function of the frequency. The different series correspond to different input powers.

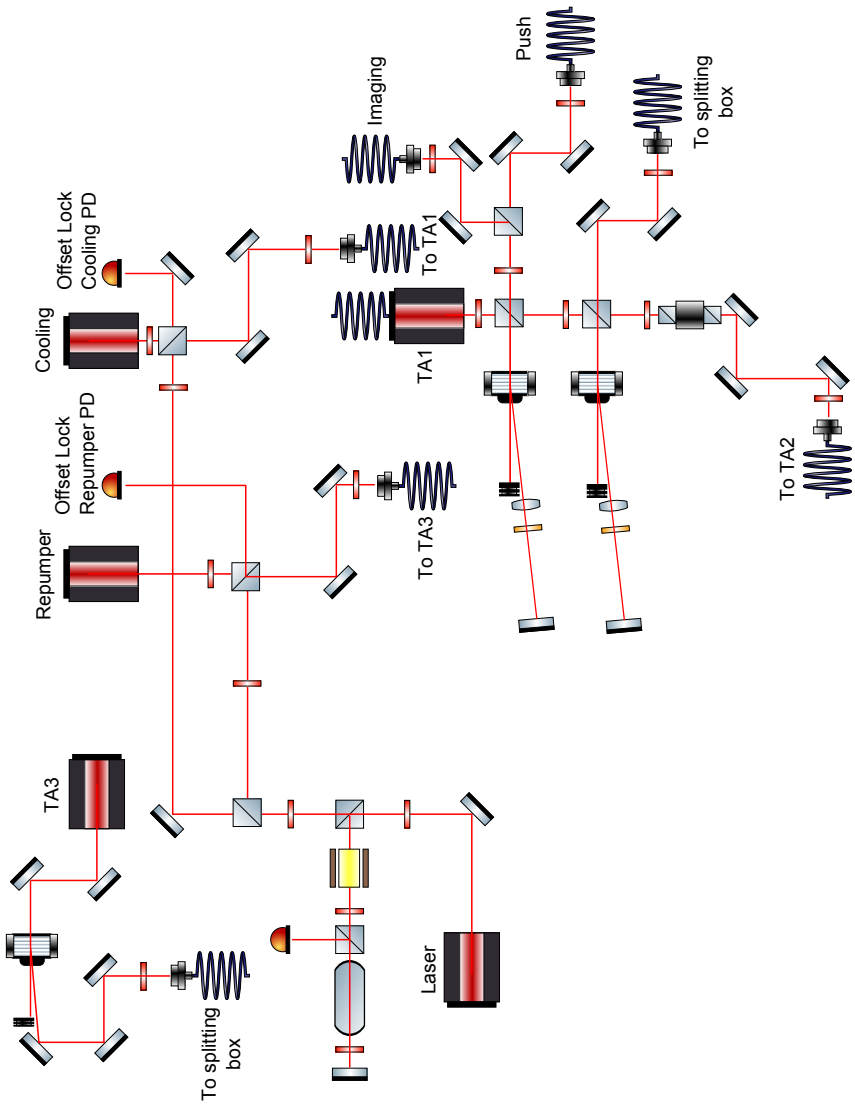

Figure 2.7: Stage 1. Laser sources, locking scheme and light amplification stage.

outputs into two fast photodiodes to create the mixed signals necessary to lock the cooling/repumper lasers. The output of the repumper is also split in two. One part, as mentioned before, is used to create the beat signal for locking. The rest is fiber coupled and sent to feed TA3. TA3 has an output power of $\simeq$ 100mW. This beam is sent through an AOM in double pass configuration before coupling it into another fiber. The latter goes into the splitting box (which is shown in figure 2.8) where it will be further split and combined with the cooling light, as I will explain later. The coolin light, in the same fashion as the repumper, is split in two. The first beam is used to mix it with the master laser light, and the second beam to couple it to feed TA1. The output of TA1 is split in 3 beams: the cooling light for the 3D MOT, the push/imaging beam, and a third beam that is coupled to feed TA2. The 3D MOT cooling beam goes through another AOM in double pass configuration and it is coupled into a fiber which is sent to the splitting box. The push/imaging beam goes through the same AOM configuration as the cooling beam, and afterwards split in two, and each branch coupled into a different fiber. The third beam goes through an optical isolator before we couple it to feed TA2, which is located in the splitting box. The optical isolator helps to avoid any back reflected light from TA2 to contaminate the other beam paths.

In figure 2.8 it is displayed the layout of the splitting box, where we combine the cooling with the repumper light, divide the power between beams and couple them into fibers that deliver the light to the experiment. The TA2 output provides the cooling light which is used for the 2D MOT. Its output goes first through another AOM in double pass configuration. After the AOM it is mixed with one part of the repumper and then coupled into a 1:2 PM fiber splitter. The repumper output, coming from TA3 in Fig. 2.7, is split in two. The first part is combined with the 2D MOT light in a PBS(1) and the rest is combined with the cooling light for the 3D MOT into PBS(2). The cooling output is mixed with the repumper in PBS(2). Then, this combined beam is split into three equal power beams. Each one is coupled to a 1:2 PM fiber splitter.The six outputs make the beams for the 3D MOT system.

A really important issue for a good performance of the experiment is to maintain the polarization of the light fixed. Fluctuations of the polarization are prone to appear when the light is transmitted through a fiber, since the mechanical stress of the fiber and the temperature of the environment can change the refractive index properties of the core, giving rise to fluctuations of the output polarization. Although using polarization maintaining fibers (PM) helps to minimize these effects, some extra precautions must be taken. First, the fibers should be fixed in place applying a small amount of stress to them. Also, to help the temperature of the fibers to be as constant as possible it is good to fix them to the optical

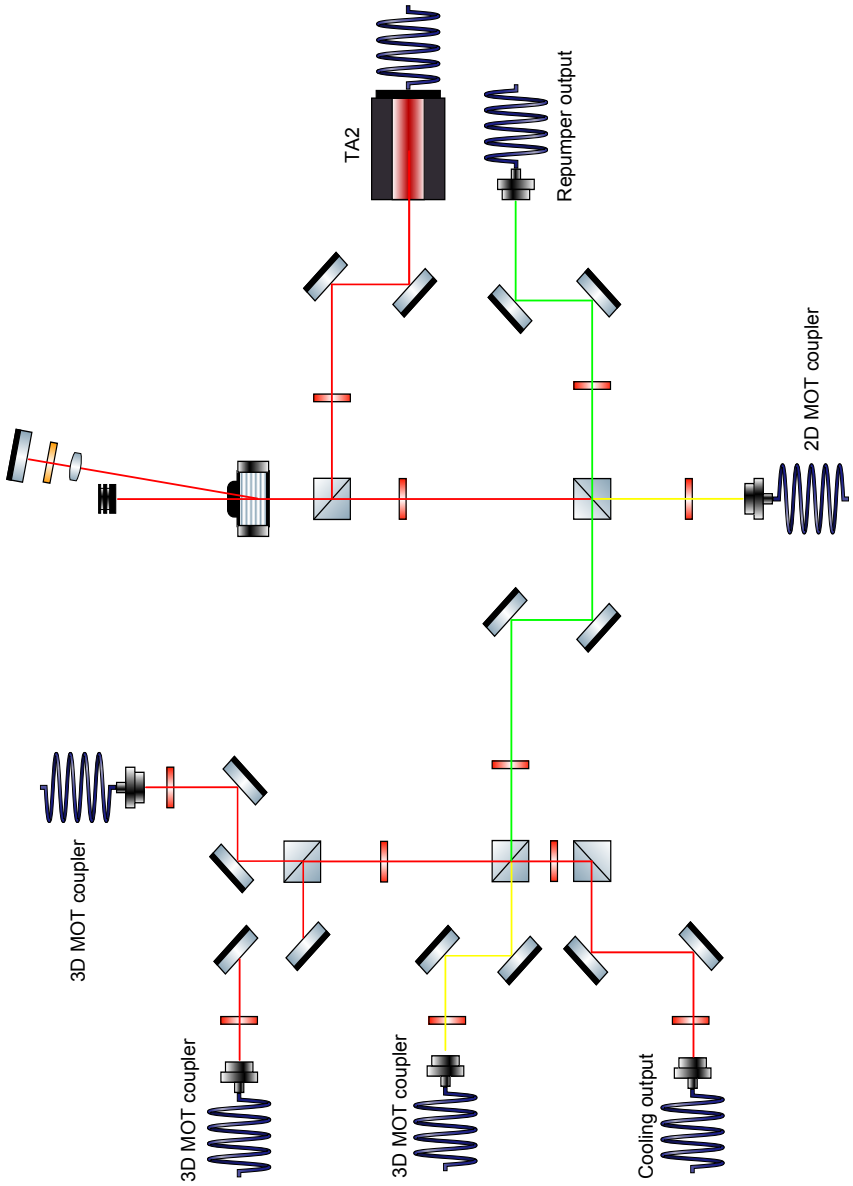

Figure 2.8: Stage 2. Recombination of cooling and repumper light, power division and couplint for the 2D-3D MOT.

table, that acts as a heat sink and is at constant termperature during the day. The laser system must be covered to isolate it from any air flow or temperature fluctuations. The polarization of the light at the input must be aligned wiht the slow axis of the PM fiber. This is done by placing and adjusting a half waveplate in front of each fiber coupler in the experiment.

The optical power available at the experiment is sufficient to have 70mW of cooling light and $\simeq$ 12mW of repumper light in each beam of the 2D MOT. For the 3D MOT, we use $\simeq$15mW of cooling light per beam, and we send a total of $\simeq$ 8mW of repumper light through the vertical beams. The imaging beam has a total power of 1.5mW and the push beam has also 1.5mW. Summarizing, I have presented and described the laser system for cooling. The locking technique is robust, the lasers stay locked during the full day. We can precisely stabilize and control the frequency of the cooling and repumper lights. Overall, the system is good to achieve loading rates of 10^9atoms s^{-1} of the 3D MOT. This is important to have a good repetition rate of the experiment. In 4s, we load $\sim 10^9$ atoms into the 3D MOT with a typical temperature of 350μK.

2.3.2 Dipole trap laser system

During the last stage of Bose-Einstein experiments, forced evaporation is used to cool down the atoms to the quantum regime. Typically, this is achieved either in magnetic or dipole traps. Some experiments also use a combination of the two, with a first stage of evaporation in the magnetic trap after which the atoms are transfered into the dipole trap. In our experiment, we have implemented an all-optical dipole trap to do the evaporative cooling. This method was first developed by Barret [12]. Our experiment can create a pure BEC sample every $\simeq$ 10s. This is quicker than typical experimental sequences using the rf evaporation in a magnetic trap that typically last $\sim$ 1min. It is also more simple, since it removes the need of using a high power rf source and big magnetic coils.

To implement the all-optical evaporation technique (which will be explained in detail in section 3.1) we use a bichromatic cross trap configuration. It is formed by two beams: one at 1070nm wavelength and the other at 1550nm. The former one is produced by an Ytterbium fiber laser (YLR-20 from IPG), which gives an unpolarized output of up to 21W of total power. The 1550nm beam is produced by an ECL laser (SFL1550P) from Thorlabs, with a typical output power of 25mW. The output beam is coupled into a fiber and further amplified using a fiber amplifier (NU-B10-0010). The output of the amplifier is a single mode, polarized 10W beam. We use the 1070nm beam as our primary beam to create a deep potential for the atoms in the first place. The 1550nm beam is needed to provide a tighter confinement in the perpendicular direction to the propagation of the 1070nm beam. This is necessary to succesfully

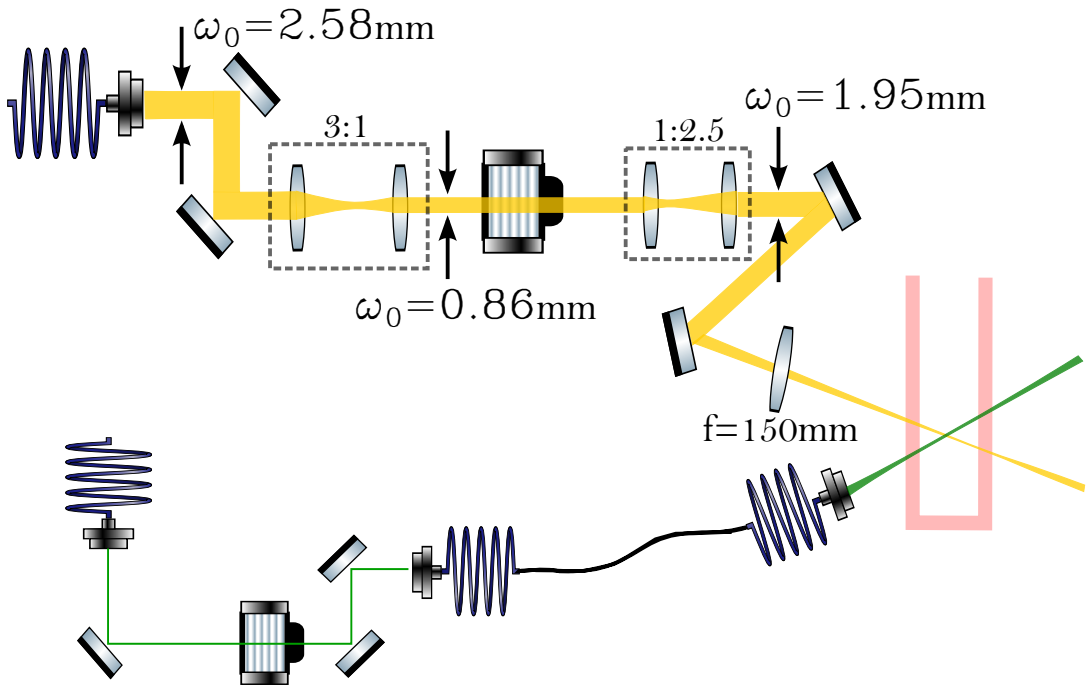

Figure 2.9: Pictorial representation (not to scale) of the dipole trap laser system. The yellow/green beam represent the 1070nm/1550nm beams respectively.

implement the evaporative cooling as we will see later.

As depicted in figure figure 2.9, the 1070nm fiber laser has a collimated output with a $1/e^2$ waist of $w_0 = 2.58$mm. This beam is delivered into the experiment using free-space optics. It is first sent through an AOM (Isomet M1080-T80L) in single pass configuration. The AOM has two purposes: to control the intensity of the light reaching the experiment and to allow for fast switching of the beam. In order to fit the beam within the active aperture of the AOM, the collimated output from the laser is first demagnified using a 3:1 telescope made of two achromatic lenses ($f = 150$mm and $f = 50$mm). After the AOM, another pair of lenses in a 1:2.5 telescope configuration collimates the beam to a waist of $w = 1.95$mm. This beam is sent in free space towards the science cell using a periscope with a precision alignment mirror as the last optical element. A final lens with a focal distance of 150mm is place in front of the glass cell to focuse the beam to an expected waist of $w_f = \lambda \cdot f/\pi \cdot \omega_{Lens} = 26.2\mu$m at the centre of the science cell. The measured waist is reported in figure 2.10a and is $33.1 \pm 0.3\mu$m at the expected

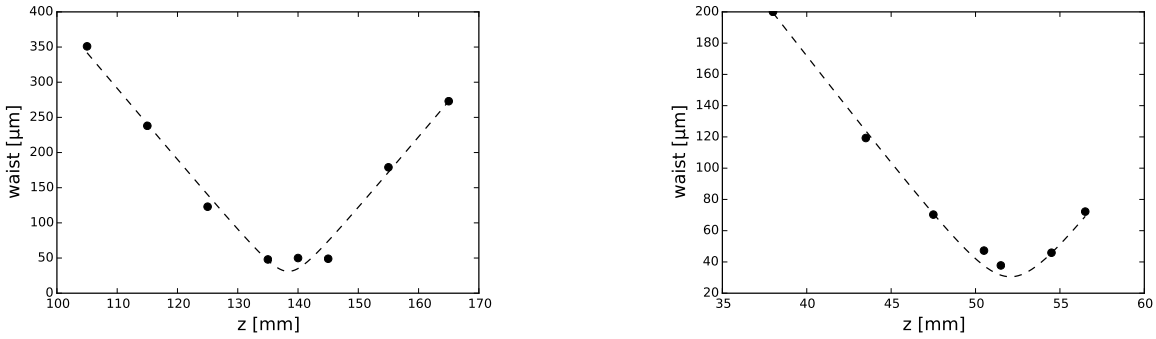

(a) (b)

Figure 2.10: Figure (a) shows the fitting of the $w(z)$ to the measured waists along the propagation axis for the 1070nm laser. The fit gives a waist of $w_0 = 30.0 \pm 0.3\mu$m at a distance of ≈138mm from the focusing lens. Figure (b) shows the corresponding waist measurements for the 1550nm beam propagating after the OZ optics focuser.

position of the atoms. We mount the lens onto a 1-axis translation stage to fine tune the position of the focal point. The total power available before the glass cell is 16W.

The 1550nm beam is sent to another AOM in single pass configuration (Isomet M1099-T50L-1.55) and then it is coupled into a fiber using a high power coupler. The fiber has a pigetailed focuser output (OZ Optics) that focuses the light at a working distance of 52mm from the last lens with a measured waist of $30.5 \pm 0.3\mu$m as reported in figure 2.10b. The available power after the AOM (efficiency ≈ 70%) and the fiber coupling (efficiency ≈ 60%) is 4.5W. The focuser is mounted into a very stable, non-magnetic flexure mount to allow precision alignment of the beam, which is positioned into the breadboard at about 50mm from the center of the science cell. Another 1-axis translation stage is used to adjust the position of the focal point. This beam is sent at an angle of ≃80 degrees with respect to the 1070nm beam, forming the crossed dipole trap.

Combining these two beams into a crossed dipole trap allows us to cool down the atoms from $\sim 100\mu$K to $\sim$ 10nK, and to increase the phase space density of our sample. This makes possible to reach the Bose-Einstein condensation regime within few seconds, as it will be described later.

2.4 2D-3D Magneto-Optical Trap configuration

I have already reviewed the laser cooling mechanism, the vacuum system and the laser systems. In this section I will describe how all these elements work together in our experimental sequence.

The cooling process starts in the 2D MOT chamber. The ^{87}Rb atoms are loaded from the vapour

into the 2D MOT. A 2D MOT consists of a 2-axis MOT in which the atoms are cooled and trapped in two spatial directions. In the direction of the zero-field line, only atoms from a low velocity class are selected. This is because they will not be cooled in any of the other two directions if they pass through the MOT region faster than the cooling cycle. This is a standard configuration which has been extensively studied in the literature and is commonly used in many cold atoms experiments [72, 73]. We use two elliptical beams of approximately 5×2cm that are sent through the rectangular windows of the chamber and then retro-reflected using two rectangular mirrors with a quarter wave-plate in front to set the polarization. This chamber has also a set of anti-Helmholtz elliptical coils mounted around the top and bottom windows to create a cuadrupole field along the symmetry axis of the chamber. The coils give $\approx$10 G/cm at the centre of the chamber while running a current of 5A.

As mentioned before, the light is delivered using optical fibers that already contain light at both cooling and repumper frequencies. Two cylindrical lenses shape the beam output from the fibers. A first lens is placed shortly after the fiber output to expand the beam in the horizontal direction. After $\simeq$ 150mm, a second spherical lens collimates the beam in both vertical and horizontal directions. The two telescopes are mounted directly into the chamber as seen in figure 2.11(a) using a set of screws and springs that allow us to roughly align the cooling axis. Afterwards, the mirrors placed on the opposite sides of the chamber give us the necessary alignment freedom. Two elliptical coils are placed in each cooling direction to allow precise alignment of the field axis with the differential pumping stage.
To transfer the atoms to the science cell, we push the atoms through the differential pumping tube using a *push beam*. This linearly polarized beam has a power of $\simeq$ 1.5mW, and it is carefully aligned with the differential pumping tube. It pushes the pre-cooled atoms from the 2D MOT into the 3D MOT at rate of $\sim 10^9$atoms s^{-1}, as mentioned previously, to load our 3D MOT.

The 3D MOT is in a standard configuration using 3 pairs of counter propagating beams. Each beam is collimated by simple plano-convex lenses to a diameter of 1 inch using a telescope tube. The tubes are mounted on 6 threaded high precision mirror mounts. They are fixed to the optical breadboard with 1 inch aluminium posts. The polarization of the MOT beams have been carefully set to be circularly polarized with the same handness in all beams with respect to the propagation direction. The frequency of the cooling light is detuned to the red $\Delta \simeq -2.5\Gamma$ of the atomic transition.

The quadrupole field is created by a pair of circular coils made of flat wire and mounted on the vertical direction, as shown in figure 2.12. They are supported in a 3D printed plastic arm which is attached to the breadboard. They have 50 turns with a diameter of 6.5cm and a separation of 5cm. They create a field of $\simeq$10G/cm at the center of the chamber when running 2.3A of current. They are switched on and off using a MOSFET triggered with a TTL signal which allows for fast switching off the magnetic field in less

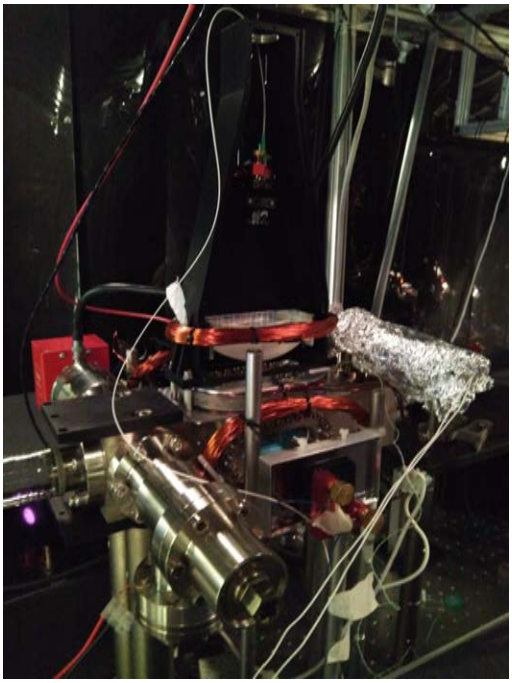

(a)

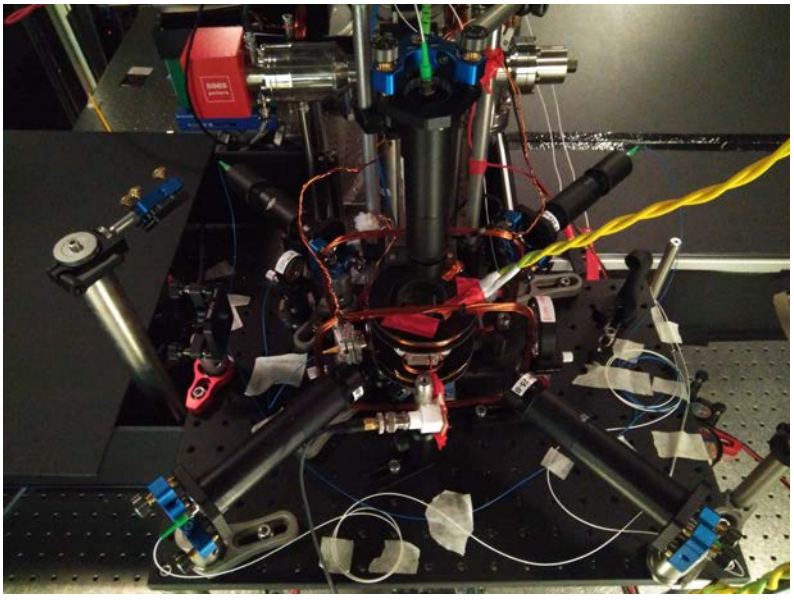

(b)

Figure 2.11: Figure (a) shows the side view of the 2D chamber. The telescope used to create the elliptical beams for the 2D MOT can be appreciated. Also, the sets of coils used to create the quadrupole and compensation fields. The aluminium foil is wraped around the bellow that contains the Rb ampule while it is being heated. Figure (b) is a top view of the science chamber. The MOT telescopes, as well as the MOT coils can be well appreciated. The blue mirror on the left, that is mounted on a thick and tall aluminium post is the second mirror of a periscope that delivers the 1070nm dipole beam into the experiment.

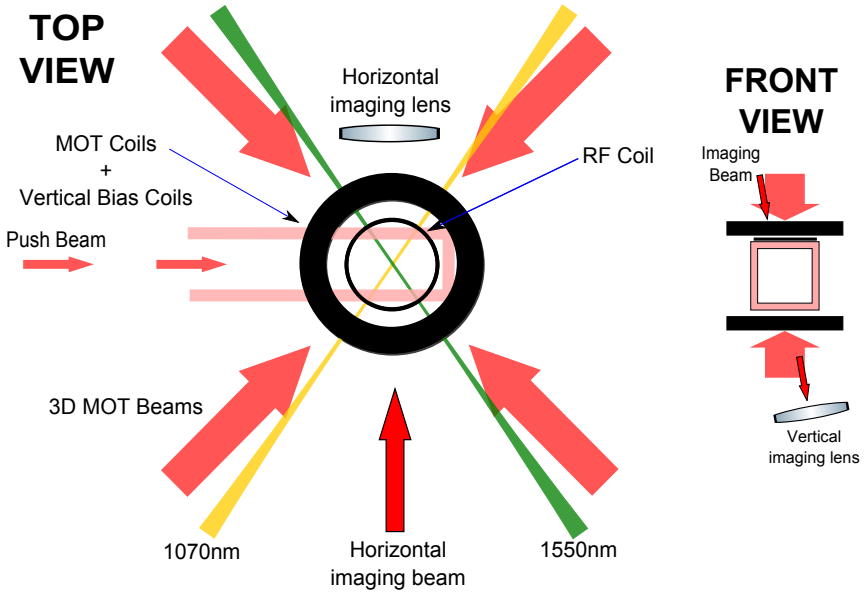

Figure 2.12: Pictorical representation of the dipole trap beams crossing at the center of the chamber at an angle of $\simeq 80$ degrees with the MOT beams and coils.

than 1μs. On top of the quadrupole coils, we have added another pair of coils in Helmhotz configuration in order to correct for the residual magnetic fields in the vertical direction. This compensation coils are supplied with a voltage controlled current source that is able to provide a current of $\pm$10A. They give a field of $3.83G/A$ measured at the centre of the science chamber.

The lifetime of our MOT is $\approx$10s, and the typical temperature of the atoms in the MOT is $\simeq 350\mu$K. The PSD is estimated to be $\simeq 7 \times 10^{-8}$. After the 3D MOT, we transfer the atoms into the dipole trap to perform forced evaporation. To load the atoms efficiently into the dipole trap we need to lower the temperature of the atoms further, which is achieved adding a *Dark MOT* stage that will be described in section 3.2.

To finish this section, I have to mention that we have also placed a small radio-frequency coil very close to the science chamber. This can be used for state preparation of the atomic sample and also as an experimental tool to introduce a coupling between the different states. The coil has a diameter of one inch, and is made of three loops. A capacitor $\simeq 1\mu$F is connected in paralell to make the resonance frequency of the coil be $\omega_{res} = \frac{1}{\sqrt{L_{coil}C}}$. The measured resonant frequency of the coil is $\simeq$ 1.557MHz with a -3dB linewidth of 0.2MHz. Using this frequency, we will need to apply a magnetic field $|B| \simeq 1.557/0.7$G to induce resonant coupling between the states. We use a commercial signal generator (Keysight) connected to a radio frequency amplifier (Mini-Circuits) to generate the frequency.

2.5 Detection

In the previous sections I have described how to create and prepare a cold atomic sample. Now I will describe the *absorption imaging* technique that we use to probe the atomic cloud and extract information from the system. This technique is used in most of cold atoms experiments. This requires to precisely control the exposure time of the camera, and to synchronize it with the experiment. We trigger the exposure of our camera using a digital channel from the computer control system. Our camera is from Allied Vision Technologies (AVT), model Guppy Pro F-031. The CCD chip has 656×492 pixels with a size of 5.6 μm. We control it using a software written in Python, which is a wrapper for the AVT "Vimba C API" available online [74]. This is used with another Python GUI, which reads in the images captured by the camera and processes them to extract the necessary information by performing two dimensional fits to the images.

For absorptionimaging, we use a 3mm collimated beam at a frequency resonant with the $|F=2\rangle \rightarrow |F'=3\rangle$ transition of the D_2 line of ^{87}Rb . The atoms in our condensate are in the $|F=1\rangle$ ground state. Therefore, just before taking the picture, we need to flash some repumper light to drive them into the $|F=2\rangle$ ground state. After a short 15μs pulse of repumper light, the imaging beam is then sent to the atoms. The atoms absorb it and leave a shadow on the beam intensity distribution. This shadow is imaged onto a CCD camera. The amount of light which has been absorbed by the atoms is given by the Beer-Lambert law: $I = I_0 \exp\big[-\int n(z)\sigma dz\big]$, where z is the direction of propagation of the beam, $n(z)$ the density of the cloud, I_0 the intensity of the beam, and $\sigma = \sigma_0/(1+4(\Delta/\Gamma)^2 + I_0/I_s)$ is the absorption cross section with $\sigma_0 = \hbar\omega\Gamma/(2I_s)$ the resonant cross section. $\Omega = \int n dz$ is the column density. For each realization of the experiment, we take three pictures. First, the picture of the imaging beam with the atoms I_1, then one picture of the imaging beam without atoms I_2, and finally another picture with no light and no atoms I_3. We can then calculate the column density of the atomic cloud pixel by pixel as $\Omega(x,y) = -ln[I(x,y)/I_0(x,y)] = -ln[(I_1(x,y) - I_3(x,y))/(I_2(x,y) - I_3(x,y))]$ [75]. Some care is taken during the experiment to take the pictures at an intensity $I_{imaging} << I_s \approx 3.57\text{mW}cm^{-2}$. This is to avoid saturation of the transition.

We image the atoms along both vertical and horizontal directions. The horizontal direction is mainly used for diagnostic purposes and to calibrate the vertical imaging. In the horizontal direction, we use a telescope system with two lenses. A first f = 10cm lens working at its focal distance and another f =30cm placed at 40cm from the first. The CCD chip is located at 30cm from the second lens. With this imaging system we expect to obtain a magnification factor of $m = 3$. We calibrate it as follows.

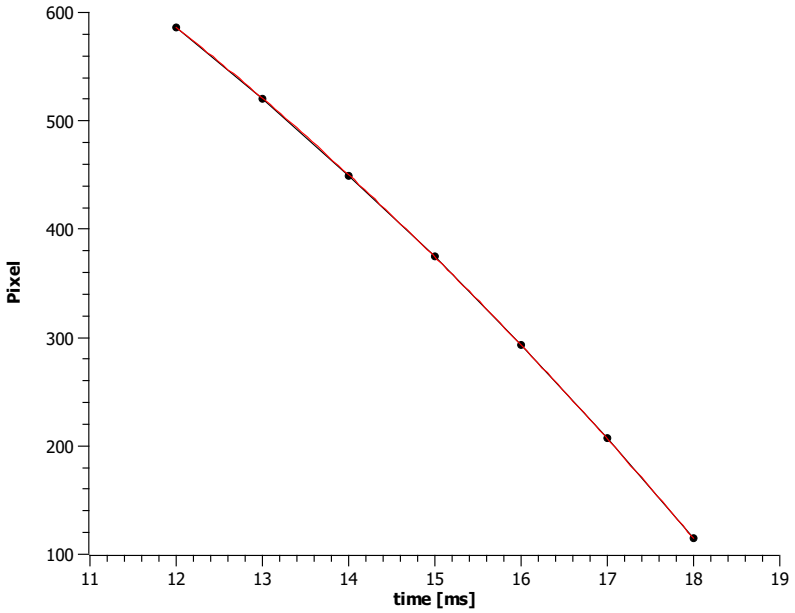

Figure 2.13: Calibrating the magnification of the imaging system looking at the cloud from the horizontal direction using the gravity as a reference. The experimental points corresponding to the center of mass of the cloud for different expansion times is fitted to a quadratic function (red line). $a_2^* = (-2.64 \pm 0.06) pix/ms$.

First, the sample is prepared in the $m_F = 0$ Zeeman substate. Then, we let the atomic cloud fall into gravity for a variable amount of time, and record the position of the center of mass of the atomic cloud in the vertical direction. This is shown in figure 2.13. The experimental points are fitted to a quadratic function cm(t)= $a_0 + a_1 t + a_2 t^2$. Since we know the size of the pixels 5.6μm, and the theoretical curve that the cloud should follow cm(t)= $cm_0 - 9.81t^2 + v_0 t$ we can determine the magnification of the imaging system to be $m = 3.014$. This value is in good agreement with the expected value from our imaging telescope.

The vertical imaging beam is sent to the atoms from the top of the MOT coils at the smallest angle available $\simeq 15^o$. After passing through the cell, a similar telescope made of two achromatic lenses collects the image of the absorption shadow and re-image it on the CCD. To accurately determine the magnification of the vertical imaging system, we compare the radius of the atomic clouds at different TOF for the vertical and horizontal imaging systems. This gives us a ratio of that we can use to determine the magnification of the vertical imaging system.

Another technique that we use for imaging is Stern-Gerlach separation of the clouds to image each Zeeman state independently. We switch on a gradient magnetic field during the time of flight. This gradient magnetic field $\partial_z |B(z)|$ will induce a force on the atoms that depends on the magnetic substate of each atom

$$F_z = \mu_B g_F m_F \partial_z |B(z)| \tag{2.3}$$

In this way, we separate the clouds and we can extract the different column densities of each species. In our experiment, we use the MOT quadrupole field during 26ms of the TOF stage. Typical images of the three clouds obtained by absorption imaging after applying the Stern-Gerlach pulse are shown in figure 3.4. Using the absorption imaging technique, as explained above one can extract the spatial distribution of the optical density $\Omega(x, y, t = TOF)$ of the sample which is related to the density distribution of the atoms. We can extract all the relevant physical parameters of the system performing 2D fits to the optical density profile.

The fitting function will be determined by the conditions of the experiment. If the temperature of the atoms is $T > T_c$, the density of the cloud is expected to have a gaussian distribution, related to the optical density in the following way

$$\Omega = \sigma_0 \frac{N}{2\pi\sigma_x\sigma_y} \exp\left[-\frac{(x-x_0)^2}{2\sigma_x^2} - \frac{(y-y_0)^2}{2\sigma_y^2}\right] \tag{2.4}$$

Where N is the total number of atoms, σ_0 is the absorption cross section as defined earlier, and σ_x, σ_y are the widths of the cloud. From the fitting amplitude and widths we can then extract the total number of atoms N. The widths of the cloud are related to the temperature of the atoms, because the density distribution in TOF reflects the momentum distribution of the cloud at $t = 0$s. The momentum distribution of the atoms always follows a Maxwell-Boltzmann distribution $f(\vec{p}) \propto e^{-\frac{\vec{p}^2}{2\sigma_{\vec{p}}^2}}$, and the width of that distribution is related to the cloud temperature.

$$\sigma_{TOF}^2 = \sigma_0^2 + \frac{TOF^2 T k_B}{m} \approx \frac{TOF^2 T k_B}{m} \tag{2.5}$$

where T is the temperature of the cloud at $t = 0$ms, k_B is the Boltzmann constant and m the mass of the atoms. The approximation assumes that the cloud size at $t = 0$s is small compared to the cloud after TOF ($\sigma_0 << \sigma_{TOF}$). Using this approximation we can calculate a higher limit for the temperature of the cloud.

If $T << T_c$, and all the atoms are condensed the initial momentum distribution of the atoms is zero by definition. In this case, the shape of the cloud can be approximated using the Thomas-Fermi profile, with the condensate density given by

$$n_{TF} = \max\left(\frac{\mu - U_{trapping}}{g}, 0\right) \tag{2.6}$$

where μ is the chemical potential and g is the one-body s-wave interaction parameter. The column density distribution can be expressed as

$$\Omega = n_{TF}^{0} \max\left(1 - \frac{(x-x_0)^2}{r_x^2} - \frac{(y-y_0)^2}{r_y^2}, 0\right)^{3/2} \tag{2.7}$$

In the regime where the temperature of the atoms is similar to the condensation temperature ($T \simeq T_c$), the cloud will have a condensed fraction and a thermal fraction. In this case, we apply a bimodal fitting, that consists on the sum of a 2D gaussian plus a Thomas-Fermi distribution. This allows us to determine the fractional populations of the condensate and thermal parts of the clouds.

2.6 Control system

The computer control system of this experiments is based on National Instruments DAQ cards and the software developed at MIT, called **"Cicero Word Generator"** [76]. The use of such a program has the advantage of using off the shelf components available at a relatively low cost. It is easy to implement and to use it.

The hardware that we use are National Instruments I/O DAQ cards mounted on a PXI-e 1602Q chasis. The analog card is a PXI-6713 which provides eight 14-bit analog outputs with a voltage range from -10V to +10V. The digital card is a PXIe-6535 that has 32 channels with a high level signal output of 3.3V. The chasis is connected to the control computer. To provide a variable timebase reference clock the software requires an external FPGA (Opal-Kelly XEM3001) connected to the computer digital card with a BNC cable and to the computer via USB. The reference clock is set to 10MHz, which means that the achievable resolution of our experimental sequences is 0.2μs. The output of the cards are connected to home-made breakout boards that are later buffered and isolated from the PXI. The analog buffers provide up to 50mA on each channel, with a frequency bandwidth of 10MHz. The software, developed at MIT, consists on two C# different programs, that are available in [77]. Atticus is the name of the server that communicates with the PXI cards. Cicero is the software that writes the instructions that Atticus converts into buffer instructions and sends them to the PXI cards.

CHAPTER 3

ALL-OPTICAL REALIZATION OF A BOSE-EINSTEIN CONDENSATE

Experimentally, the realization of Bose-Einstein condensation implies increasing the phase-space density PSD= $n\lambda_{th}^3$ to values ~ 1. After we have cooled the atoms in the 3D MOT (PSD$\simeq 7\times10^{-8}$), we still need to increase the PSD by several orders of magnitude to achieve Bose-Einstein condensation. To this end, we use the evaporative cooling technique. This is a well stablished procedure that is implemented in every BEC experiment [78, 79]. The process of evaporative cooling is intuitively simple. It consists in removing the hottest atoms from the trap, and wait sufficient time for the remaining ones to thermalize through elastic collisions. This brings down the average energy distribution of the atoms. The efficiency of the evaporative cooling process is a trade-off between elastic collisions leading to thermalization and collisions with the background gas that induce losses. Using this technique, one can achieve a reduction of several orders of magnitude in the temperature at the price of loosing atoms. This process is realized in two ways: radio-frequency evaporation in a magnetic trap and evaporation in a dipole trap, where the trapping potential is created by the light intensity distribution of a powerful laser. In our experiment, we have chosen this latter, since it circumvents the use of bukly and power-consuming magnetic coils, simplifying the experiment and increasing the repetition rate. Our evaporative cooling stage exploits a crossed beam configuration as in [80]. The two beams have different wavelengths, 1.07μm and 1.55μm. This method of evaporative cooling was first achieved in [12]. Since then, a variety of experiments have successfully employed this technique to condense several atomic species [81–83].

In this chapter, I will present the main milestone of my thesis work, which is the all-optical realization of a spinor Bose-Einstein condensate of ^{87}Rb . In section 3.1 I will present the basic principles of the all-optical dipole trap setup that we use. The crossed beam configuration will be discussed and justified. The trap will be characterized later in section 3.3. In section 3.2 I will describe the evaporation path

that we follow to achieve the Bose-Einstein condensation. In section 3.3 I will present some important measurments that characterize the condensates such as the lifetime, the trapping frequencies and the transition temperature.

3.1 Basic principles of dipole traps

The all-optical trapping mechanism is based on the dipole force that a powerful and far-off resonant light field induces on the atoms. The presence of the light field induces a shift of the atomic energy levels, also called **a.c Stark Shift**. Unlike the scattering force, the dipole force exerted by a light field into an atom is not dissipative and can be used to directly trap the atoms in the potential created by the intensity distribution of the light field. Another advantage of this trapping mechanism is that, under the correct conditions, the trapping potential is independent of the internal state of the atoms. This allows to obtain samples of multi-species Bose-Einstein condensates after the evaporation process. In general, the force exerted on the atoms by the light field is [84]:

$$\vec{F}_d = -\nabla U_d(\vec{x}) \tag{3.1a}$$

$$U_d = -\frac{Re(\alpha)}{2\epsilon_0 c} I(\vec{x}) = \Delta E_{a.cStark} \tag{3.1b}$$

with α the complex polarizability of the atoms, ϵ_0 the permitivity in free space, c the speed of light in vacuum and $I(\vec{x})$ the intensity of the light field. For alkali atoms with a complex hyperfine structure, like ^{87}Rb, to compute the U_d it is necessary to take into account the contribution to the polarizability from both D_1 and D_2 lines. If the detunings are large compared to the excited state hiperfine splitting $\Delta \gg \Delta'_{HFS}$ such as in our setup, the dipole potential and the scattering rate due to the far-detuned light can be expressed as

$$U_d = \frac{\pi c^2 \Gamma}{2\omega_0^3} \left(\frac{2 + \mathcal{P} g_F m_F}{\Delta_{D2,F}} + \frac{1 - \mathcal{P} g_F m_F}{\Delta_{D1,F}} \right) I(\vec{x}) \tag{3.2a}$$

$$\Gamma_{sc} = \frac{\pi c^2 \Gamma^2}{2\hbar\omega_0^3} \left(\frac{2 + \mathcal{P} g_F m_F}{\Delta^2_{D2,F}} + \frac{1 - \mathcal{P} g_F m_F}{\Delta^2_{D1,F}} \right) I(\vec{x}) \tag{3.2b}$$

where g_F is the Landé factor, $m_F = 0, \pm 1$ is the projection of $\mathbf{F}$ along the quantization axis for each state, $\Delta_{D1,D2,F} = \omega_i - \omega$ are the detunings with respect to the two D_1 and D_2 lines, and $\mathcal{P}$ represents

the polarization of the light. $\mathcal{P} = 0$ for linearly polarized light (π), and $\mathcal{P} = \pm 1$ for circularly polarized light ($\sigma^{\pm}$). ω_0 is the central frequency of the transition. The scaling laws of the potential and scattering rate are $U_d \propto \frac{I}{\Delta}$, and $\Gamma_{sc} \propto \frac{I}{\Delta^2}$. This means that we can increase the power of the light fields as soon as we keep the detuning large enough to avoid the scattering rate to become large. This is important since the scattering constitutes a heating mechanism of the atomic sample. The heating rate due to the scattering is $\frac{\Delta T}{\Delta t} = \frac{2}{3}\frac{T_{recoil}}{\Gamma_{sc}}$ [84]. In our case, because of the large detuning that we choose, this effect is negligible.

If the beam is a gaussian beam, we can write the intensity $I(\vec{x})$ as

$$I(\vec{x}) = \frac{2P_0}{\pi w^2(z)} \exp\left[-\frac{2r^2}{w^2(z)}\right] \tag{3.3}$$

where $r^2 = x^2 + y^2$, z is the propagation direction, and $w(z) = w_0\sqrt{1 + \frac{z}{z_R^2}}$ is the waist of the beam along the propagation direction. $z_R = \frac{\pi w_0^2}{\lambda}$ is the Rayleigh length. λ is the wavelength of the light, and P_0 is the total power of the beam. In a red detuned trap where $\Delta = \omega - \omega_0 < 0$, the atoms will be attracted to the maximum of the light intensity, which means the waist of the beam. The trapping potential at the position of the beam waist can be approximated as a harmonic potential with axial symmetry. Expanding the expression of the potential in equation 3.2(a) up to first order with respect to r/w_0 and z/z_R:

$$U_d \simeq -U_0\left(1 - 2\left(\frac{r}{w_0}\right)^2 - \left(\frac{z}{z_R}\right)^2\right) \tag{3.4}$$

where $U_0 = |U_d(\vec{x} = 0)|$ and the negative sign implies red detuning of the trapping light with respect to the resonance. The harmonic potential in equation 3.4 is characterized by the trapping frequencies:

$$\omega_r = \sqrt{\frac{4U_0}{mw_0^2}} \tag{3.5a}$$

$$\omega_z = \sqrt{\frac{2U_0}{mz_R^2}} \tag{3.5b}$$

The ratio between the trapping frequencies $\omega_r/\omega_z = \sqrt{2}\pi\frac{w_0}{\lambda}$. This slows the thermalization process as it will be discussed later. The way to overcome this problem is using two beams propagating in orthogonal directions. The second beam will provide tight confinement also in the axial direction of the first beam. In the case of two gaussian trapping beams crossing at 90°, beam 1 propagating along the $\hat{z}$ axis and beam 2 along the $\hat{y}$ axis, the potential resulting from the combination of the two can be approximated up to the second order:

$$U_{cross} \simeq -U_{0,1} - U_{0,2} + \left(\frac{2U_{0,1}}{w_{0,1}^2} + \frac{2U_{0,2}}{w_{0,2}^2}\right)x^2 + \frac{2U_{0,1}}{w_{0,1}^2}y^2 + \frac{2U_{0,2}}{w_{0,2}^2}z^2 \tag{3.6}$$

And the corresponding trapping frequencies are given by

$$\omega_x = \sqrt{\frac{4U_{0,1}}{mw_{0,1}^2} + \frac{4U_{02}}{mw_{0,2}^2}} \tag{3.7a}$$

$$\omega_y = \sqrt{\frac{4U_{0,1}}{mw_{0,1}^2}} \tag{3.7b}$$

$$\omega_z = \sqrt{\frac{4U_{0,2}}{mw_{0,2}^2}} \tag{3.7c}$$

$$\tag{3.7d}$$

These expressions do not include the effect of gravity. This adds a tilt to the trapping potential along the vertical direction, and all the expressions become more complicated. Alternatively, we have calculated the trapping potentials numerically including the effect of gravity and the fact that our beams do not cross exactly at 90°. Our two laser beams are both far detuned from the D_1 and D_2 lines. The 1070nm beam has a completely unpolarized output, while the output of the 1550nm beam is linearly polarized. In figure 3.1, I have plotted the crossed beam trapping potential geometry as a function of the vertical and horizontal directions for beam powers of $P_{1550} = 155$mW and $P_{1070} = 61.5$mW, corresponding to the final trapping powers of our experimental sequence, and I have assumed a crossing angle of 80°. I used the formulas given above assuming that both laser beams are independent and do not interfere with each other.

3.2 All-optical evaporative cooling and realization BEC

After the 3D MOT stage, we need to transfer the atoms into the dipole trap to start the evaporation process. We start with a single beam. As mentioned in section 2.1, to efficiently load the dipole trap we add a Dark MOT stage of 80ms. During this time the MOT is compressed, and the atoms can achieve sufficiently high PSD to start the evaporation stage.

3.2.1 Dipole trap loading

As mentioned in section 2.1, we load our dipole trap from a compressed MOT. The most powerful 16W, 1070nm beam focused to a waist of 33μm is kept on during the MOT loading. After typically 5s of

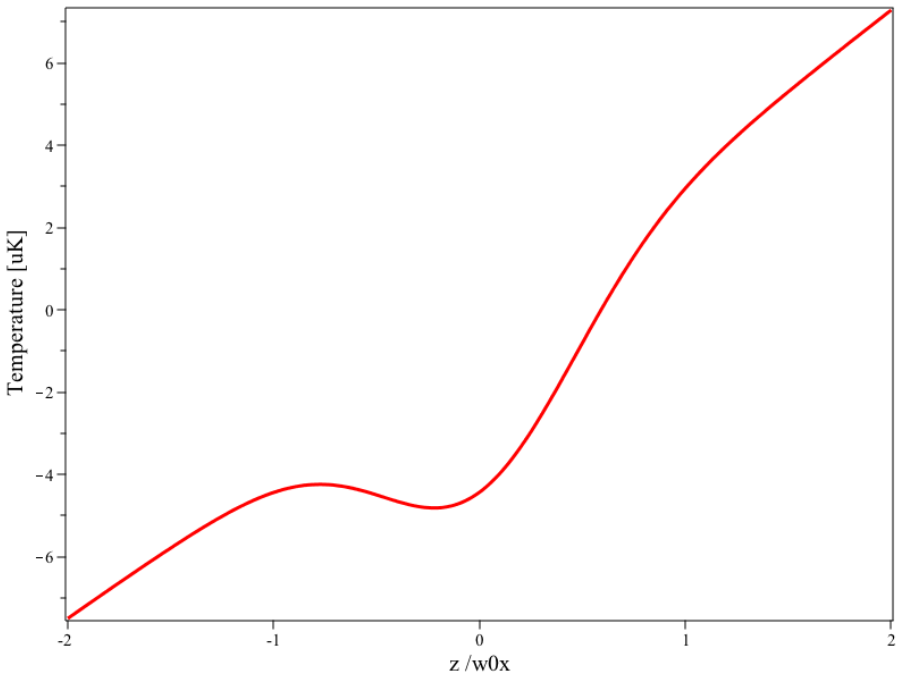

(a)

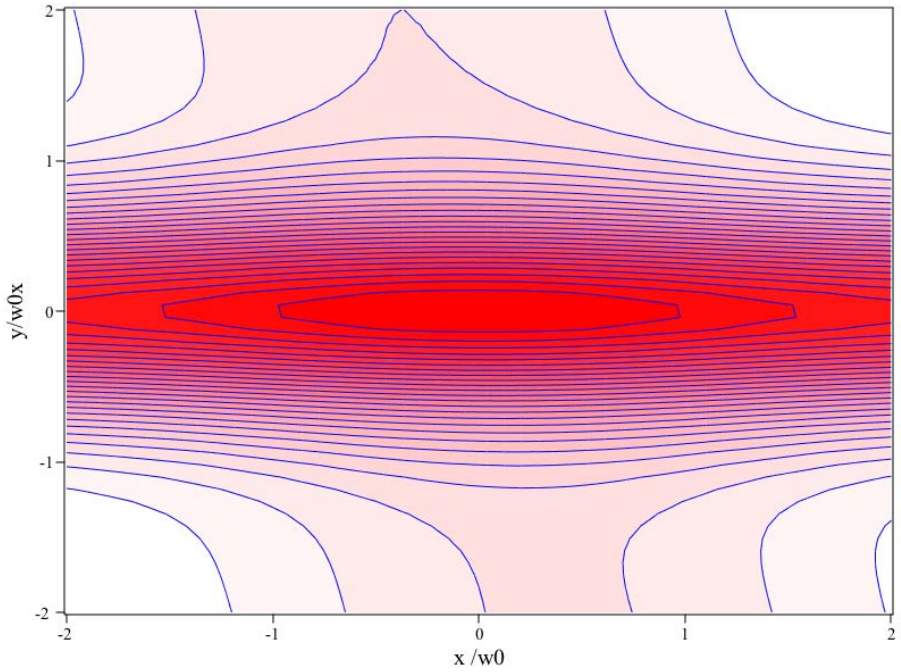

(b)

Figure 3.1: Figure (a) shows the trap depth including the effect of gravity, as a function of the height z, with z=0 being the centre of the trap. In figure (b) the equipotential contour lines of the function are plotted as a function of the horizontal spatial directions.

loading, the MOT has $\simeq 10^9$ atoms at a temperature of $\approx 350\mu$K. The MOT is then compressed by detuning the cooling light frequency from its value during the MOT ($\Delta \approx -2.5\Gamma$) to $\Delta \approx -10\Gamma$ in 80ms, and lowering the repumper power to $\approx 20\mu$W cm^{-2}. The repumper light is turned off a few μs before the cooling light to ensure that the atoms are pumped to the $|F = 1\rangle$ manifold. At the end of the Dark MOT stage, we have $\sim 10^8$ atoms at a typical temperature of 50μK. This results in an increase of the PSD to $\simeq 3 \times 10^{-6}$, that helps to start the evaporation process in more ideal conditions. The dipole trap is then loaded, and we measure the number of atoms after 50ms of thermalization to be $\sim 10^7$. This is a rough under estimation because the anisotropic geometry of the single beam makes the assessment difficult.

Before starting to optimize the evaporation, we need to align the dipole beams to cross. The alignment process is performed as follows. First, we shine the 1070nm beam at full power during the MOT loading and detect the atoms after a very short TOF $\sim 0.5\mu$s using absorption imaging, until we see the beam structure in the picture. This is almost straightforward after taking some care to prealign the beam with respect to the 3D MOT. Then we to do the same with the 1550nm beam. Once we can see both beams within our field of view, we start the evaporation ramp with the 1070nm beam. As we will discuss later, the power of the beam is ramped down in an exponential way with a time constant of 0.1s. We stop the evaporation after $\simeq 1.2$s, and then we switch on the 1550nm beam at full power. We scan the vertical alignment of the latter until we can observe the cross structure appearing on the CCD (see figure 3.2). From there on, the optimization of the evaporation ramp and the cross alignment can be done iteratively. The figure of merit to optimize during this process is the PSD.

Once the atoms are in the dipole trap, we start the evaporation. We need to choose carefully the way in which we lower the trapping potential. The rate at which it is lowered has to be slow enough to allow the remaining atoms in the trap to thermalize through elastic collisions. The elastic collisional rate is given by

$$\Gamma_c = \sqrt{2} n \bar{v} \sigma \tag{3.8}$$

where $\bar{n} = N\bar{\omega}^3 \left(\frac{m}{4\pi k_B T}\right)^{3/2}$ is the mean density in a harmonic trap [85], being $\bar{\omega}$ the geometrical average of the trapping frequencies, $\bar{v} = \frac{8k_B T}{\pi m}$ is the average velocity of the atoms and $\sigma = 8\pi a^2$ is the elastic scattering cross section with a the scattering length of the atoms. The collision rate scales as $\Gamma_c \sim \bar{\omega}^3 / k_B T$. This rate decreases when lowering the trap depth, because it scales with the trapping frequency that, in turns, depends on the the power. Following [80], we define the parameter $\eta = \frac{U_0}{k_B T}$ as the ratio between the trapping depth and the averaged temperature of the atomic distribution. Lowering the

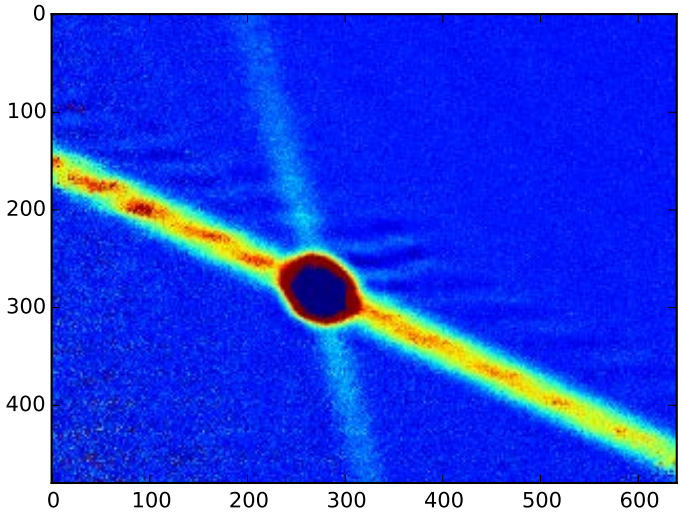

Figure 3.2: The picture shows the crossing beam configuration. After some time of evaporation in the single beam dipole trap, we switch on the crossing beam. The efect of the crossing beam can be appreciated clearly. It increases the trapping frequencies along the axial direction of the most powerful beam, creating a 'bulb' where atoms that were populating the wings of the single beam are then preferentially trapped. The picture is taken after few $\sim$ 5ms of TOF.

trapping potential results in an increase of η, and the thermalization process is slowed down because the most energetic atoms spend more time in the wings of the trapping potential. Typically, the evaporative cooling process does not lead to an increase in the PSD if $\eta \geq 8$. To avoid stagnation of the process, we use the cross beam to increase the thermalization rate. This provides a tighter confinement in the axial direction that increases the rate of elastic collisions and allows the atomic sample to thermalize faster.

Figure 3.2 shows an experimental picture of the crossed beam geometry. We can clearly observe how the weaker beam provides confinement in the axial direction of the most powerful beam. Where the beams cross, the trap becomes deeper, and some of the atoms that were in the wings of the powerful beam gather at the crossing point, forming a 'bulb' with tighter confinement in all directions.

Taking into account the previous considerations, we choose our evaporation ramp as follows. We start the evaporation in the single beam dipole trap by ramping down the power of the 1070nm beam with a linear piecewise ramp as sketched in figure 3.3b. We break down the sequence in linear ramps for simplicity, but we aim to create a ramp that resembles as much as possible an exponential curve.

During the first stage without the crossing beam, we have four ramps, which are summarized in table 3.3a. We decrease the power from 100% to 4% in 3.16s with a time constant $\tau \simeq 0.1$s. At t=2.16s from the beginning of the ramp, we switch on the crossing 1550nm beam with a power of 1.2W that corresponds to 28% of the total power available. We then keep it at a constant power during 2s in the

	Ramp 1	Ramp 2	Ramp 3	Ramp 4	Ramp 5	Ramp 5	Ramp 7
Duration [ms]	90	20	150	900	2000	1500	1900
1070nm end power [%]	48%	31%	16%	7%	4%	1.7%	1%
1550nm end power [%]					28%	9%	5%

(a)

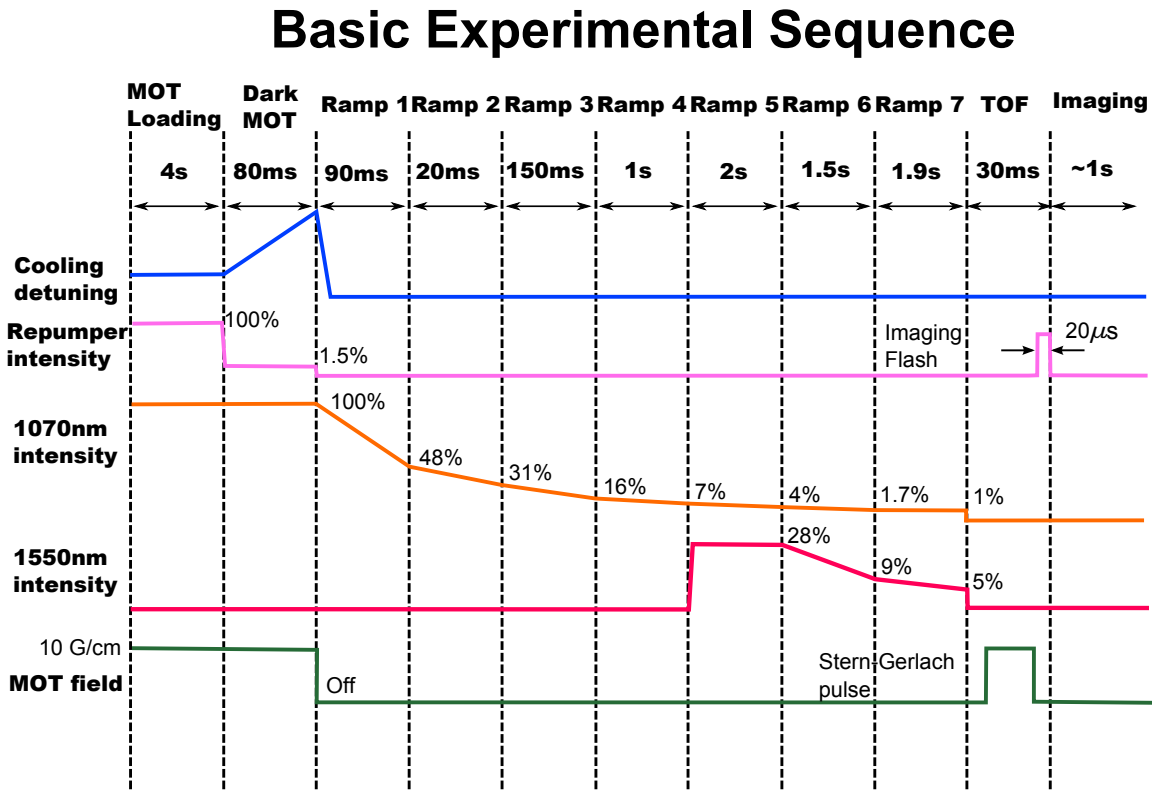

(b)

Figure 3.3: Figure (a) shows the tabulated powers of the dipole trap beams during the evaporation sequence. Figure (b) shows a schematic diagram of the basic experimental sequence to achieve a Bose-Einstein condensed sample of atoms. The most relevant experimental parameters are displayed as a function of time. Within each time step, step-wise of linear ramps are applied to the experimental parameters. The short repumper pulse at the end of the TOF step is to pump the atoms to the F=2 ground state to perform absorption imaging, since the cooling light, used to image the atoms is tuned to the resonance of the $F = 2 \rightarrow F' = 3$ transition.

5th step of the evaporation ramp. From there on, we ramp both beams with time constants $\tau_{1550} \simeq 1.5$s and $\tau_{1070} \simeq 1.15$s. After 6.56s of total evaporation time, we end up with a pure Bose-Einstein condensate of N$\simeq 1 \times 10^5$ atoms in the F=1 spin manifold, as shown in figure 3.4, where we can see a typical BEC picture after TOF=30ms with and without applying a Stern-Gerlach pulse to separate the three different m_F substates.

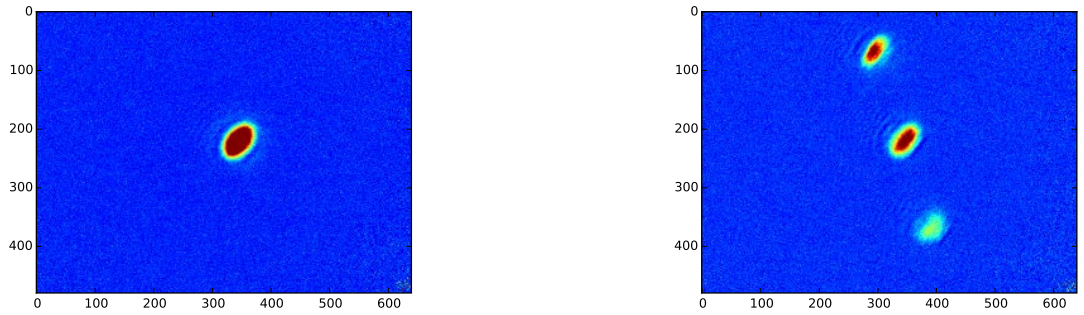

(a) (b)

Figure 3.4: Figure (a) shows a purely condensed BEC sample with $\simeq 1 \times 10^5$ atoms. In (b) it is shown the same sample after applying a Stern-Gerlach pulse during time of flight to separate the three clouds.

In figure 3.7 I have displayed the integrated density profiles of the atomic cloud at different temperatures[1]. The transition from a purely gaussian distribution to a bimodal distribution is clearly visible. The minimum temperature that we can measure is $\simeq$ 150nK. When we have a pure condensate, the typical thermal wings of the bimodal distribution disappear giving rise to a Thomas-Fermi distribution of the measured optical density.

Another typical feature of the BEC is the inversion of the aspect ratio (relation between the widths of the density distribution) during the expansion time. It is clearly observable in our system, as it is shown in figure 3.5. We can see pictures of the cloud for different TOF between 8ms and 28ms. We can appreciate how at 8ms, the cloud is elongated in the perpendicular direction with respect to the elongation axis of the cloud at 28ms. In the two middle pictures for times 12ms and 20ms we can see how the cloud is more or less symmetric, and has a rounded shape. Note that the ring pattern around the cloud in the pictures for short TOF is due to the high densities of the cloud.

In this section, I have describe with detail the experimental path that we follow in our experiment to achieve Bose-Einstein condensation, with an emphasis in the evaporative cooling stage, which has been adapted to our bichromatic crossed configuration.

[1]We say that we are at $T \simeq 0$K when the temperature of the thermal cloud is so small that we can not measure it.

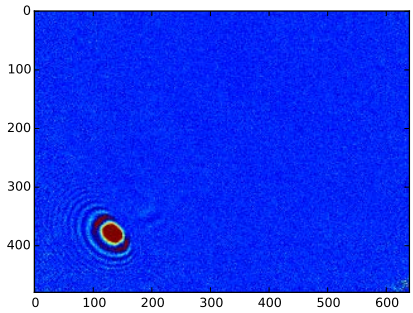

(a) TOF = 8ms

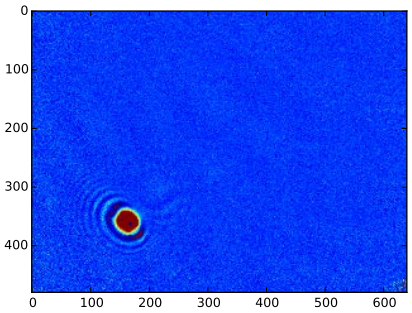

(b) TOF = 12ms

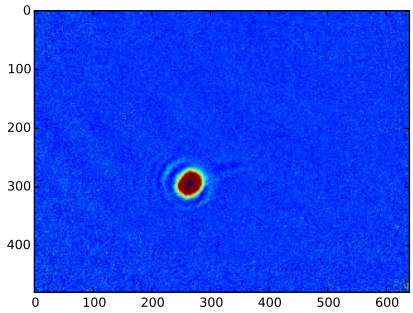

(c) TOF = 20ms

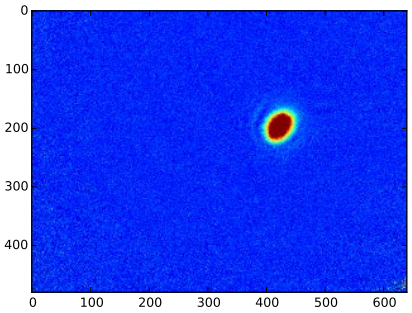

(d) TOF = 28ms

Figure 3.5: Pictures of a pure condensate cloud at different times of flight, showing the change of the aspect ratio during the expansion. This is a typical feature of the BEC that is not observed in non condensed clouds.

3.3 Characterization of the Bose-Einstein condensate

In this section, I will present some characterization measurements of the BEC. In the first place, I will show the measurements of the condensate fraction as a function of the temperature of the clouds. From this, we will be able to determine the transition temperature of our condensate. Then I will measure the trapping frequencies of the trap using two techniques: parametric heating and collective mode excitation. These are important to determine the density, size and chemical potential of the BEC, as described in section 1.2. Then, I will present a measurement of the lifetime, which is important to determine the available time to perform experiments in our system.

3.3.1 Transition temperature

The critical temperature T_c is a function of the trap frequencies $\bar{\omega}$ and the number of atoms N: $k_B T_c = \hbar\bar{\omega}(N/1.202)^{1/3}$. Once the system has reached the critical temperature, the number of condensed atoms grow according to $N_0/N = 1 - \left(\frac{T}{T_c}\right)^3$. In a dipole trap, lowering the power of the beams have two different effects: lowering the temperature of the atoms but also the trapping frequencies. We have established previously (see equation 3.5b) the scaling of the trapping frequencies with the power to be $\bar{\omega} = U^{1/2}\sqrt[3]{(4/m\omega_0^2)(2/mz_R^2)^{1/2}}$. If U is the depth of the trapping potential, the temperature of the atoms scales $k_B T = \chi U$. Typically $\chi \approx 1/6$. Therefore, the condensate fraction in an optical dipole trap as a function of the critical temperature is

$$\frac{N}{N_0} = 1 - \left(\frac{T}{\tilde{T}_c}\right)^{3/2} \tag{3.9a}$$

$$\tilde{T}_c = \frac{1.88\hbar^2 N^{2/3}}{k_B \chi m(\omega_0^2 z_R)^{3/2}} \tag{3.9b}$$

In figure 3.6 I plotted the condensate fraction as a function of the temperature of the thermal cloud for different temperatures set by the depth of the trap. The dashed line is a fit to the data using the function given in equation 3.9b. The points are averaged over three experimental runs and the error bars correspond to the standard deviation. The result of the fit gives us the transition temperature $\tilde{T}_c = 207 \pm 4\text{nK}$.

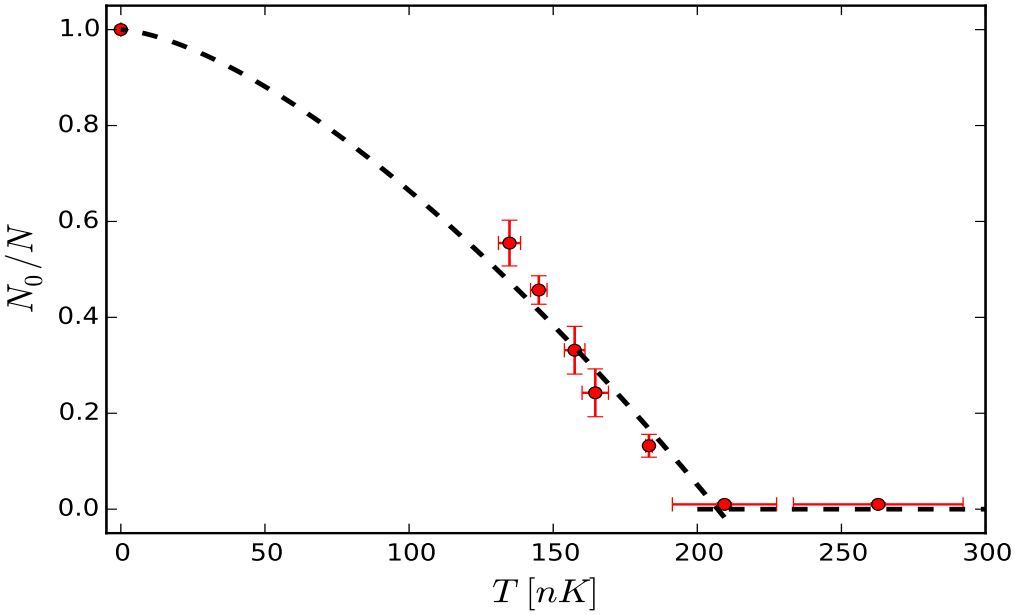

Figure 3.6: The condensate fraction (red circles) is plotted against the temperature of the thermal cloud. Each point is the average over three experimental runs. The error bars correspond to the standard deviation of the measurements. The dashed line is a fit to the data using equation 3.9b.

3.3.2 Trapping frequencies

As discussed in the previous sections the trapping frequencies are very important experimental quantities. The method that we use to determine the high frequencies of the trap is parametric excitation. This consists in applying a sinusoidal modulation to the trapping potential. We realize it by applying the modulation to the amplitude of the 1070nm beam. The atomic cloud will be parametrically excited when the frequency of the modulation is twice the fundamental frequency of the trap [86, 87]. The results of these measurements are shown in figure 3.8. The solid points are averages over three distinct measurements, and the error bars correspond to the standard deviations. To perform the measurement, we stop the evaporation with trapping beam powers of $P_{1550} = 200$mW and $P_{1070} = 100.$mW, slightly above our final trap powers. Then we apply a modulation of $\simeq 10\%$ to the 1070nm beam. The frequency that results in a heating up of the cloud is 510Hz, where the width of the cloud peaks at 70μm, as compared to the baseline of 40μm. We can see that at the same frequency, the number of atoms decreases due to the heating mechanism. Another low peak at 510/2Hz can be observed in the number of atoms. These losses correspond to the fundamental frequency of the trap. At this modulation frequency, no heating mechanism is observed. From these results, we can calculate the corresponding trapping frequencies at the end of the evaporation, where the power of the beams are $P_{1550} = 155$mW and $P_{1070} = 80$mW, taking into account that $\omega \propto \sqrt{P} \rightarrow \omega_{trap} \simeq 2\pi \times 200$Hz.

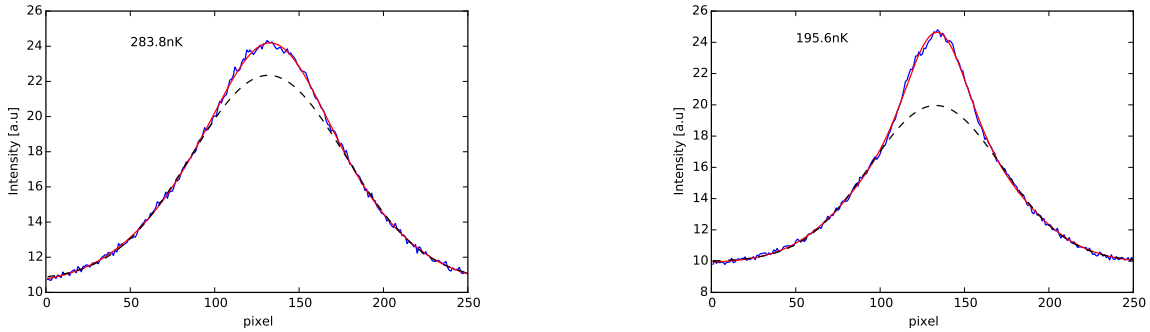

(a) (b) (c) (d)

Figure 3.7: Different integrated density profiles of the atomic cloud are shown for different temperatures across the BEC transition, together with a double fit to the profiles, showing the development of the bimodal distribution. In picture d) the thermal cloud can not be distinguished and it makes the estimation of the temperature difficult.

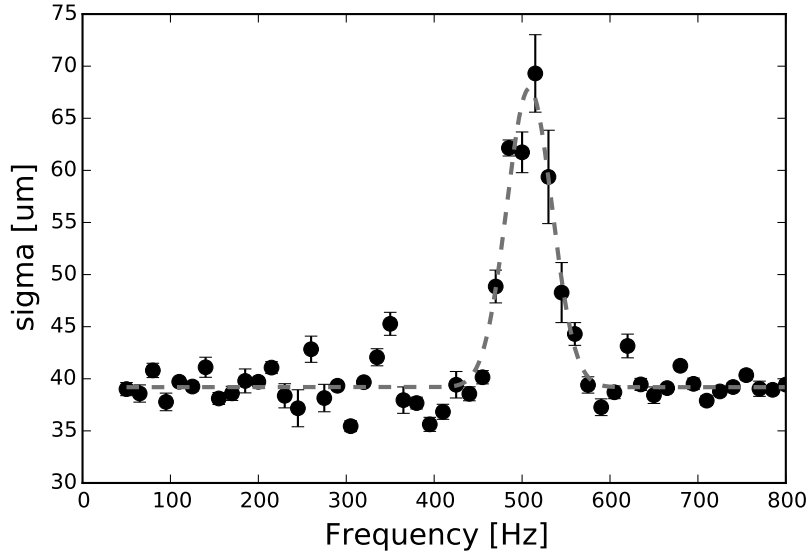

(a)

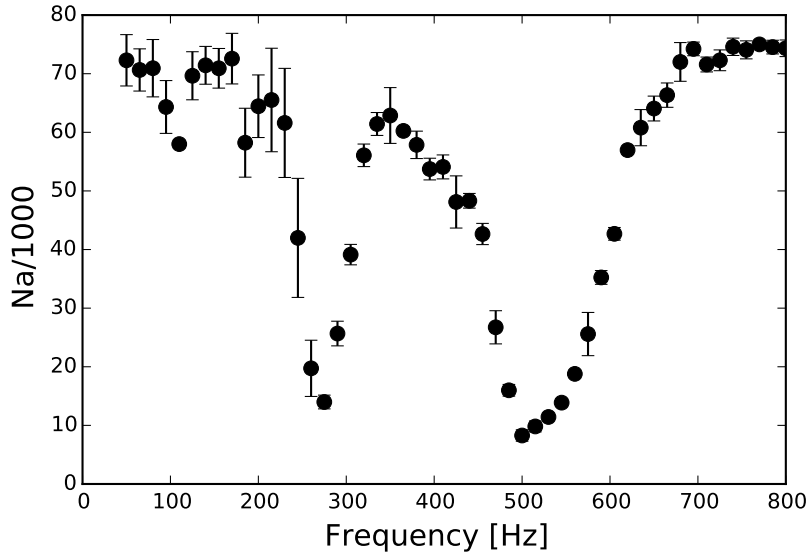

(b)

Figure 3.8: In (a) the figure shows the average width of the atomic cloud measured after 30ms TOF as a function of the modulation frequency applied to the main dipole beam. The error bars are the statistical standard deviations of three measurements. The depth of the modulation applied was $\simeq 10\%$ of the total beam power. The dashed line is a gaussianl fit to the data. We can observe a clear peak in the temperature of the cloud at $\simeq 510$Hz. In (b) the figure shows the number of atoms measured as a function of the frequency. The error bars are the statistical standard deviations of the measurements.

As we can see from figure 3.8 we could observe only the response due to the high frequencies of the trap. This allows to determine the high frequencies of the trap. To measure the low frequency, we

	Measured frequencies [Hz]	Calculated frequencies [Hz]
ω_1	$2\pi\times200 \pm 10$	$2\pi\times$ 233
ω_2	$2\pi\times200 \pm 10$	$2\pi\times$ 235
ω_3	$2\pi\times87 \pm 13$	$2\pi\times$ 42
$\bar{\omega}$	$2\pi\times151 \pm 11$	$2\pi\times$ 131

Table 3.1: Trapping frequencies of the cross potential, both calculated using the theoretical formulas given before and the values found exlperimentally using parametric heating and collective mode excitation techniques for the final trapping laser powers of P_{1550} =155mW and P_{1070} =80mW

use another approach. We excite the collective mode of the condensate and observe the center of mass oscillations of the BEC within the trap itself. The excitation of the collective modes of a Bose-Einstein condensate have been studied in [88]. The center of mass motion is triggered applying a small magnetic field gradient pulse at the end of the evaporation. After the excitation pulse, we wait for a variable amount of time, with the trapping potential fixed and finally we release the atoms to detect the centre of mass of the cloud with a fixed TOF. Experimental results are shown in figure 3.9. The solid points are the average of three repeated measurements and the error bars the corresponding standard deviations, as before. The dashed grey line is a fit to a sinusoidal function. The result of the fit gives an angular frequency $\omega_l = 547 \pm 13$ rad/s.

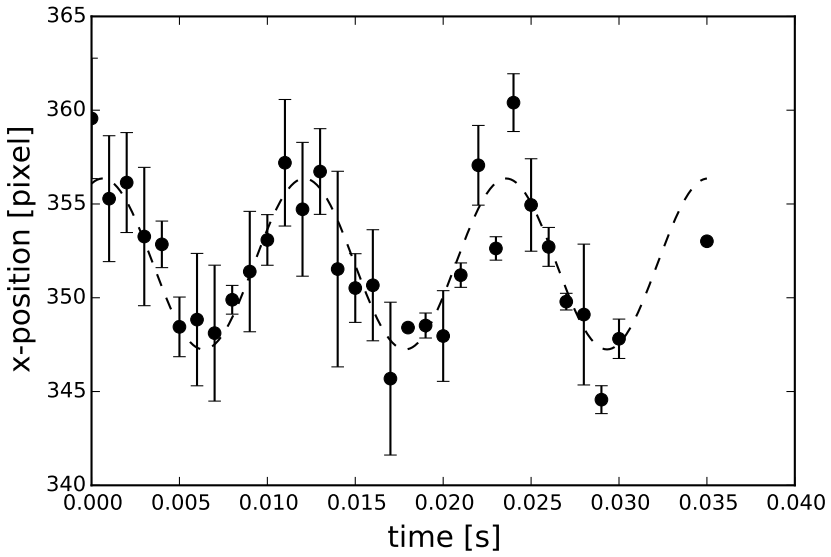

Figure 3.9: The figure shows the centre of mass of the atomic cloud measured after 30ms TOF as a function of the waiting time after the magnetic field pulse is applied. The error bars are the statistical standard deviations of the measurements. The dashed line is a sinusoidal fit to the data, resulting in an angular frequency of $\omega_l = 547 \pm 13$ rad/s.

A summary of the results is presented in table 3.1, where I have summarized the predicted and

measured parameters, that are in good agreement. From the experimental results reported above, we can calculate some useful parameters of our trapped condensate. The theory of interacting trapped Bose-Einstein condensed gases can be found in [69] and references therein. The geometrical averaged trapping frequency ($\bar{\omega}_{ho}$) and the corresponding oscillator length (a_{ho}) of our trap are

$$\bar{\omega}_{ho} \approx 2\pi \times 131\text{Hz} \tag{3.10a}$$

$$a_{ho} = \frac{\hbar}{m\bar{\omega}_{ho}} \approx 0.94\mu\text{m} \tag{3.10b}$$

These parameters allow us to estimate the condensation temperature T_c of our system, the chemical potential μ and the Thomas-Fermi radius R_{TF}:

$$T_c = \frac{0.94\hbar\omega_{ho}N^{1/3}}{k_B} = 256\text{nK} \tag{3.10c}$$

$$\mu = \frac{\hbar\omega_{ho}}{2}\left(\frac{15Na}{a_{ho}}\right)^{2/5} = 98.5\text{nK} \tag{3.10d}$$

$$R_{TF} = a_{ho}\left(\frac{15Na}{a_{ho}}\right)^{1/5} = 5.8\mu\text{m} \tag{3.10e}$$

where a is the scattering length of ^{87}Rb.

3.3.3 Lifetime

Another important quantity to characterize the performance of the BEC is the lifetime. A typical lifetime measurement is presented below. We prepare the BEC and then we hold it at the final trap depth of the evaporation for a variable amount of time. We then release it and measure the number of atoms. The results are fitted to a double exponential decay curve $N_a = N_T(\exp[-t/\tau_1] + \exp[-t/\tau_2])$. In figure 3.10 it is shown a typical lifetime measurement in our system. The high densities of the BEC sample make the system to suffer from three-body losses, which are reflected in the τ_1 contribution to the exponential. After that short period of time, the loss mechanism is mainly due to collisions with the background gas particles, that limit the lifetime of our condensate in the long term, and is given by τ_2. The lifetime of our condensate $\simeq$ 10s, within the usual range of BEC experiments.

	Fit parameter	Error
N_T	61.3 $\times 10^3$	$\pm$2.1
τ_1	0.31 s	$\pm$0.1
τ_2	9.43 s	$\pm$0.5

Table 3.2: Result of the fitting in figure 3.10.

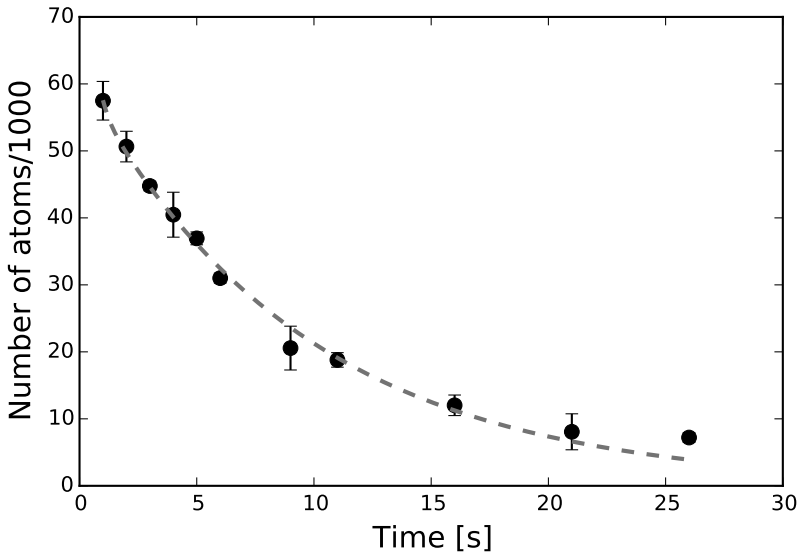

Figure 3.10: The figure shows an example of a typical lifetime measurement in our system. The results of the double exponential fit to the data is presented in the table below. The error bars on the graph are standard deviations of three measurements.

CHAPTER 4

ENDOSCOPIC IMAGING THROUGH A FIBER BUNDLE

Up to now, I have presented the basic theory concerning spin-1 systems and the efforts towards a working experiment to produce spin-1 Bose-Einstein condensates. The last chapter was dedicated to the characterization of the BEC samples. In this chapter, I will present the first results obtained with the setup that we built. This chapter is a re-formatted version of the article published in [22]. All the data acquisition and the data analysis have been carried out by me.

This chapter is a result of the initial plan to explore the spin-1 physics of a ^{87}Rb BEC in the ultra-low magnetic field regime, and the need to transport reliable images of the physical system outside a shielded environment. Within this spirit, we started to investigate how the properties of absorption imaging pictures are affected when they are transmitted through a coherent fiber bundle. These devices are widely used for optical diagnosis in medicine, and for fluorescence imaging in biology, but they have not been used in quantum gas experiments. Here,we use a coherent fiber bundle to demonstrate the endoscopic absorption imaging of quantum gases. We show that the fiber bundle introduces spurious noise in the picture mainly due to the strong core-to-core coupling. By direct comparison with free-space pictures, we observe that there is a maximum column density that can be reliably measured using our fiber bundle, and we derive a simple criterion to estimate it. We demonstrate that taking care of not exceeding such maximum, we can retrieve exact quantitative information about the atomic system, making this technique appealing for systems requiring isolation form the environment.

4.1 Introduction

Cold atoms systems are at the core of the emerging quantum technologies and represent an invaluable resource for the exploration of quantum phenomena. On the one hand they enable the development of increasingly precise sensors and measurement devices, on the other hand they can be manipulated

with great control, allowing the engineering of complex hamiltonians for quantum simulation. Often, to achieve such exquisite level of control and precision, cold atoms systems need to be isolated from the environment. Magnetically sensitive experiments, such as atom magnetometers [89, 90], atom clocks [91], atom interferometers [92] and quantum simulators [93], need to be accurately shielded from external magnetic fields using one or more layers of μ-metal. Experiments that require cryogenic temperatures [94, 95] need instead to be performed inside cryostats. Thermal isolation is also desirable to increase the performance of atomic clocks [96].

Within the experiments aiming at realizing quantum simulations, there are those that require extreme isolation from the environment to explore the effects of dipolar interactions in quantum gases [97, 98]. Unless one employs atomic species with permanent magnetic dipole moment like Dy [99] or Er [100], to investigate such effects it is necessary to ensure that the interaction energy of the atomic dipole moments is not washed out by the Zeeman coupling to any residual magnetic fields. For example, since in ^{87}Rb the dipole-dipole energy is only $\simeq h \times 1$Hz, with h the Planck constant, and the Zeeman splitting goes approximately as $\simeq h \times 7 \times 10^9$ Hz/T, it follows that the external magnetic field should be below 10^{-9}T for dipolar effects to become relevant. Our experiment has been built to explore such extreme regime and has been designed to be completely non magnetic and to accommodate 5 layers of μ-metal magnetic shield, in combination with active field compensations.

In our experiment, as in all those that require a strong shielding, retrieving information from the system inevitably leads to an unwanted coupling with the environment. Particularly disruptive is the use of the widely employed absorption imaging, since it requires high numerical aperture optics and sophisticated CCD cameras. These latter are not compatible with a shielded environment so they need to be accommodated outside the shield. Then, to allow the image of the atoms to reach the camera, one or more holes must be cut in the shield resulting in a detrimental loss of shielding factor [101].

In this work, we follow a different approach and we demonstrate the use of a fibre bundle to perform endoscopic absorption imaging of quantum degenerate gases. Fibre bundles are fibre optic devices composed of thousands of standard optical fibres which are packed together. They are widely used in biological applications for fluorescence imaging techniques [102–104] and in medical endoscopy for optical coherence tomography and multiphoton microscopy [105–108]. If the spatial ordering of the fibres is preserved on both ends, the bundle is regarded as coherent and can be used to transfer an image from one end to the other. Fibre bundles have a diameter of only a few mm and are flexible, making them ideal candidates to transport the absorption images through small holes in the shield, therefore causing only minor disruption in the shielding. By accounting for the spurious effects introduced by the fibre bundle, we show that quantitative information can be retrieved from the absorption pictures, making our

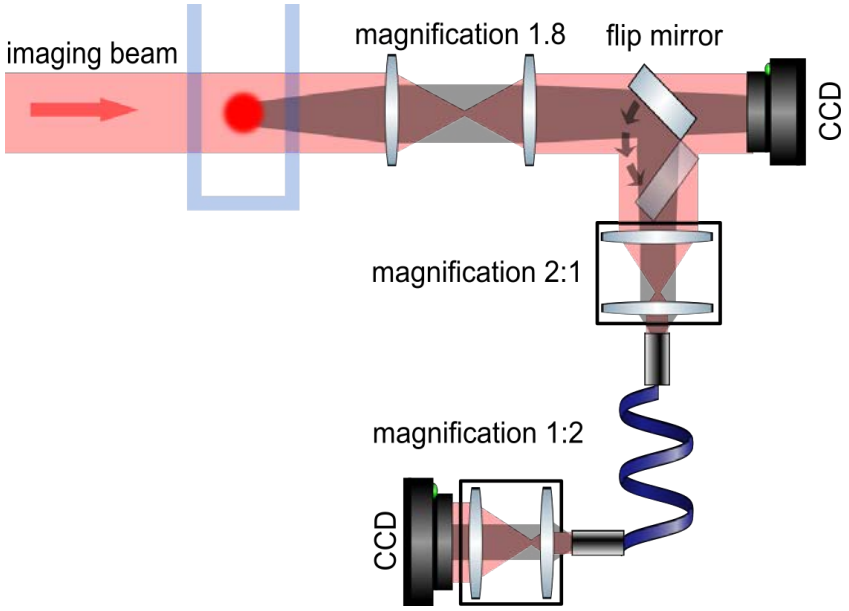

Figure 4.1: Schematics (not in scale) of the optical setup used. The atomic cloud casts a shadow on the imaging beam that is magnified by a factor of 1.8 by a first telescope. A flipping mirror send the image of the shadow of the atomic cloud either on the CCD or on the fiber bundle setup. In this latter a 2:1 telescope images the focal plane on the input facet of the fiber bundle. A 1:2 telescope then images the output facet on the CCD camera.

technique extremely appealing for experiments requiring high shielding factors.

4.2 Endoscopic absorption imaging

As shown in Fig. 4.1, to perform the endoscopic imaging of our ultracold sample, instead of sending the light directly to the CCD camera, we send it to a leached fiber bundle. This latter is a commercially available fiber bundle (Schott 1249311 RLIB CVET,1.00 X 670,8.2M,13.5K,QA 0.80) that is 67 cm long and contains a total of 13500 fibers with 8.2 μm core diameter. The fibers are coherently packed in an hexagonal pattern so that the input/output facet at each end has 1 mm outer diameter. After magnification, the focal plane of the atoms is imaged on the input facet of the bundle with a 2:1 telescope made of two achromatic lenses (Thorlabs MAP1050100-B). A similar optical set up with a 1:2 magnification is used to image the output facet of the fiber bundle onto the CCD chip. It is formed by two lenses: a high NA (0.5) f = 8 mm aspheric lens (Thorlabs AC240TME-B) and a f = 16 mm lens (Thorlabs AC080-16-B). It is mounted on a cage system to allow for precision alignment. This allows us to properly collect the light coming out the bundle since the typical NA of the fibers is $\approx$ 0.35. With this setup, the overall magnification for the fiber bundle optical system is also 1.8. To characterize the absorption imaging through the bundle, we use a simple flipping mirror that allows to switch between the two imaging paths and therefore to have the direct comparison of the pictures transmitted through the bundle with the

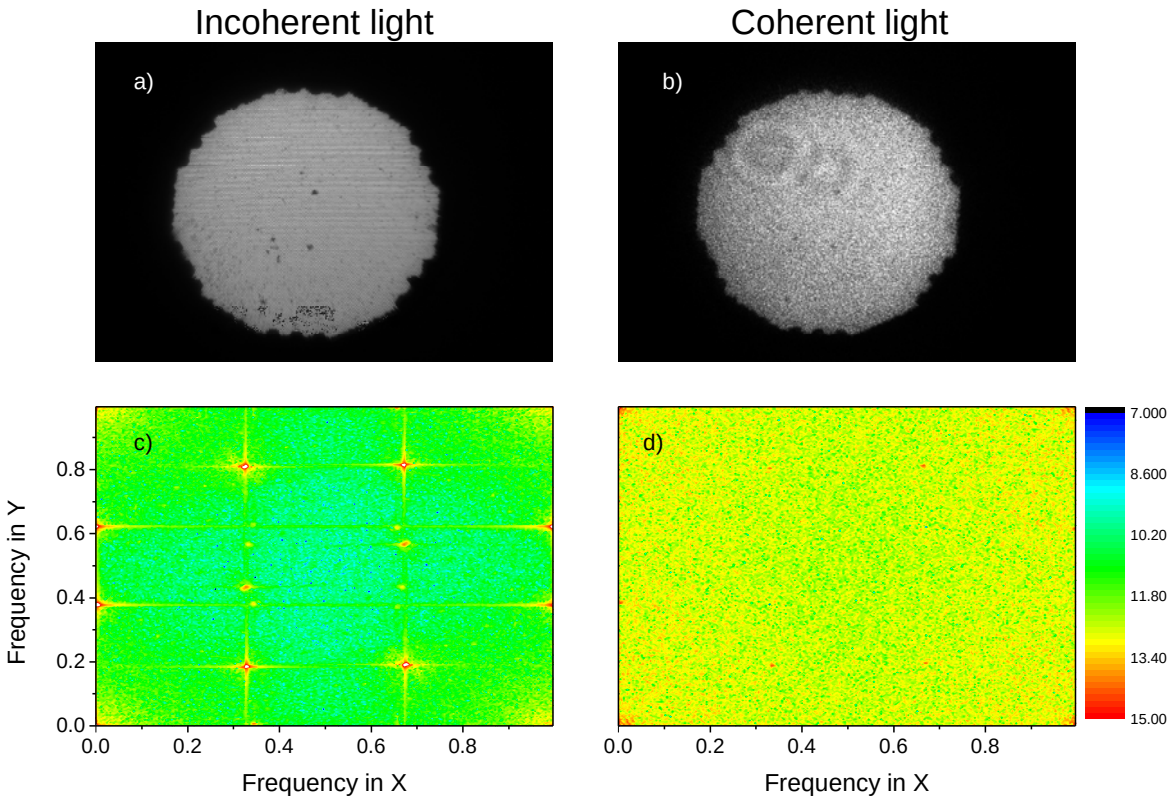

Figure 4.2: Image of the output facet of the fiber bundle when injected with incoherent (a) and coherent light (b). c) and d) are the corresponding two-dimensional Fourier transforms. The color scale is in dB. While in a) it is possible to appreciate the hexagonal packing of the fiber bundle, in b) only a speckle pattern is visible. Equivalently, in c) clear peaks emerge from the spectrum while in d) no peaks are visible.

pictures taken in free space.

By passing through the fiber bundle, pictures can suffer from spurious effects such as multimodal coupling [109], cross talk between the fiber cores [110] and pixelation due to the packing structure of the bundle that can potentially alter the information transmitted. All this, in addition to a non-unitary quality area, also severely limit the transmission efficiency [111].

To limit pixelation and have a better image quality we have chosen a bundle with a large number of small core fibers closely packed. The price to pay is a non-negligible core-to-core coupling. We have found that the cross talking between fibers must be accounted especially when working with coherent laser light. In Fig. 4.2(a) and (b) we report an image of the output facet of the bundle when it is injected with incoherent and coherent light respectively. In the case of incoherent light, the underlying matrix of fibers is clearly visible. This becomes even more clear when performing the 2D Fourier transform of the image, see Fig. 4.2(c), where the regular structure of the fibre packing give rise to clear peaks in the power spectrum. When instead we use coherent light, a speckle pattern appears and the regular lattice of fibres is completely washed out. This is due to the fact that the laser light acquires a different phase inside

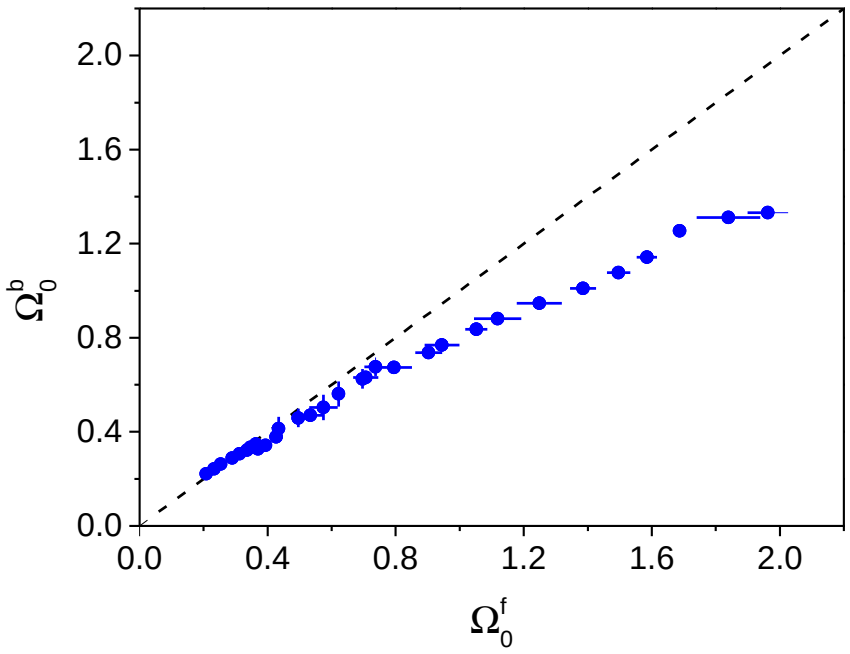

Figure 4.3: Peak column density measured using the fiber bundle Ω_0^b as a function of the peak column density measured in free space Ω_0^f for the same atomic sample. The dashed line is the curve $\Omega_0^b = \Omega_0^f$. The errorbars are one standard deviation statistical errors.

each different fiber. The cross-talking between different fibers inside the bundle creates the interference that generates the speckle pattern. By performing the 2D Fourier transform we confirm the absence of the peaks on the power spectrum, see Fig. 4.2 (d) and we observe that the noise level is significantly increased. The appearance of a noisy speckle pattern is not *per se* a problem for the absorption imaging since it is stationary and it is eliminated when computing Ω. However we will see in the following that the percolation of light into adjacent fibers severely affects images of objects with high optical density.

In principle, another major effect to take into account is the low transmission efficiency of the bundle, which acts as an optical attenuator. We have measured the efficiency of our fiber bundle to be $\eta \simeq 0.33\%$ at 780nm, which is compatible with the typical values quoted by the manufacturer and in other studies [111]. However it is easy to verify that absorption imaging is robust against this effect. Indeed, in the absence of other spurious effects, even in case of very poor efficiency the column density obtained using the fiber bundle is identical to the one in free space: $\Omega^b = -ln[(I_1^b - I_3^b)/(I_2^b - I_3^b)] = -ln[\eta(I_1^f - I_3^f)/(\eta(I_2^f - I_3^f))] = \Omega^f$, where the superscripts b and f stand for bundle and free-space respectively.

To measure the effect of the cross-talk and of the transmission efficiency we take absorption pictures of our atomic clouds at different temperatures and number of atoms. For each set of parameters we vary the intensity of the probe beam from $\simeq 0.05$ to $0.7\ I_0/I_s$. To make a direct comparison, we take the absorption picture of the cloud with the same parameters, both using the fiber bundle and in free space. We then fit each absorption image $\Omega(x, y)$ using a 2d Gaussian function and extract the peak column

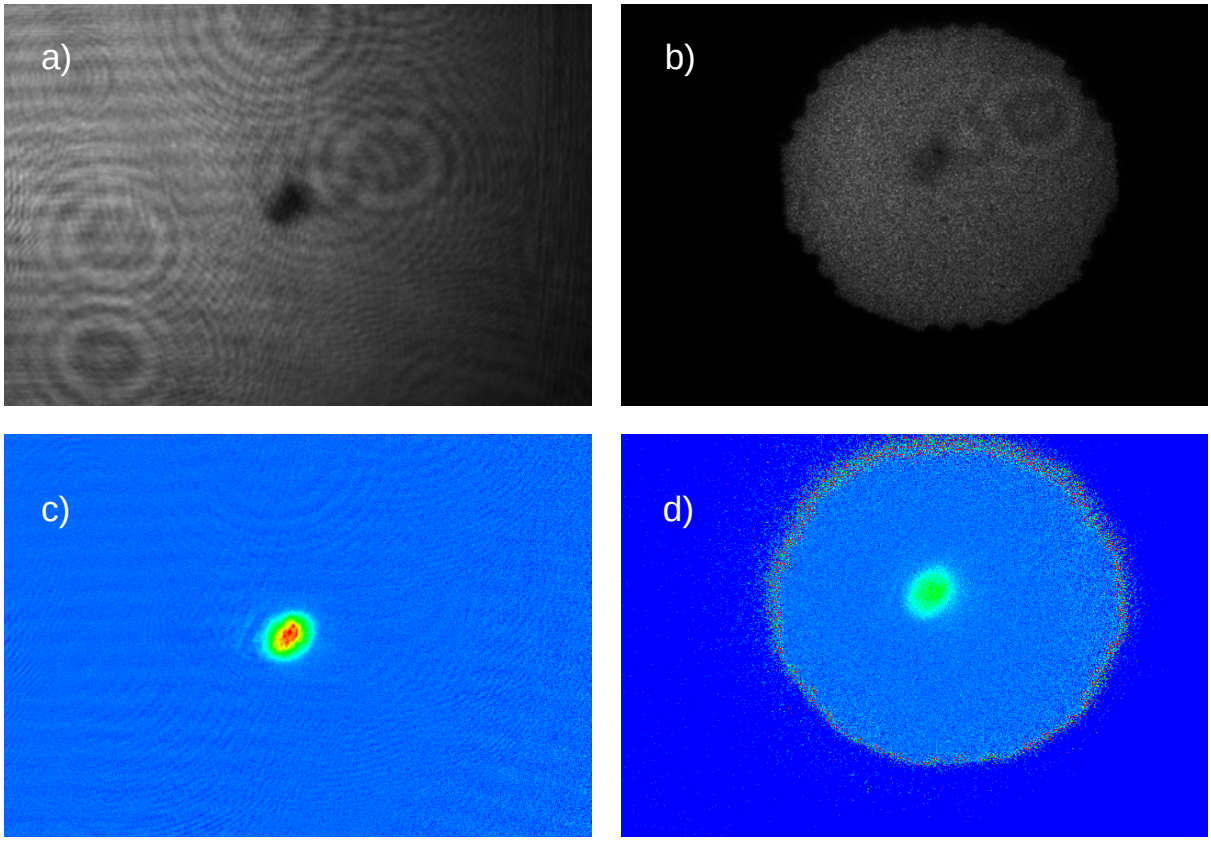

Figure 4.4: a) and b) Direct picture of the absorption profile of a Bose-Einstein condensate in free space (I_1^f) and through the fiber bundle (I_1^b) respectively. c) and d) the corresponding absorption pictures Ω^f and Ω^b. The colour scale is the same in c) and d). Each picture is 656×492 pixels.

density Ω_0, that is directly proportional to the number of atoms in the cloud $N = 2\pi\Omega_0\sigma_x\sigma_y/\sigma_0$, where $\sigma_{x,y}$ are the widths of the Gaussian distribution and σ_0 is the resonant scattering cross section. We have verified that, within our errorbars, $\sigma_{x,y}$ measured through the fiber bundle are identical to those measured in free space, as expected since the overall magnification of the two imaging system is equal.

In Fig. 4.3 we summarize our results reporting Ω_0^b as a function of Ω_0^f. We observe that, within our errorbars, $\Omega^b \equiv \Omega^f$ for values below $\Omega_M \simeq 0.7$. We conclude therefore that for small column densities the impact of the fiber bundle in the images has a negligible effect. For values of Ω above 0.7 however, the peak column density measured with the bundle starts to be lower than the one measured in free space, and the difference increases as Ω^f increases. Note that we have taken care that no saturation effects were present in the free-space picture and consequently in the pictures taken through the bundle. Indeed this latter transports the light only after it has interacted with the atoms, so it does not play any role in the atom-light interaction. The reason for the discrepancy at higher Ω can be understood from Fig. 4.4(a) and (b), where we report I_1^f and I_1^b for a dense BEC. In particular, in Fig. 4.4 (b) it is possible to observe that even in case of a very dense sample, the atomic shadow is not completely dark, as it is in free space

-Fig. 4.4 (a). As described above, when passing through the bundle the image acquires a faint speckle pattern created by the core-to-core coupling. This percolates into the fibers that transport the shadow of the atoms preventing this latter to be completely dark on the output facet. This effect is therefore more important in the pictures with high column density samples. The resulting effect can be observed in the absorption pictures in Fig, 4.4(c) and (d) (same colour scale), where the column density measured with the bundle is significantly lower than the one measured in free space.

Whenever it is possible to make a direct comparison, like in our case, it is easy to correct for the effect of the cross-talking by doing a simple calibration. For example, one can fit the curve $\Omega \equiv \Omega^f = \Omega^b(\Omega^f)$. However problems arise when this direct comparison cannot be done, as it will be the case once our setup will be enclosed in the five-layer μ-metal shield. In that case the only information available will come from the pictures taken through the bundle.

A quantitative description of the core-to-core coupling is a challenging task, especially for thousands of fibres and this goes beyond the scope of this work. Here instead we derive a simple criterion to ascertain the maximum reliable column density Ω_M that can be measured with the fiber bundle, using *only* the information available through the fiber bundle itself. For very dense samples, that in normal conditions would feature a high column density, it is possible to remain below Ω_M and therefore to obtain correct quantitative information either using a probe beam well above the saturation intensity or increasing the detuning of the probe light Δ. If on the one hand remaining below Ω_M guarantees to extract correct information, on the other it inevitably penalizes the signal-to-noise ratio. We will see in the following that, at least for the parameters of interest for our experiment, the increase in the signal-to-noise ratio is negligible.

Our method requires to prepare samples with different densities in order to span a wide range of column densities. In this work the three samples are A=(1.8×10^5, 250 nK); B=(1.2×10^5, 100 nK) and C=(1×10^5, 20 nK), where the first number indicates the number of atoms and the second the temperature of the cloud. Samples A and B are dilute thermal clouds while sample C is a BEC, and they are prepared changing the final point of the evaporation ramp. For each sample we perform the absorption imaging with different intensities of the probe I_0 (in alternative one can scan the detuning Δ). We then perform a Gaussian fit of the shadow cast by the atoms in $I_1^b(x,y)$, retrieving the value of the background light b and the amplitude of the Gaussian s [1]. We verify that the value of b coincides with the one obtained from $I_2^b(x,y)$. In the region of maximum absorption the number of counts in the CCD drops from b to $m = b - s$, and it is easy to verify that $\Omega_0 \simeq -ln(m/b)$. In the absence of spurious effects and for $I_0 < I_s$, we expect both s and b to increase linearly with the probe intensity I_0 and therefore that m is a linear

[1] The correct fitting function for a BEC is a Thomas-Fermi profile. We have verified that within our errorbars, using a Gaussian profile does not introduce any appreciable systematic error in the determination of the parameters here discussed.

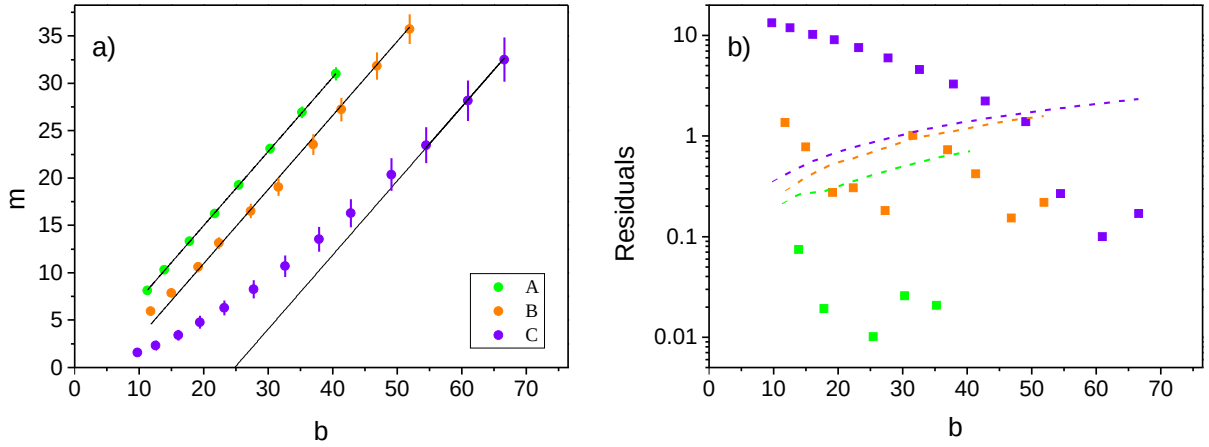

Figure 4.5: a) Number of counts in the region of maximum absorption m as a function of the average number of counts in the background b, evaluated from the direct picture I_1^b. All the units are counts per pixel. The three data sets are described in the text. The solid lines are linear fits to the data using the procedure described in the text. The errorbars are one standard deviation statistical errors. b) Absolute value of the residuals of the linear fits reported in a) as a function of b. The dashed lines correspond to the errorbars in a).

function of b. As reported in Fig. 4.5(a), this is the case for the low density sample A. From a linear fit to the data set of the sample A, we obtain the slope m/b that should be common to all data sets not significantly affected by the core-to-core coupling. We then fit the data sets corresponding to samples B and C using a linear function keeping the offset as the only free parameter, as shown in Fig. 4.5(a). As a criterion to estimate Ω_M, we discard all the points whose absolute value of the residuals is larger than the errorbars, corresponding to the points above the dashed lines in Fig. 4.5(b). Using this simple method that relies only on the information acquired through the bundle, we find that $\Omega_M \simeq 0.7$, in agreement with what we have observed from the direct comparison with the free space pictures.

To give a specific example we have measured the BEC transition using both imaging systems, taking care not to exceed Ω_M while using the fiber bundle. To this end we have measured the fraction of condensed atoms N_0 as a function of the temperature. This is done fitting $\Omega(x, y)$ with a two-dimensional bimodal distribution made by the sum of a Thomas-Fermi and a Gaussian profile. As can be seen from Fig. 4.6, the results obtained using the fibre bundle are in very good agreement with those taken in free space. For both imaging systems, we are not able to detect any thermal component for condensed fractions above $\simeq 60\%$. From the (integrated) density profiles reported in Fig. 4.6, it is possible to appreciate the modest increase in the signal-to-noise ratio using the fiber bundle, that does not significantly affect our measurements. For example, in the leftmost panel of the upper row of Fig. 4.6, the signal-to-noise ratio drops from 168 (free-space) to 104 (fiber bundle). More quantitatively, we compare the critical temperatures T_c measured with the two methods. In three dimensions, the condensate fraction scales as $N_0/N = 1 - (T/T_c)^3$, with $k_B T_c = 0.94\hbar\bar{\omega}N^{1/3}$, where $\bar{\omega}$ is the average trapping frequency

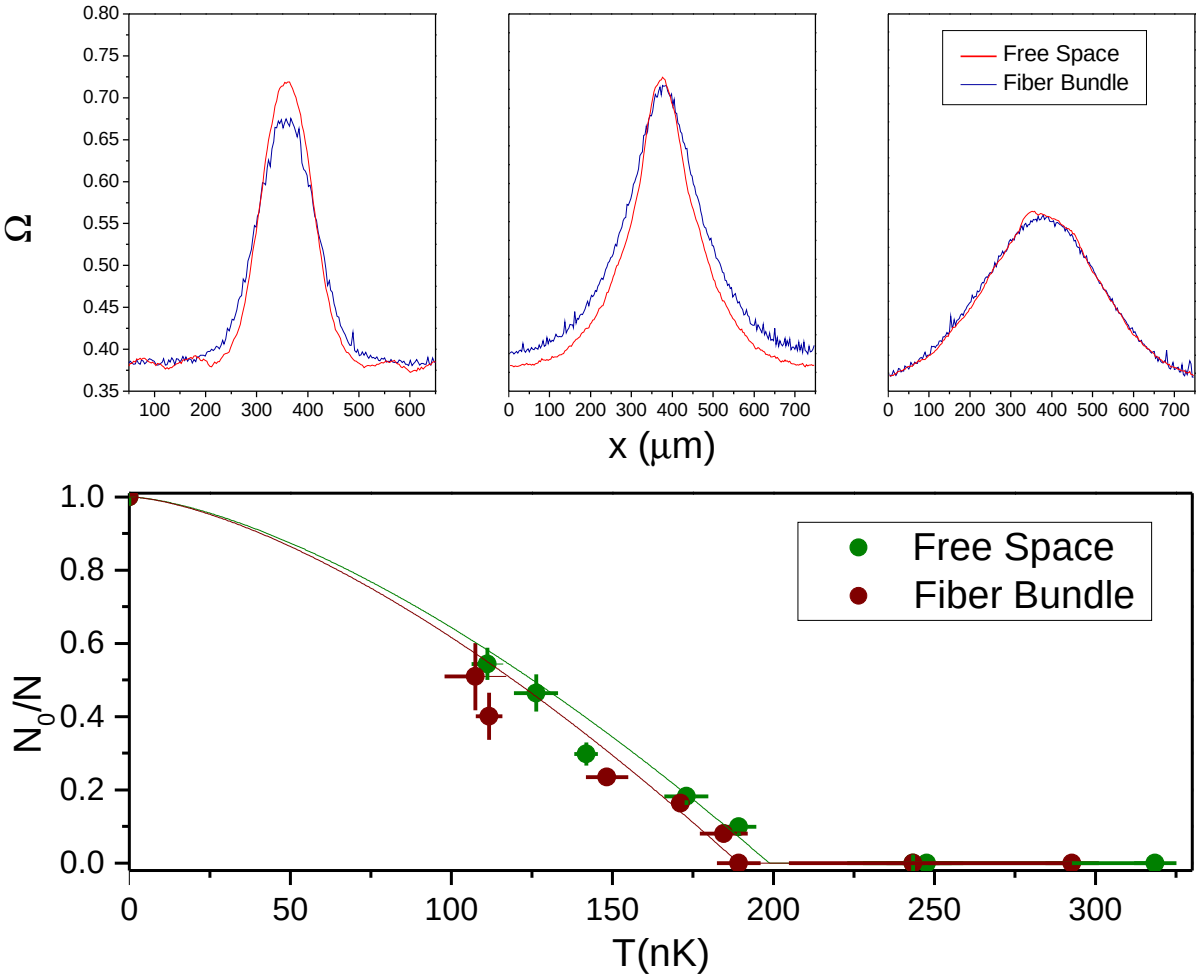

Figure 4.6: The Bose-Einstein condensate transition. Upper row: integrated density profiles of our atomic sample across the BEC transition measured using the fiber bundle and in free space. From the right to the left: a thermal cloud, a partially condensed cloud and a pure BEC. Lower row: condensate fraction as a function of the temperature. The lines are the fit functions explained in the text.

and k_B the Boltzmann constant [69]. In an optical dipole trap, the evaporation has two effects: it lowers the temperature of the cloud and reduces the trapping frequencies. Indeed, if U is the depth of the trap (proportional to the trapping laser intensity), we have that $k_B T \simeq \xi U$, with $\xi \simeq 1/6$, and $\bar{\omega} = U^{1/2}[(4/mw_0^2)(2/mz_R^2)^{1/2}]^{1/3}$, being m the mass of the atom and w_0 and z_R the waist and the Rayleigh length of the trapping beam [112]. From this, it follows that for our trap the condensate fraction scales as $N_0/N = 1 - (T/\tilde{T}_c)^{3/2}$, with $\tilde{T}_c = 1.88\hbar^2 N^{2/3}/[k_B \xi m(w_0^2 z_R)^{2/3}]$. By fitting the two curves shown in Fig. 4.6 we obtain that $\tilde{T}_c^{\,b} = 189 \pm 7$ nK and $\tilde{T}_c^{\,f} = 198 \pm 7$ nK, whose difference is within our statistical uncertainty, demonstrating the reliability of absorption imaging through the fiber bundle.

CHAPTER 5

THERMALIZATION PROPERTIES OF A SPIN-1 FERROMAGNETIC CONDENSATE

Trapping the atoms in an all-optical dipole trap allows us to prepare Bose-Einstein condensates in which the different hyperfine states of the F-manifold are macroscopically populated. The presence of multiple Zeeman substates that are condensed together adds a degree of freedom to the dynamics of the system (see section 1.2). This makes spinor condensates a versatile system to study a wide range of problems, from quantum magnetism to spin squeezing including non-equilibrium physics and coreless vortices [47–50, 60].

Spin-1 condensates are ferromagnetic(antiferromagnetic) if the difference between the scattering lengths of the different collisional channels c_2, is negative(positive). The ferromagnetic character of ^{87}Rb was predicted theoretically [65], and experimentally confirmed since the first experimental realizations of ^{87}Rb spinor gases [46, 66, 113].

In this chapter I will report on our experimental investigation of the thermalization properties of spin-1 ferromagnetic condensates in a non-zero magnetic field. We have focused on two main subjects. In section 5.1 we investigate the long term thermalization dynamics of the system magnetization. In section 5.2 we report on the long term equilibrium state of a spin-1 ferromagnetic condensate as a function of both initial magnetization and external magnetic field.

5.1 Magnetization dynamics

The ground state properties of a spin-1 system in an external non-zero magnetic field are determined by the competition between two energy scales: a) the interspecies interaction energy given by $c_2 n$ where n is the density and c_2 characterizes the spin-mixing collisions. For our experimental parameters, this energy is $|c_2|n \simeq 10 \times h$ Hz; b) the quadratic zeeman effect induced by the external field parametrized by

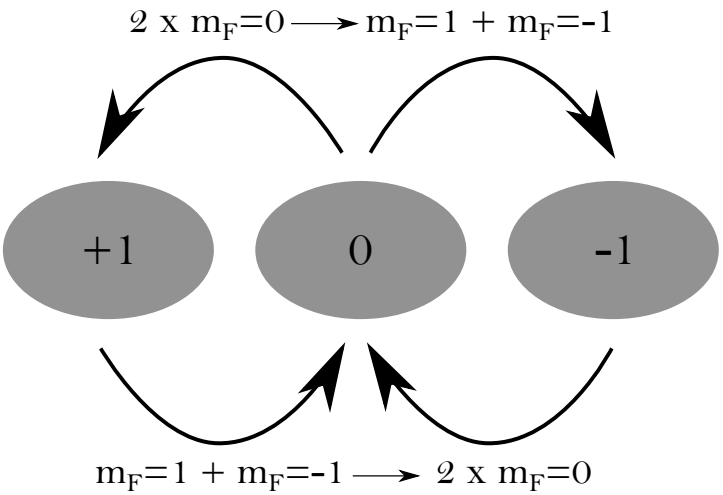

Figure 5.1: Pictorial representation of spin-mixing dynamics. The arrows show the direction of the population transfer.

$q = \frac{E_{+1}+E_{-1}-2E_0}{2} \simeq h \times 70 \times B^2$ Hz/G^2, where E_i are the energies of each Zeeman sublevel (see equation 1.7c). As mentioned before in section 1.2, due to the conservation of the magnetization, spin-mixing collisions $|F=1, m_F=-1\rangle + |F=1, m_F=+1\rangle \leftrightarrow |F=1, m_F=0\rangle$ as depictedn in figure 5.1, become a relevant process in the dynamics of such systems. Indeed, the relaxation towards the ground state can only happen via spin-mixing collisions because they conserve the total angular momentum of the system. However, to reach the ground state the system has to overcome two main issues then. On the one hand, the spin-mixing dynamics is suppressed for magnetic fields that induce a quadratic zeeman shift larger than the energy associated with the spin-mixing coupling $|q| > 2|c_2|n$, as reported in [114, 115]. On the other hand, the magnetization can vary during the experimental window due to dissipative processes. The question arises, does the magnetization of experimentally accesible states reach an equilibrium within the experimental window?

In what follows, I will report on the investigation of these effects in our experimental setup, showing the boundaries under which the system can effectively relax to an equilibrium state, therefore setting some boundaries for the study of equilibrium physics in this system.

5.1.1 Zero Magnetization

The case of $M = \rho_{+1} - \rho_{-1} = 0$ is somewhat special, since any population distribution with $\rho_{-1} = \rho_{+1}$ corresponds to zero magnetization, with $\rho_{m_F} = \frac{N_{m_F}}{N_t}$ as the fractional populations of each Zeeman state, whit $m_F = \{-1, 0, +1\}$. All these states can be accessed experimentally by preparing the initial sam-

ple in the $m_F = 0$ state and applying a radio-frequency pulse afterwards. The experimental sequence is the same as explained in section 3.2. The only difference is that during the last two stages of the evaporation, we switch on the quadrupole field produced by the MOT coils. This induces a loss channel for the magnetically sensitive states. We end up with a pure condensate of $N \simeq 8 \times 10^4$ atoms in the $m_F = 0$ state. After that, we apply a variable length rf pulse to select the initial state populations of the form $((1-\rho_0)/2, \rho_0, (1-\rho_0)/2)$. After the initial state preparation, we adiabatically ramp the external magnetic field to the desired value. This external field is produeced by the compensation coils in the vertical direction. We control the field by varying the voltage (V_{set}) applied to the current source. The coils produce a magnetic field of $B_z = (3.83/0.5 \times V_{set} - 1.5)$G at the center of the cell. The end of the magnetic field ramp sets the starting point t_0 of our experimental window. We then wait for a variable time t for the system to evolve, and probe the clouds using the Stern-Gerlach technique.

In figure 5.2 I have plotted the temporal evolution of the fractional populations of each Zeeman state for different initial populations $\rho_0 \in (0.39, 0.16, 0.07)$, and for two different values of the applied field: $B \simeq 38$mG ($q \simeq 0.1 \times h$ Hz) and $B \simeq 422$mG ($q \simeq 12 \times h$ Hz). Each point corresponds to 3 experimental runs, and the error bars are the corresponding standard deviations. We can observe that the amplitude of the spin oscillations is bigger for smaller fields. The period of the oscillations, on the other hand, has a resonant value at a finite value of the magnetic field around $\simeq 100$mG [46, 114], and it also depends on the initial value of ρ_0. The lifetime in our system, however, exceeds the observation times of previous studies [36, 46], as we have observed spin dynamics up to 7s. This gives us an excellent opportunity to explore the long-term equilibration properties of the system. After 7s the number of atoms in our system becomes too low to be detected. However, already after ≈5s, the oscillations of the populations are already damped and close to their equilibrium values for most of the accessed points on the $\rho_0 - B$ parameter space.

In figure 5.3 it is shown the difference between the final and initial population of the $m_F = 0$ state as a function of the the initial population and the applied magnetic field for two different evolution times $t = 3s, 5s$. We can clearly appreciate two things. First, that the spin dynamics is strongly suppressed for initial fractions $\rho_0 > 0.6$. Second, it does not strongly depend on the magnetic field within our parameter region $B \in (0, 0.08)$G.

We can observe a similar behaviour in both plots for different evolution times. The main differences are observed for very low initial populations of the ρ_0 state ($\rho_0 < 0.2$) and for small magnetic fields ($0 < B < 500$mG). In that region, we can observe spin dynamics that does not equilibrate within our experimentally accessible evolution times. For bigger fields and bigger initial ρ_0 fractions, the system

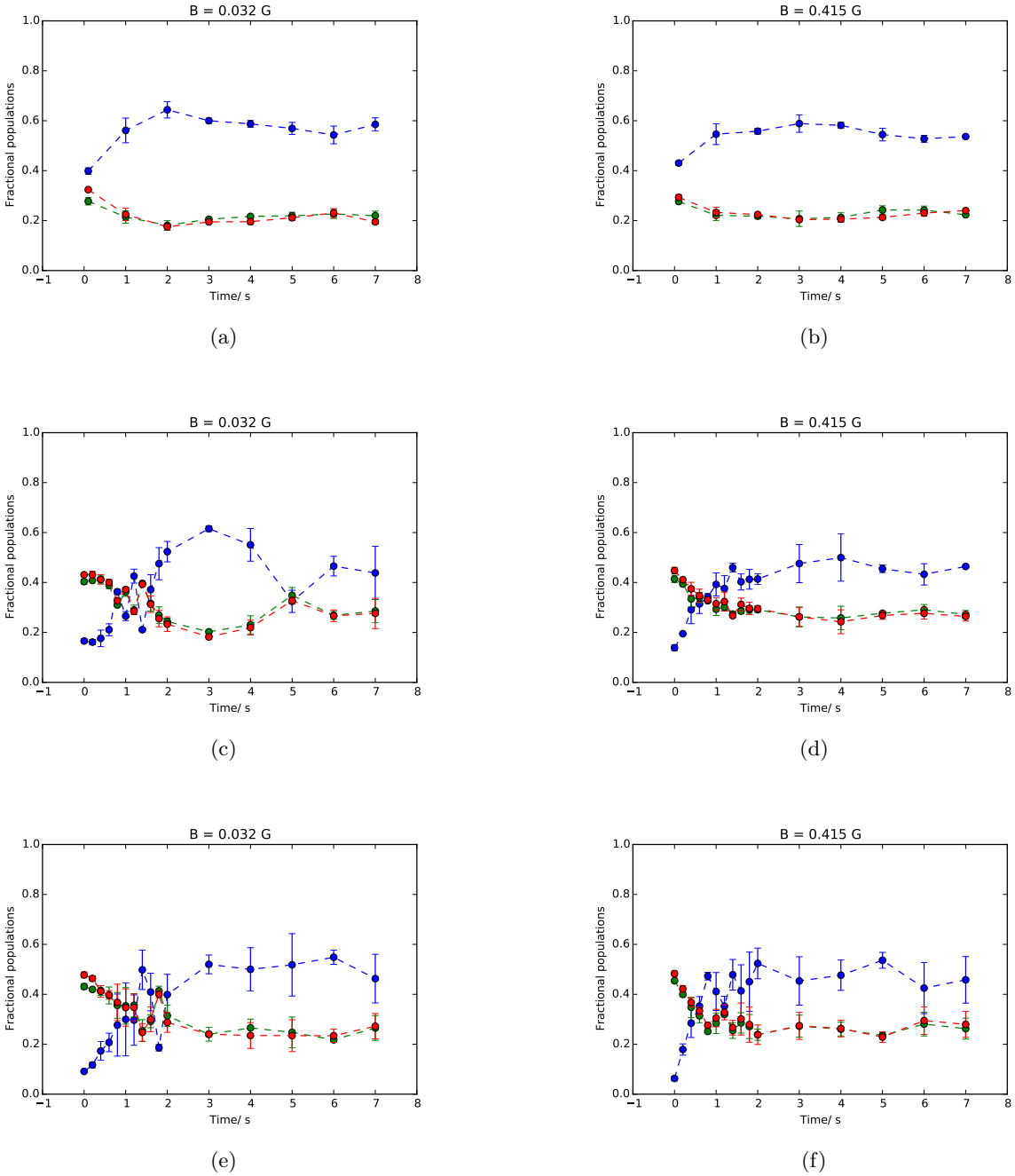

Figure 5.2: Temporal evolution of ρ_0 at different magnetic fields and initial population fractions. The solid points correspond to the average of three expreimental runs of the experiment. The error bars are the standard deviation, and the dashed lines are displayed as a guide to the eye. The blue, green and red points correspond to the ρ_0, ρ_{+1} and ρ_{-1} respectively.

clearly reaches an equilibrium state within 5s. For all these cases, the total magnetization has been measured to be $M = 0.0 \pm 0.02$.

Remarks To conclude, we can say that the magnetization is conserved for all cases studied here. We have also framed the region for which the spin-dynamics equilibrate within our experimentally accessible evolution time. We observed a small region for which the oscillations of the population do not reach an equilibrium within 5s of evolution.

We have to note that inhomogeneous spin textures are observed in our system (see figure 5.4). Some of the dynamical properties of this spin-structure formation and evolution has been studied in [37]. They observed that the evolution dynamics of this structures is longer than the experimental time for large values of $|q|$. How the formation and dynamics of such spin textures affects our measurements is unclear. But taking everything into account we cannot talk about accessing the ground state of a ferromagnetic spin-1 BEC because we have seen that there are equilibration processes that last longer than our experimentally accessible times.

It is worth noticing that in our experiment the BEC has a substantially higher number of atoms with respect to previous experiments. Due to this, the spin-mixing dynamics is highly suppressed especially in the $2 \times |F = 0\rangle \rightarrow |F = -1\rangle + |F = +1\rangle$ channel. Indeed, this can be explained considering that the high density of our samples leads to mean field energies on the order of $\frac{4\pi a\hbar^2}{m} n \simeq h \times 3\text{KHz}$, almost three orders of magnitude bigger than the energy associated to the spin-mixing dynamics. This effect is analogous to the self-trapping effect observed in double-well systems[].

5.1.2 Finite magnetization

We have seen that for the case of $M = 0$, the magnetization does not change despite the fact that the system presents spin dynamics up to 7s. The $M \neq 0$ are studied separately. We investigate the final magnetization M state of the system as a function of the initial magnetizatio (i.e the magnetization set at $t = 0$) and of the magnetic field B, $B \in (0, 0.8)G$ and for initially set magnetizations $M \in (0, 1)$.

To prepare the initial magnetization state, we apply a magnetic field gradient during the last 3s of the evaporation. The magnetic field gradient increases the trap depth for the $m_F = +1$ atoms, while it lowers the trap depth for the $m_F = -1$. Therefore, the thermalization process is enhanced for the $m_F = +1$ atoms, and the other two species are selectively evaporated before. By varying the magnetic field gradient applied we can reach different initial states. The fully magnetized sample is achieved by applying a magnetic field gradient of $\simeq 0.25$G/cm. The gradient coil, placed in the vertical direction, is physically mounted on top of the quadrupole coils for the 3D MOT to ensure optimal alignment. The coil

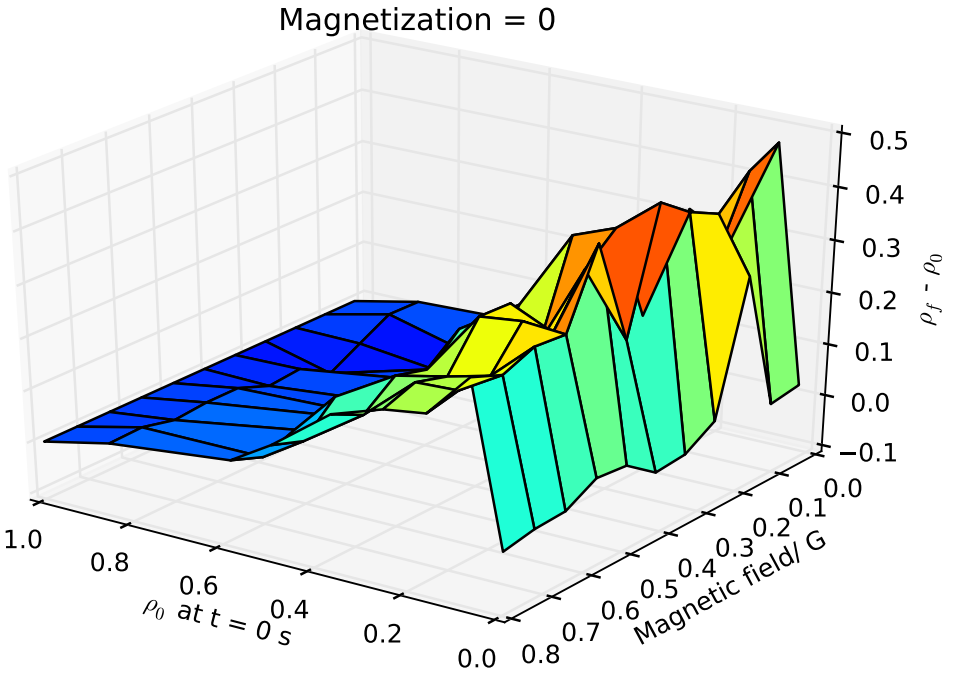

(a)

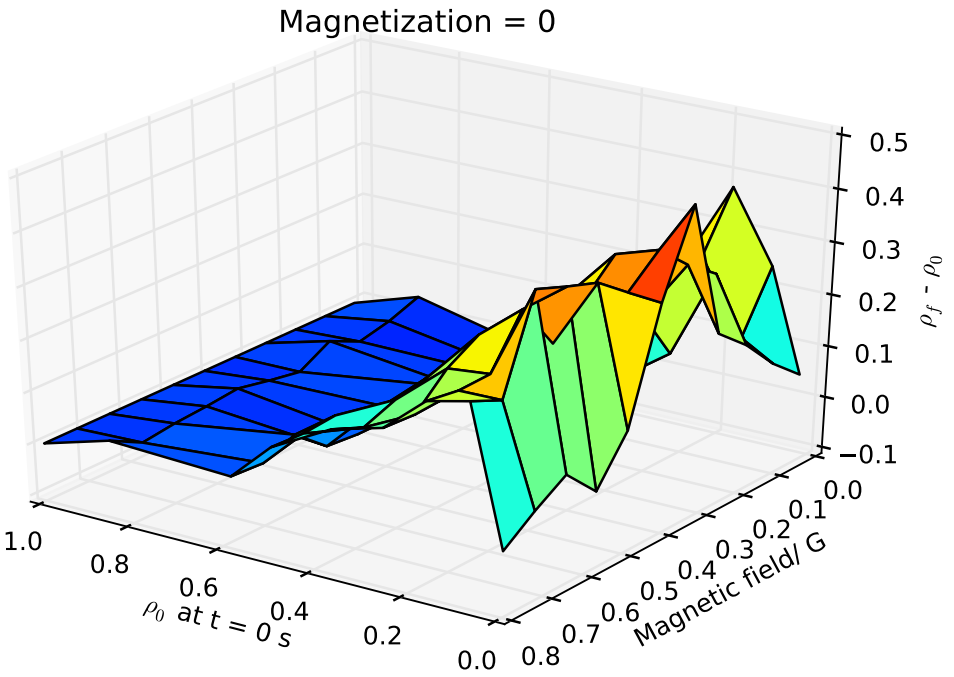

(b)

Figure 5.3: In the figures it is displayed the difference between the final and initial ρ_0 as a function of the initial fraction set using radio frequency pulses and the applied magnetic field for holding times of 3s and 5s.

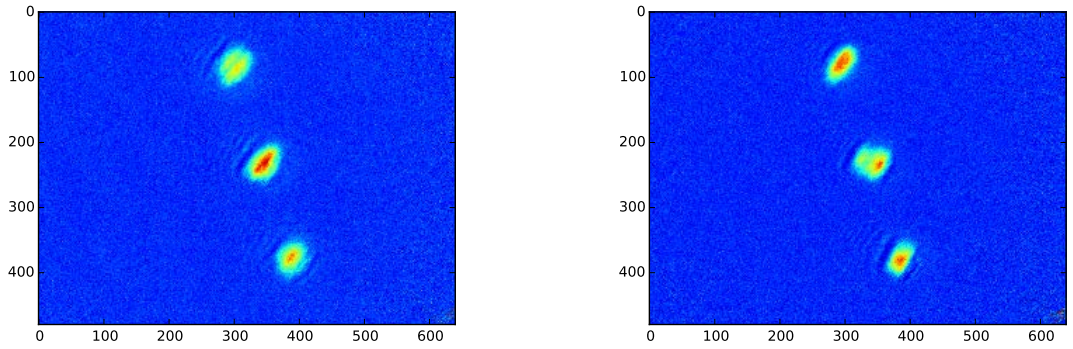

(a) (b)

Figure 5.4: Images of spin domains observed in our system during the course of this experiment. We can observe how the condensate clouds have distorted shapes, indicating that the SMA can not be applied.

is made of flat wire, it has 20 turns and provides a magnetic field gradient of 1.18G/cmA at the centre of the cell. In what follows,I will present the calibration of the BEC as a function of the magnetic field gradient applied .

In figure 5.6(a) and (b) we plot the final magnetization of the system after 3s and 5s of evolution time in the $M - B$ parameter space. We observe that in both cases the difference between the initial and final magnetization of the system is within our error bars ($\simeq 5\%$), proving that the magnetization is conserved in the parameter space that we have explored. Notably, this highlights that dissipative effects such as two and three body losses do not substantially alter the magnetization. Due to the symmetry of the problem, the same behaviour is expected for negative magnetizations.

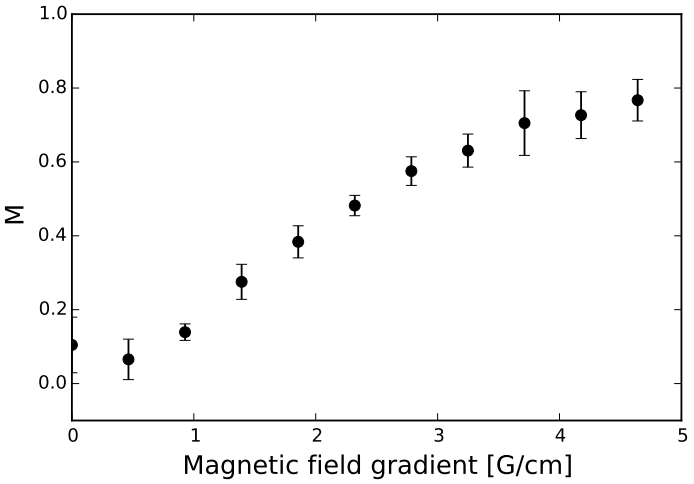

(a)

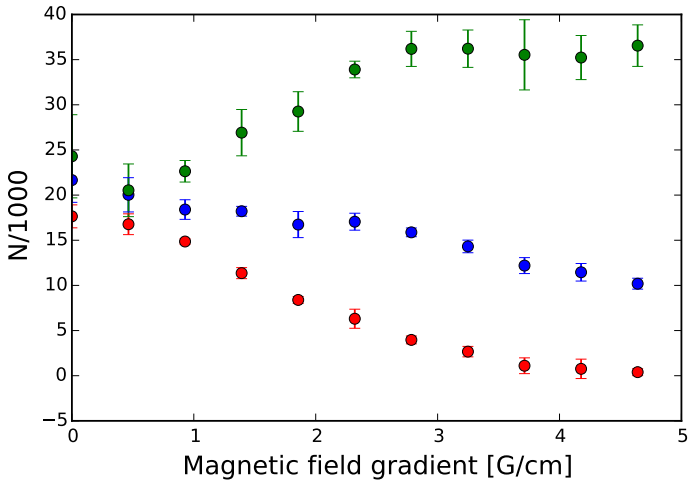

(b)

Figure 5.5: In figure (a) it is displayed the magnetization created on the sample by applying a small magnetic field gradient during the last steps of the evaporation. This method has proven to be reproducible and accurate as a way to prepare initial state samples. The maximum magnetic field gradient applied is $\simeq 0.18 G cm^{-1}$. In (b) we can see the evolution of the number of atoms for each substate as a function of the magnetic field gradient applied to the sample. The red squares corresponds to the $m_F = +1$ state. The blue circles represent the $m_F = 0$ and magenta diamonds stand for $m_F = -1$. The error bars are standard deviations of three different runs of the experiment.

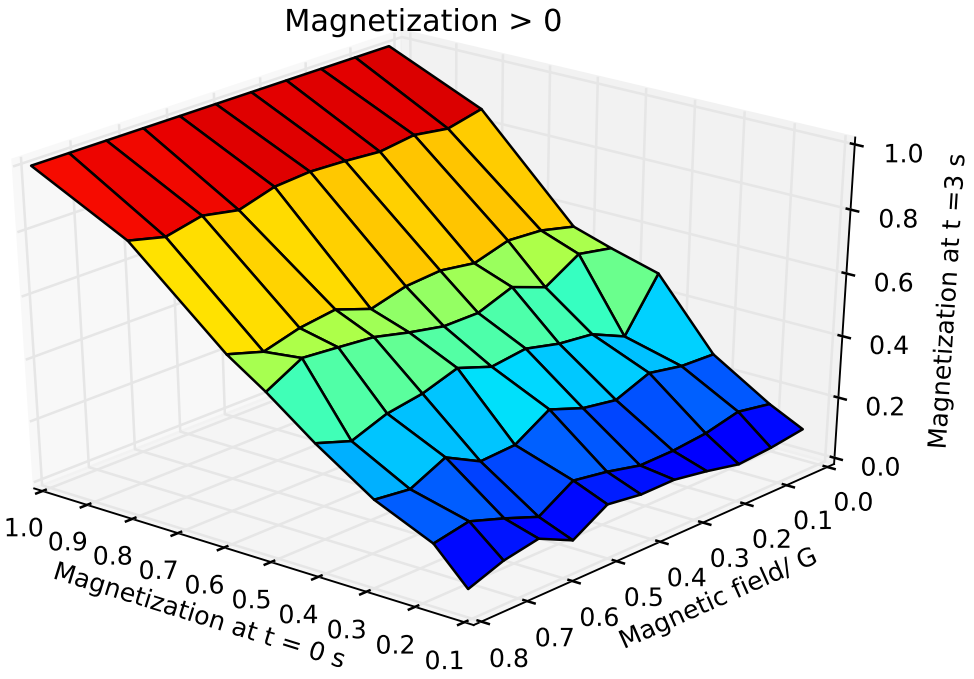

(a)

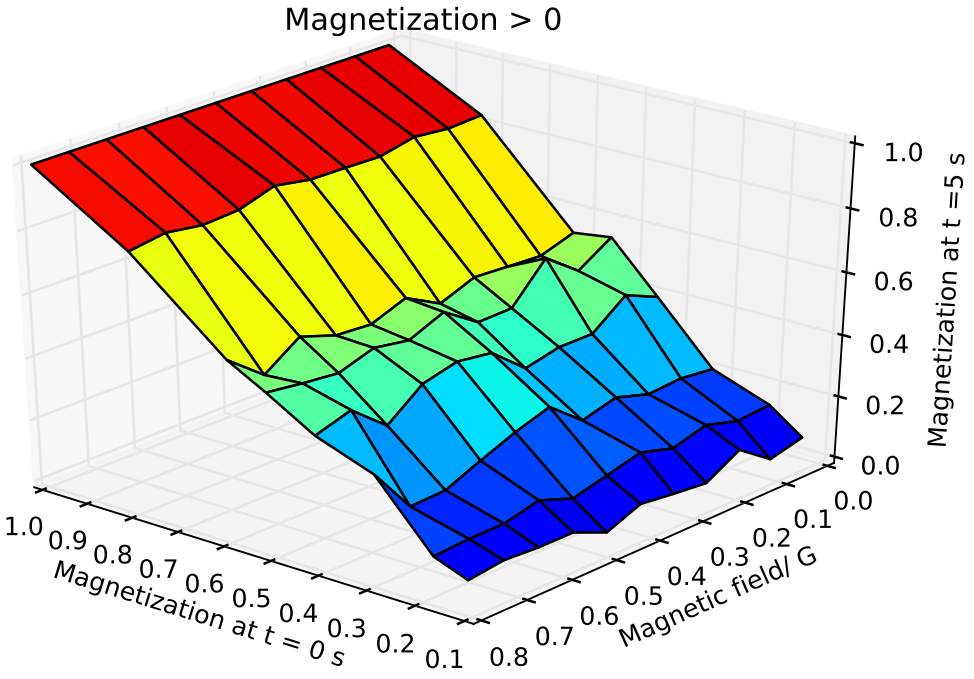

(b)

Figure 5.6: In figure (a) and (b) it is shown the final magnetization of the sample as a function of the initial set magnetization and the external magnetic field applied for 3s and 5s of evolution time.

5.2 Long term equilibrium state of a ferromagnetic spin-1 condensate

While the ground state of an antiferromagnetic condensate has been studied in a number of experimental works and reported extensively [31, 55–57, 116], to the best of our knowledge the ground state of ^{87}Rb has not been reported in a systematic way as a function of both magnetization and external magnetic field. In the previous section 5.1, with the exception of the cases with $M = 0$, $\rho_0 < 0.2$ and $B < 0.1$G (see figure 5.1), I have shown that the magnetization is conserved and that the spin dynamics is completely damped after $\simeq$ 5s, as can be observed in figure 5.5. However, the question arises wether or not the system has reached its ground state, because there are other dynamical processes that have an even longer equilibration time, such as the formation and structural evolution of spin domains. Unfortunately, probing such dynamics requires the use of techniques that can not be implemented in our experiment. This phenomena has been reported in [37].

In this section, we will compare the equilibrium state reached by our system with the ground state predicted by the theory. Typically, theoretical studies of the ground state of these systems do not take into account the dissipative processes that are unavoidable in experiments such as forced evaporation and two and three body losses. Additionally, as explained above, our condensate contains $\sim 10^5$ atoms and therefore we can not apply the SMA as $R_{TF} \sim 4 \times \xi_s$. On the contrary, theoretical studies of the spin-1 ground state properties rely on the validity of the SMA approximation i.e $R_{TF} < \xi_s$. The importance of the SMA in this investigation is unclear.

The ground state of a spin-1 ferromagnetic system has been predicted in the limit of zero magnetic field [27, 28]. For zero magnetic field, the ferromagnetic ground state is simply the state in which all spins point in the same direction, and because the spinor object has rotational symmetry, it can be generally expressed as

$$\vec{\chi} = e^{i\theta}\mathcal{R}\begin{pmatrix}1\\0\\0\end{pmatrix} = e^{i(\theta-\tau)}\begin{pmatrix}e^{-i\alpha}\cos^2(\frac{\beta}{2})\\ \sqrt{2}\cos\left(\frac{\beta}{2}\right)\sin\left(\frac{\beta}{2}\right)\\ e^{i\alpha}\sin^2(\frac{\beta}{2})\end{pmatrix} \tag{5.1}$$

The predictions at zero magnetic field are not possible to achieve experimentally, because the presence of any magnetic field will break the rotational SO(3) symmetry of the spinorial wavefunction as discussed in [68]. The non-zero field needs to be introduced in the theoretical predictions, as in [31, 52, 54]. The presence of the non-zero magnetic field can be taken into account including an extra term H_Z in

the external trapping potential of the Hamiltonian: $U_{ext} = V_{trap}(\vec{x}) + H_Z$. The Zeeman Hamiltonian is $H_Z = \delta_{i,j}E_i$, each E_i given by the Breit-Rabi formula (see equation 1.7c). Within the SMA, the wavefunction of the spinor condensate can be written as $\phi_i(\vec{x}) = \sqrt{N_i}\Phi_i(\vec{x})e^{-i\theta_i}$ with the convention $\int d\vec{x}\sum_i \Phi_i^2 = 1$ and $\theta_{+1} + \theta_{-1} - 2\theta_0 = 0$ as stablished in [28] for ferromagnetic systems. To find the ground state of the spin-1 Hamiltonian with the Zeeman Hamiltonian included we need to minimize the corresponding energy functional:

$$H[\phi_i] = H_S + E_0 N + \frac{c_2}{2}\langle\vec{F}\rangle^2 - p\langle f_z\rangle + q\langle f_z^2\rangle \tag{5.2}$$

The term H_S is symmetric for the exchange of the spin components, and therefore it is independent of the magnetic field value. This implies that to correctly derive the ground state it is necessary to introduce constraints for both the particle number and the magnetization.

From the Hamiltonian in equation 1.27 we can derive the following energy functional within the MF approximation [117]

Where $p = \frac{E_{-1}-E_{+1}}{2}$ and $q = \frac{E_{+1}+E_{-1}-2E_0}{2}$ parametrize the linear and quadratic Zeeman effect. Following [54] for the minimization of equation 5.2, the ground state of the system is found by finding the minimum of the spinor energy function that depends on the external magnetic field:

$$\mathcal{K} = 2c\rho_0(\sqrt{\rho_{+1}} + \sqrt{\rho_{-1}})^2 + q(\rho_{+1} + \rho_{-1}) \tag{5.3}$$

As a consequence of the conservation of number of particles, $1 = \rho_{+1} + \rho_{-1} + \rho_0$ and magnetization $M = \rho_{+1} - \rho_{-1}$, for a condensate in the presence of a fixed magnetic field B, we can parametrize the above equation using a single parameter $\alpha = \rho_{+1} + \rho_{-1}$,

$$\mathcal{K} = 2c\,(1-\alpha)\left(\alpha + \sqrt{\alpha^2 - M^2}\right) \tag{5.4}$$

The solution to the equation above is displayed in the right column of figure 5.7a.

5.2.1 Results and discussion

After loading the dipole trap from the MOT, we do a standard evaporation ramp until we reach the last two stages of the evaporation. Then, we prepare the initial magnetization of the system as described before. At the end of the evaporation, we adiabatically ramp up the power of the 1070nm beam in 50ms to about 10mW. This serves to prevent the system to loose atoms by plain evaporation. During that time, we also ramp the value of the magnetic field from the usual evaporation value to a fixed set value B. The system is left to thermalize for about 100ms more, and then we let the system evolve for another 4s.

Each data point in figure 5.7b is the average of three experimental runs. We sample the space parameter $M - B$, and we measure the fractional population of each Zeeman state. As mentioned before, to obtain the full information about the system, we only need to know the population of the ρ_0 state, and the magnetization. The results are compared with the theoretical predictions in figure 5.7a, for a system within the SMA regime.

We can inmediately notice the clear difference between the theoretical prediction and our results. The theoretical prediction shows a clear increase of ρ_0 for low magnetizations and high fields. On the contrary, our data shows a clear increase for low magnetizations and low fields. The data is in agreement with all our previous observations of spin-mixing dynamics in the system. For high fields, the spin dynamics in our experimental system is greatly suppressed, and therefore the system effectively "freezes" at the initial population values set by the magnetization. This clearly shows that the ground state is not reached, but rather the system equilibrates in a metastable state that does not evolve within our experimental window. For low fields, vanishing magnetizations and small ρ_0, however, the system is still evolving after 7s, and therefore the system does not even reach equilibrium state.

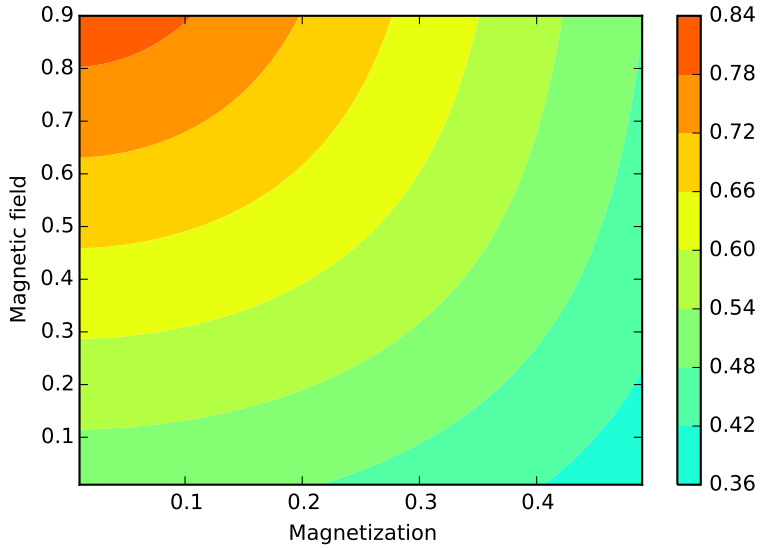

(a)

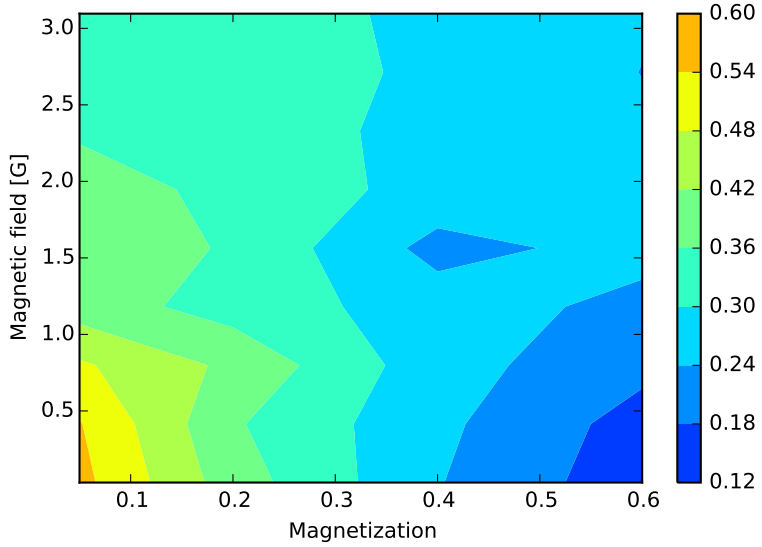

(b)

Figure 5.7: In figure (a) it is plotted the theoretical phase diagram of ρ_0 in the ground state as a function of the external magnetic field and the magnetization of the sample, calculated using equations 5.4 under the SMA approximation. In figure (b), I have plotted the experimental data in the $M - B$ parameter space explored in the experiment.

CHAPTER 6

STUDY OF SPONTANEOUS MAGNETIZATION IN AN EXTERNAL MAGNETIC FIELD

In the previous chapter we have studied the equilibration dynamics of a spin-1 BEC of ^{87}Rb . Our starting point was always a Bose-condensed sample with fixed magnetization, that was our control parameter together with the external magnetic field. In this chapter we are going to investigate the evaporative cooling of the multicomponent spinor BEC in the presence of an external magnetic field. Some theoretical studies have tried to assess this question [118, 119]. However, the assumptions made in these studies are not met in the experiment. This is simply because to achieve the condensation in atomic gases, the experimentalist relies on evaporative cooling, that is a dissipative process. One of the general conclusions of the theoretical studies is that condensation occurs at different temperatures for each Zeeman component. Which component condenses first? At which temperature? Do all three components always condense as a function of the magnetic field? These are natural questions that need to be assessed experimentally. Evaporative cooling does not conserve the number of atoms, but is the magnetization of the system conserved during this process? Does this dissipative process give rise to any magnetic phase of the condensates as a function of the external magnetic field, i.e does a particular value of the field favour the condensation in one of the states? This is expected to happen since the presence of the magnetic field will change the energy of the levels due to the Zeeman shifts, that can be expressed up to quadratic terms as $\Delta E_B = pm_F + q(m_F^2 - 1)$.

The all optical evaporation technique that we use is essential in this study. Other experiments that investigate spinor systems use a combination of radio-frequency evaporation in a magnetic trap in the first place, to later transfer the atoms into a dipole trap for the last stage of the evaporation. The forced evaporation in a magnetic trap produces samples of atoms in the $|F = 2, m_F = -2\rangle$ that need to be transfered to other magnetic substates artificially to prepare an equally distributed sample among the Zeeman levels at a given temperature. In our case all the Zeeman substates are equally populated from

the beginning of the experiment, and we can study the process starting from a high temperature regime.

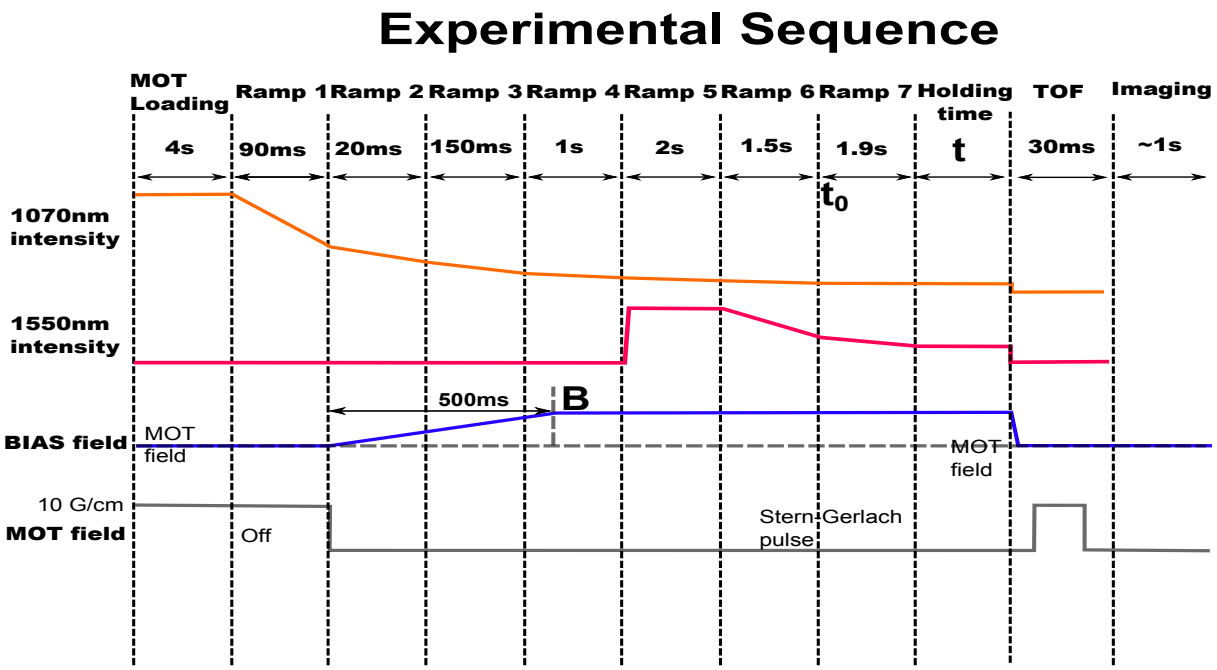

(a)

Figure 6.1: Sketch of the sequence used in this experiment.

6.1 Experimental sequence

In chapter 5, we have presented results showing the long term equilibration dynamics of the system, showing the dependence of the spin-dynamics and relaxation times with the magnetic field applied. We will take this into account when performing our experimental sequence, that starts with loading the atoms into the dipole trap from the MOT following the methods described in section 3.2. Then we start the evaporation sequence. At the same time, we ramp the magnetic field in the vertical direction to a fixed value adiabatically. The evaporation ramp is then performed as usual. We set initial experimental time t_0 (see figure 6.1) at 1.9s before the end of the evaporation ramp. From there on, we stop the evaporation at different times $t \in (800, 1900)$ms. Each time will correspond to a trap depth, that in turn sets a certain temperature $T(t)$. The calibration of the temperature was done measuring the temperature of the whole BEC for each evaporation time. After the evaporation stops, we wait 100ms more to allow thermalization of the atoms in the trap, and then we wait for 3s more to allow the system to equilibrate through spin-mixing collisions. Then we perform a Stern-Gerlach measurement of the population of each Zeeman sublevel. We do this for values of $B \in (0, 37)$G in steps of $\simeq 0.8$G. We detect the atoms after 30ms TOF, and we apply different fits to the clouds depending on their properties (Gaussian, Bimodal

or Thomas-Fermi profiles are fitted in a post-processing stage) to extract the total number of atoms and the condensate fraction of the clouds.

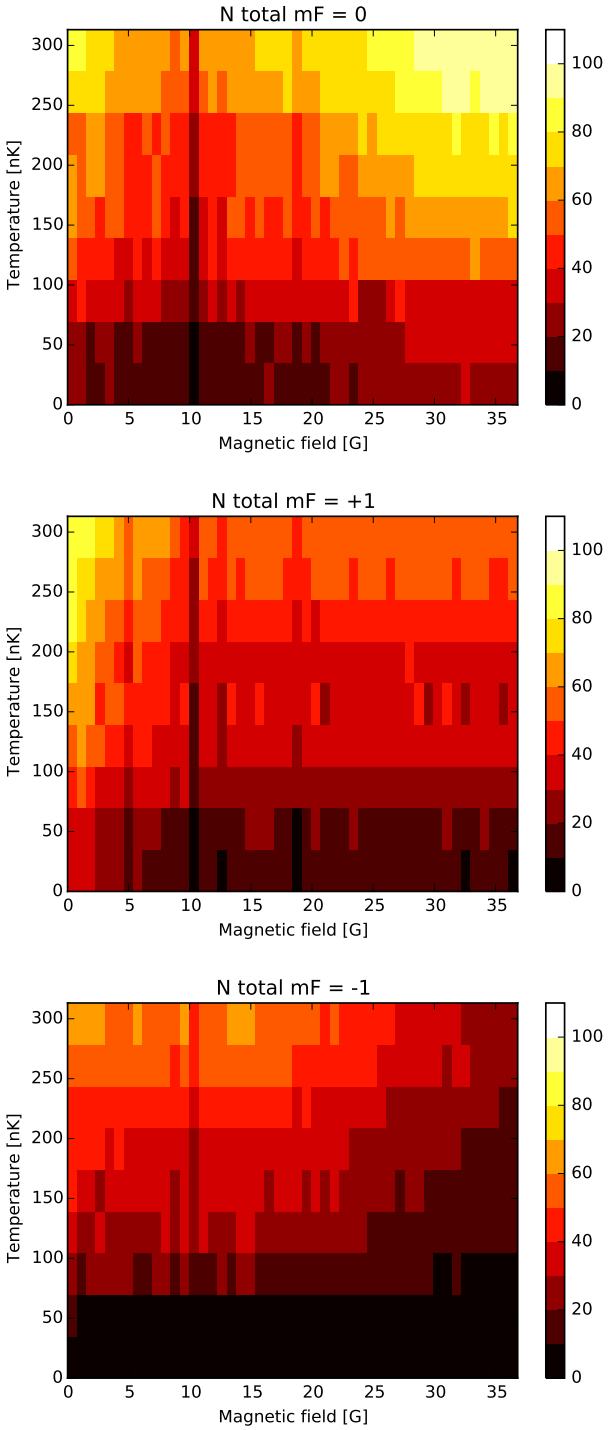

Figure 6.2: The figure shows the total number of atoms in each Zeeman state during the forced evaporation as a function of the magnetic field. The color scale displays the total number of atoms in thousands.

6.2 First results

In figure 6.2 I have plotted the total number of atoms in each Zeeman state for each temperature and magnetic field (the color bar indicates number of atoms in thousands). Although at high temperatures we start with an equally distributed population among the three levels, we can appreciate that in general, the number of atoms in $m_F = -1$ is smaller than in the other two states. For temperatures $T > 150$nK, we can observe two clear regimes as a function of the magnetic field applied. For magnetic fields $B < 10$G, the population of the $m_F = +1$ is larger than the other two states. For higher fields, such that $B > 25$G, it is in turn the $m_F = 0$ state that it is most populated, while the $m_F = -1$ decreases. Overall, the number of atoms decreases with the temperature, as expected due to the evaporation process.

Remark A common feature in the data shown in figure 6.2 is a depletion of the number of atoms around $B \simeq 10$G. The effect is enhanced by plotting a horizontal slice, as in figure 6.3. We can also observe that this feature is already present at high temperatures, and it has sharp boundaries as a function of the magnetic field. The atom losses are higher for the $m_F = 0$ and $m_F = +1$ states. This might be the signature of a Feshbach resonance happening at high temperatures between these two Zeeman states. For now, the nature of this feature remains unexplored, and it will be the subject of future investigations.

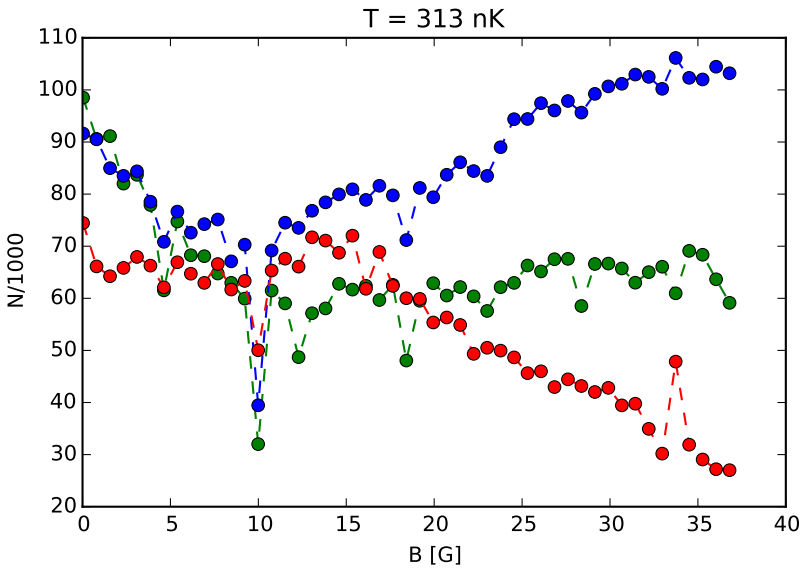

Figure 6.3: Number of atoms in each state as a function of the magnetic field, for a temperature of 313nK. Blue, green and red solid points correspond to $m_F = 0$, $m_F = +1$ and $m_F = -1$ states. The dash line serves as a guide for the eye.

In figure 6.4, I have plotted the number of condensed atoms in each magnetic substate. We observe the different behaviour of each state. In the first place we can observe that condensation occurs at different temperatures for each Zeeman state as a general feature. The $m_F = 0$ state tends to condense always first, followed by the $m_F = +1$. The $m_F = -1$ condenses the last. For fields $B > 25$, the number of atoms in $m_F = -1$ is too low to achieve condensation. Overall, we can observe two different regimes of the condensed fraction as a function of the magnetic field. At low magnetic fields $B < 5$G, the condensate fraction of the $m_F = +1$ increases towards vanishing fields and becomes the most populated state. On the contrary, at magnetic fields $B > 25$G, the $m_F = 0$ becomes the most populated state.

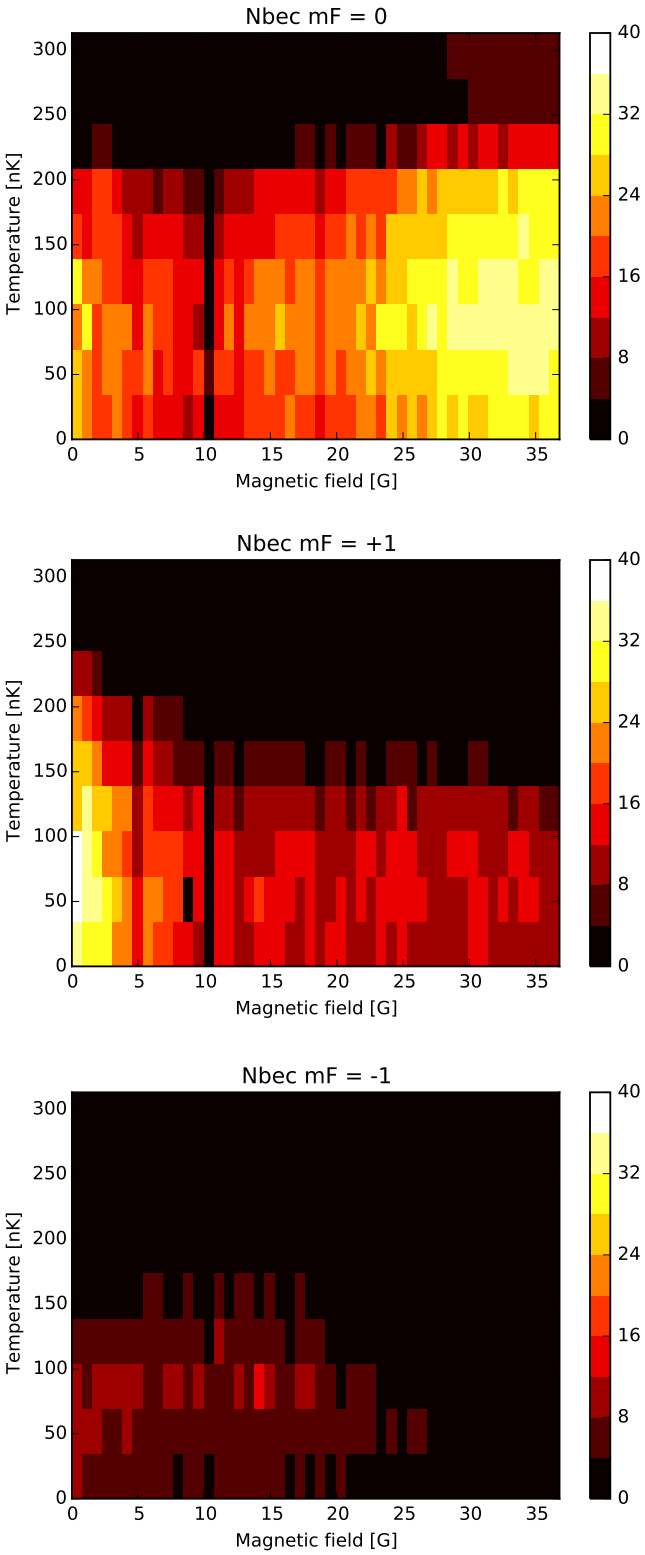

Figure 6.4: The figure shows the total number of condensed atoms in each Zeeman state during the forced evaporation as a function of the magnetic field. As before, the color scale displays the total number of atoms in thousands.

Regarding the magnetization, we observe two interesting things. In figure 6.5a, we can observe a plot of the magnetization corresponding to the whole system i.e thermal and condensed fractions. Surprisingly, despite the evaporation being a dissipative process, we observe that the magnetization of the system is almost uniform, with a slightly positive value in the whole region of parameters that we have explored, excepting a slightly negative area around the values of the magnetic field that enhance the losses of the $m_F = 0$ and $m_F = +1$ states. In figure 6.5b, I have plotted the magnetization of the BEC fraction of the sample. Also here, we can observe a uniform distribution of the magnetization, except for a small region. This region is located at low magnetic fields $B \leq 5$G and high temperatures $T > 150$nK. The BEC magnetization there shows a peak $M \simeq 0.8$, indicating a highly magnetized region. In general, at low fields, there is a preference for the $m_F = +1$ state, which is what should be expected from the theoretical predictions of the ground state of a ferromagnetic spin-1 system in the absence of a magnetic field.

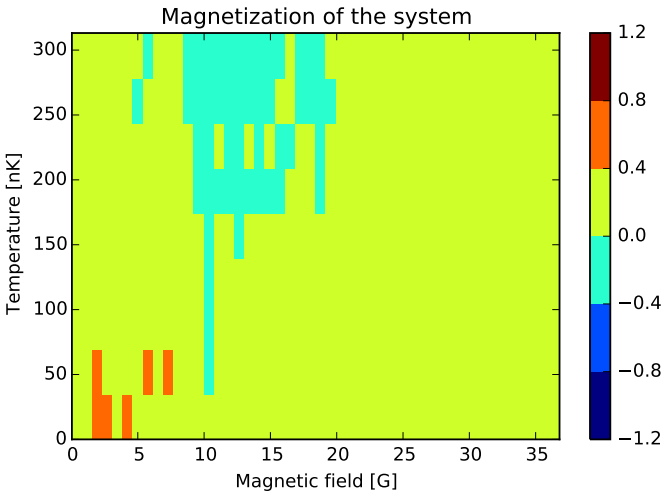

(a)

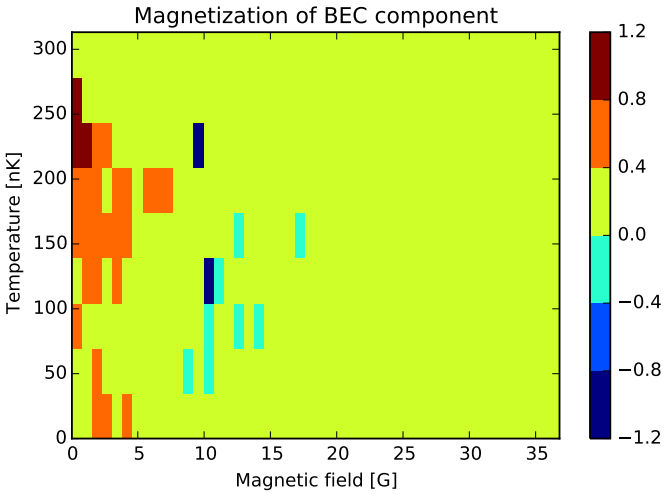

(b)

Figure 6.5: Figure (a) shows the total magnetization of the system during the forced evaporation process as a function of the magnetic field. Figure (b) shows the magnetization of the condensate fraction of the system.

To conclude, I have shown the preliminary results of the investigation of the BEC formation process in a spin-1 ferromagnetic quantum gas subject to an external magnetic field. The system displays non trivial features, such as multi-step condensation and enhaced losses as a function of the magnetic field. These are consequence of the interspecies collisional processes, as well as the interplay between the condensed atoms and the thermal cloud during the evaporation process.

SUMMARY AND OUTLOOK

The majority of my thesis work has been devoted to the construction, optimization and characterization of an experimental apparatus, capable of creating spinor condensates of $\simeq 1\times10^5$ atoms with a repetition rate of 10s, using an all-optical evaporation technique. In this thesis, I have reported a complete description of the experimental apparatus and techniques used in the experiment and a complete characterization of the BEC sample. The achievement of a working experiment has represented the milestone of my thesis work, and allowed me to start investigating some interesting physics:

- We have studied the transmission of absorption imaging pictures through a coherent fiber bundle. This paves the way towards the use of such devices in quantum degenerate gases experiments in which the system requires strong isolation from the environment.

- We have explored the equilibration dynamics of our system as a function of the initial magnetization of the sample and the external magnetic field. We have assessed some questions regarding the conservation of magnetization during the equilibration of the system. An interesting effect due to the size of our BEC samples that supresses the spin dynamics of the system has been observed. The equilibrium state at long evolution times was reported and compared to the SMA theoretical prediction of the ground state of a spin-1 ferromagnetic system.

- The process of the formation of a BEC remains as an interesting question, despite the fact that the issue was raised long ago [120, 121]. In particular, I have presented the first results of an ongoing investigation on the BEC formation of a spin-1 quantum gas in the presence of an external magnetic field. Interesting phenomena such as step-wise condensation or possible interspecies Feshbach resonances at low magnetic fields have been observed, and they will be subject of a more in-depth investigation in the future.

The possibility of realizing BEC samples in which multiple components are present, including the possibility of coupling these states to different hyperfine manifolds enriches the possibilities of using this system as a powerful quantum simulator. To this end, we will additionally implement a high resolution imaging system and a DMD, that will allow us to imprint topological defects onto our spinor BEC. It has

been demonstrated that coherently driven spinor Bose gases can simulate classical field theory confinement and string breaking [122]. In this system, dimer vortices appear as couples of half-vortices (one vortex in each component) connected by a well defined pattern in the relative phase (sine-Gordon soliton), corresponding to a constant force. When the distance between the half-vortices exceeds a certain value, the dimer spontaneously breaks into pairs of half-vortices, with a mechanism similar to that of string breaking in QCD. This simulator will allow to understand the role of creation and decay of domain walls in the sine-Gordon field theory, with immediate impact on the theory of axions and on the physics of high-density quark matter (like neutron stars). Additionally, Hawking radiation is one of the effects predicted by Quantum Field Theories on curved spacetime, which represents a first step towards including effects of gravity into the dynamics of quantum matter fields. This phenomenon, firstly introduced studying black holes, seems to be practically not observable in this context. However, the close analogy between sound propagation on a background hydrodynamic flow and field propagation in a curved spacetime led to the first realization of sonic Hawking radiation with an event horizon (the region between a subsonic and a supersonic flow) for a single BEC [123]. The richer structure of a multicomponent system and the possibility of coherent coupling between the different components allows new insights in the physics of Hawking radiation [124]. Furthermore, it will be possible to circumvent the issues that make Hawking radiation in single component BECs still devated, like the presence of quantum correlations between the phonons across the event horizon.

BIBLIOGRAPHY

[1] M H Anderson, J R Ensher, M R Matthews, C E Wieman, and E a Cornell. Observation of bose-einstein condensation in a dilute atomic vapor. *Science (New York, N.Y.)*, 269(5221):198–201, July 1995.

[2] M.-O. Mewes, M. R. Andrews, N. J. van Druten, D. M. Kurn, D. S. Durfee, C. G. Townsend, and W. Ketterle. Collective excitations of a bose-einstein condensate in a magnetic trap. *Phys. Rev. Lett.*, 77:988–991, Aug 1996.

[3] Dale G. Fried, Thomas C. Killian, Lorenz Willmann, David Landhuis, Stephen C. Moss, Daniel Kleppner, and Thomas J. Greytak. Bose-einstein condensation of atomic hydrogen. *Phys. Rev. Lett.*, 81:3811–3814, Nov 1998.

[4] A. Ashkin. Acceleration and trapping of particles by radiation pressure. *Phys. Rev. Lett.*, 24:156–159, Jan 1970.

[5] Steven Chu, J. E. Bjorkholm, A. Ashkin, and A. Cable. Experimental observation of optically trapped atoms. *Phys. Rev. Lett.*, 57:314–317, Jul 1986.

[6] Steven Chu. Nobel lecture: The manipulation of neutral particles. *Rev. Mod. Phys.*, 70:685–706, Jul 1998.

[7] Claude N. Cohen-Tannoudji. Nobel lecture: Manipulating atoms with photons. *Rev. Mod. Phys.*, 70:707–719, Jul 1998.

[8] William D. Phillips. Nobel lecture: Laser cooling and trapping of neutral atoms. *Rev. Mod. Phys.*, 70:721–741, Jul 1998.

[9] Wolfgang Ketterle. Nobel lecture: When atoms behave as waves: Bose-einstein condensation and the atom laser. *Rev. Mod. Phys.*, 74:1131–1151, Nov 2002.

[10] D S Hall, J R Ensher, D S Jin, M R Matthews, C E Wieman, and E A Cornell. Recent Experiments with Bose-Condensed Gases at JILA. *Proc. SPIE*, (3270), 1998.

[11] C. J. Myatt, E. A. Burt, R. W. Ghrist, E. A. Cornell, and C. E. Wieman. Production of two overlapping bose-einstein condensates by sympathetic cooling. *Phys. Rev. Lett.*, 78:586–589, Jan 1997.

[12] M. D. Barrett, J. A. Sauer, and M. S. Chapman. All-optical formation of an atomic bose-einstein condensate. *Phys. Rev. Lett.*, 87:010404, Jun 2001.

[13] Tetsuo Ohmi and Kazushige Machida. Bose-Einstein Condensation with Internal Degrees of Freedom in Alkali Atom Gases. *Journal of the Physical Society of Japan*, 67(6):1822–1825, June 1998.

[14] Tin-Lun Ho. Spinor bose condensates in optical traps. *Phys. Rev. Lett.*, 81:742–745, Jul 1998.

[15] Yuki Kawaguchi, Hiroki Saito, and Masahito Ueda. Can spinor dipolar effects be observed in bose-einstein condensates? *Phys. Rev. Lett.*, 98:110406, Mar 2007.

[16] M Vengalattore, S R Leslie, and J Guzman. Spontaneously modulated spin textures in a dipolar spinor Bose-Einstein condensate. *Physical review letters*, 100(170403):4–7, 2008.

[17] Yuki Kawaguchi, Hiroki Saito, Kazue Kudo, and Masahito Ueda. Spontaneous magnetic ordering in a ferromagnetic spinor dipolar bose-einstein condensate. *Phys. Rev. A*, 82:043627, Oct 2010.

[18] S. Yi and H. Pu. Spontaneous spin textures in dipolar spinor condensates. *Phys. Rev. Lett.*, 97:020401, Jul 2006.

[19] T Lahaye, C Menotti, L Santos, M Lewenstein, and T Pfau. The physics of dipolar bosonic quantum gases. *Reports on Progress in Physics*, 72(12):126401, 2009.

[20] Mingwu Lu, Seo Ho Youn, and Benjamin L. Lev. Trapping ultracold dysprosium: A highly magnetic gas for dipolar physics. *Phys. Rev. Lett.*, 104:063001, Feb 2010.

[21] K. Aikawa, A. Frisch, M. Mark, S. Baier, A. Rietzler, R. Grimm, and F. Ferlaino. Bose-einstein condensation of erbium. *Phys. Rev. Lett.*, 108:210401, May 2012.

[22] Daniel Benedicto-Orenes, Anna Kowalczyk, Kai Bongs, and Giovanni Barontini. Endoscopic imaging of quantum gases through a fiber bundle. *Opt. Express*, 25(17):19701–19710, Aug 2017.

[23] D. S. Hall, M. R. Matthews, J. R. Ensher, C. E. Wieman, and E. A. Cornell. Dynamics of component separation in a binary mixture of bose-einstein condensates. *Phys. Rev. Lett.*, 81:1539–1542, Aug 1998.

[24] G. Modugno, M. Modugno, F. Riboli, G. Roati, and M. Inguscio. Two atomic species superfluid. *Phys. Rev. Lett.*, 89:190404, Oct 2002.

[25] D. M. Stamper-Kurn and W. Ketterle. Spinor condensates and light scattering from bose-einstein condensates. In R. Kaiser, C. Westbrook, and F. David, editors, *Coherent atomic matter waves*, volume 72, pages 139–217. Springer Berlin Heidelberg, 2001. DOI: 10.1007/3-540-45338-5_2.

[26] M. H. Anderson, J. R. Ensher, M. R. Matthews, C. E. Wieman, and E. A. Cornell. Observation of bose-einstein condensation in a dilute atomic vapor. *Science*, 269(5221):198–201, 1995.

[27] Tin-Lun Ho. Spinor bose condensates in optical traps. *Phys. Rev. Lett.*, 81:742–745, Jul 1998.

[28] Tetsuo Ohmi and Kazushige Machida. Bose-einstein condensation with internal degrees of freedom in alkali atom gases. *Journal of the Physical Society of Japan*, 67(6):1822–1825, 1998.

[29] C. K. Law, H. Pu, and N. P. Bigelow. Quantum spins mixing in spinor bose-einstein condensates. *Phys. Rev. Lett.*, 81:5257–5261, Dec 1998.

[30] Masato Koashi and Masahito Ueda. Exact eigenstates and magnetic response of spin-1 and spin-2 bose-einstein condensates. *Phys. Rev. Lett.*, 84:1066–1069, Feb 2000.

[31] J. Stenger, S. Inouye, D. M. Stamper-Kurn, H.-J. Miesner, A. P. Chikkatur, and W. Ketterle. Spin domains in ground-state bose-einstein condensates. *Nature*, 396(6709):345–348.

[32] H.-J. Miesner, D. M. Stamper-Kurn, J. Stenger, S. Inouye, A. P. Chikkatur, and W. Ketterle. Observation of metastable states in spinor bose-einstein condensates. *Phys. Rev. Lett.*, 82:2228–2231, Mar 1999.

[33] D. M. Stamper-Kurn, H.-J. Miesner, A. P. Chikkatur, S. Inouye, J. Stenger, and W. Ketterle. Quantum tunneling across spin domains in a bose-einstein condensate. *Phys. Rev. Lett.*, 83:661–665, Jul 1999.

[34] Tomoya Isoshima, Kazushige Machida, and Tetsuo Ohmi. Spin-domain formation in spinor bose-einstein condensation. *Phys. Rev. A*, 60:4857–4863, Dec 1999.

[35] Jay D. Sau, S. R. Leslie, D. M. Stamper-Kurn, and Marvin L. Cohen. Theory of domain formation in inhomogeneous ferromagnetic dipolar condensates within the truncated wigner approximation. *Phys. Rev. A*, 80:023622, Aug 2009.

[36] J. Guzman, G.-B. Jo, A. N. Wenz, K. W. Murch, C. K. Thomas, and D. M. Stamper-Kurn. Long-time-scale dynamics of spin textures in a degenerate $f = 1$ ^{87}rb spinor bose gas. *Phys. Rev. A*, 84:063625, Dec 2011.

[37] M. Vengalattore, J. Guzman, S. R. Leslie, F. Serwane, and D. M. Stamper-Kurn. Periodic spin textures in a degenerate $f = 1$ ^{87}rb spinor bose gas. *Phys. Rev. A*, 81:053612, May 2010.

[38] M. Vengalattore, S. R. Leslie, J. Guzman, and D. M. Stamper-Kurn. Spontaneously modulated spin textures in a dipolar spinor bose-einstein condensate. *Phys. Rev. Lett.*, 100:170403, May 2008.

[39] L. E. Sadler, J. M. Higbie, S. R. Leslie, M. Vengalattore, and D. M. Stamper-Kurn. Spontaneous symmetry breaking in a quenched ferromagnetic spinor bose-einstein condensate. *Nature*, 443(7109):312–315.

[40] N Horiguchi, T Oka, and H Aoki. Non-equilibrium dynamics in mott-to-superfluid transition in bose-einstein condensation in optical lattices. *Journal of Physics: Conference Series*, 150(3):032007, 2009.

[41] C.S. et al. Gerving. Non-equilibrium dynamics of an unstable quantum pendulum explored in a spin-1 bose-einstein condensate. *Nat. Commun.*, 3:1169, (2012).

[42] M. Anquez, B. A. Robbins, H. M Bharath, M. Boguslawski, T. M. Hoang, and M. S. Chapman. Quantum kibble-zurek mechanism in a spin-1 bose-einstein condensate. *Phys. Rev. Lett.*, 116:155301, Apr 2016.

[43] H. Schmaljohann, M. Erhard, J. Kronjäger, M. Kottke, S. van Staa, L. Cacciapuoti, J. J. Arlt, K. Bongs, and K. Sengstock. Dynamics of $f = 2$ spinor bose-einstein condensates. *Phys. Rev. Lett.*, 92:040402, Jan 2004.

[44] Axel Griesmaier, Jörg Werner, Sven Hensler, Jürgen Stuhler, and Tilman Pfau. Bose-einstein condensation of chromium. *Phys. Rev. Lett.*, 94:160401, Apr 2005.

[45] M.-S. Chang, C. D. Hamley, M. D. Barrett, J. A. Sauer, K. M. Fortier, W. Zhang, L. You, and M. S. Chapman. Observation of spinor dynamics in optically trapped ^{87}Rb bose-einstein condensates. *Phys. Rev. Lett.*, 92:140403, Apr 2004.

[46] Wenxian Zhang, D. L. Zhou, M.-S. Chang, M. S. Chapman, and L. You. Coherent spin mixing dynamics in a spin-1 atomic condensate. *Phys. Rev. A*, 72:013602, Jul 2005.

[47] C. D. Hamley, C. S. Gerving, T. M. Hoang, E. M. Bookjans, and M. S. Chapman. Spin-nematic squeezed vacuum in a quantum gas. *Nature Physics*, 8:305–308, 2012.

[48] Özgür E. Müstecaplıoğlu, M. Zhang, and L. You. Spin squeezing and entanglement in spinor condensates. *Phys. Rev. A*, 66:033611, Sep 2002.

[49] T. M. Hoang, M. Anquez, B. A. Robbins, X. Y. Yang, B. J. Land, C. D. Hamley, and M. S. Chapman. Parametric excitation and squeezing in a many-body spinor condensate. *Nature Communications*, 7:11233, 2016.

[50] A. E. Leanhardt, Y. Shin, D. Kielpinski, D. E. Pritchard, and W. Ketterle. Coreless vortex formation in a spinor bose-einstein condensate. *Phys. Rev. Lett.*, 90:140403, Apr 2003.

[51] Wenxian Zhang, Ö. E. Müstecaplıoğlu, and L. You. Solitons in a trapped spin-1 atomic condensate. *Phys. Rev. A*, 75:043601, Apr 2007.

[52] Wenxian Zhang, Su Yi, and L. You. Bose-einstein condensation of trapped interacting spin-1 atoms. *Phys. Rev. A*, 70:043611, Oct 2004.

[53] Keiji Murata, Hiroki Saito, and Masahito Ueda. Broken-axisymmetry phase of a spin-1 ferromagnetic bose-einstein condensate. *Phys. Rev. A*, 75:013607, Jan 2007.

[54] Wenxian Zhang, Su Yi, and Li You. Mean field ground state of a spin-1 condensate in a magnetic field. *New Journal of Physics*, 5(1):77, 2003.

[55] David Jacob, Lingxuan Shao, Vincent Corre, Tilman Zibold, Luigi De Sarlo, Emmanuel Mimoun, Jean Dalibard, and Fabrice Gerbier. Phase diagram of spin-1 antiferromagnetic bose-einstein condensates. *Phys. Rev. A*, 86:061601, Dec 2012.

[56] Y. Liu, S. Jung, S. E. Maxwell, L. D. Turner, E. Tiesinga, and P. D. Lett. Quantum phase transitions and continuous observation of spinor dynamics in an antiferromagnetic condensate. *Phys. Rev. Lett.*, 102:125301, Mar 2009.

[57] J. Jiang, L. Zhao, M. Webb, and Y. Liu. Mapping the phase diagram of spinor condensates via adiabatic quantum phase transitions. *Phys. Rev. A*, 90:023610, Aug 2014.

[58] Yuki Kawaguchi, Hiroki Saito, and Masahito Ueda. Can spinor dipolar effects be observed in bose-einstein condensates? *Phys. Rev. Lett.*, 98:110406, Mar 2007.

[59] M. Takahashi, Sankalpa Ghosh, T. Mizushima, and K. Machida. Spinor dipolar bose-einstein condensates: Classical spin approach. *Phys. Rev. Lett.*, 98:260403, Jun 2007.

[60] Kevin Gross, Chris P. Search, Han Pu, Weiping Zhang, and Pierre Meystre. Magnetism in a lattice of spinor bose-einstein condensates. *Phys. Rev. A*, 66:033603, Sep 2002.

[61] Dariusz Kajtoch and Emilia Witkowska. Spin squeezing in dipolar spinor condensates. *Phys. Rev. A*, 93:023627, Feb 2016.

[62] Daniel A. Steck. "Rubidium 87 D Line Data", avilable online at *http://steck.us/alkalidata* (revision 2.1.5, 13 January 2015) .

[63] Christopher J. Foot. *Atomic Physics*. Oxford University Press, 2013.

[64] Christopher Gill. *Simulating Transport Through Quantum Networks in the Presence of Classical Noise Using Cold Atoms*. PhD thesis, School of Physics and Astronomu, University of Birmingham, 2016.

[65] E. G. M. van Kempen, S. J. J. M. F. Kokkelmans, D. J. Heinzen, and B. J. Verhaar. Interisotope determination of ultracold rubidium interactions from three high-precision experiments. *Phys. Rev. Lett.*, 88:093201, Feb 2002.

[66] Ming-Shien Chang, Qishu Qin, Wenxian Zhang, Li You, and Michael S. Chapman. Coherent spinor dynamics in a spin-1 bose condensate. *Nature Physics*, 1:111–116, 2005.

[67] Yuki Kawaguchi and Masahito Ueda. Spinor bose-einstein condensates. *Physics Reports*, 520(5):253–381, 2012.

[68] S. Yi, Ö. E. Müstecaplıoğlu, C. P. Sun, and L. You. Single-mode approximation in a spinor-1 atomic condensate. *Phys. Rev. A*, 66:011601, Jul 2002.

[69] Franco Dalfovo, Stefano Giorgini, Lev P. Pitaevskii, and Sandro Stringari. Theory of bose-einstein condensation in trapped gases. *Rev. Mod. Phys.*, 71:463–512, Apr 1999.

[70] C. Samuelis, E. Tiesinga, T. Laue, M. Elbs, H. Knöckel, and E. Tiemann. Cold atomic collisions studied by molecular spectroscopy. *Phys. Rev. A*, 63:012710, Dec 2000.

[71] G. Ritt, G. Cennini, C. Geckeler, and M. Weitz. Laser frequency offset locking using a side of filter technique. *Applied Physics B*, 79(3):363–365, June 2004.

[72] Saptarishi Chaudhuri, Sanjukta Roy, and C. S. Unnikrishnan. Realization of an intense cold rb atomic beam based on a two-dimensional magneto-optical trap: Experiments and comparison with simulations. *Phys. Rev. A*, 74:023406, Aug 2006.

[73] K. Dieckmann, R. J. C. Spreeuw, M. Weidemüller, and J. T. M. Walraven. Two-dimensional magneto-optical trap as a source of slow atoms. *Phys. Rev. A*, 58:3891–3895, Nov 1998.

[74] Available online at *https://github.com/morefigs/pymba*.

[75] M. W. Zwierlein W. Ketterle. Making, probing and understanding ultracold fermi gases. *La Rivista del Nuovo Cimento*, (506):247, 2008.

[76] Aviv Keshet and Wolfgang Ketterle. A distributed, graphical user interface based, computer control system for atomic physics experiments. *Review of Scientific Instruments*, 84(1):015105, January 2013.

[77] Available online at *https://github.com/akeshet/Cicero-Word-Generator*.

[78] O. J. Luiten, M. W. Reynolds, and J. T. M. Walraven. Kinetic theory of the evaporative cooling of a trapped gas. *Phys. Rev. A*, 53:381–389, Jan 1996.

[79] Wolfgang Ketterle and N.J. Van Druten. Evaporative cooling of trapped atoms. *Advances In Atomic, Molecular, and Optical Physics*, 37:181 – 236, 1996.

[80] K.J. Arnold and M.D. Barrett. All-optical bose-einstein condensation in a 1.06μm dipole trap. *Optics Communications*, 284(13):3288 – 3291, 2011.

[81] Toshiya Kinoshita, Trevor Wenger, and David S. Weiss. All-optical bose-einstein condensation using a compressible crossed dipole trap. *Phys. Rev. A*, 71:011602, Jan 2005.

[82] Chen-Lung Hung, Xibo Zhang, Nathan Gemelke, and Cheng Chin. Accelerating evaporative cooling of atoms into bose-einstein condensation in optical traps. *Phys. Rev. A*, 78:011604, Jul 2008.

[83] Q. Beaufils, R. Chicireanu, T. Zanon, B. Laburthe-Tolra, E. Maréchal, L. Vernac, J.-C. Keller, and O. Gorceix. All-optical production of chromium bose-einstein condensates. *Phys. Rev. A*, 77:061601, Jun 2008.

[84] Rudolf Grimm, Matthias WeidemÃ$\frac{1}{4}$ller, and Yurii B. Ovchinnikov. Optical dipole traps for neutral atoms. In *Advances In Atomic, Molecular, and Optical Physics*, volume 42, pages 95–170. Elsevier. DOI: 10.1016/S1049-250X(08)60186-X.

[85] Huang Wu, Ennio Arimondo, and Christopher J. Foot. Dynamics of evaporative cooling for bose-einstein condensation. *Phys. Rev. A*, 56:560–569, 1997.

[86] S. Friebel, C. D'Andrea, J. Walz, M. Weitz, and T. W. Hänsch. co_2. *Phys. Rev. A*, 57:R20–R23, Jan 1998.

[87] R. Jáuregui, N. Poli, G. Roati, and G. Modugno. Anharmonic parametric excitation in optical lattices. *Phys. Rev. A*, 64:033403, Aug 2001.

[88] S. Stringari. Collective excitations of a trapped bose-condensed gas. *Phys. Rev. Lett.*, 77:2360–2363, Sep 1996.

[89] T. W. Kornack, S. J. Smullin, S.-K. Lee, and M. V. Romalis. A low-noise ferrite magnetic shield. 90(22):223501, 2007.

[90] M. Koschorreck, M. Napolitano, B. Dubost, and M. W. Mitchell. High resolution magnetic vector-field imaging with cold atomic ensembles. *Applied Physics Letters*, 98(7):074101, 2011.

[91] Igor Moric, Philippe Laurent, Philippe Chatard, Charles-Marie de Graeve, Stephane Thomin, Vincent Christophe, and Olivier Grosjean. Magnetic shielding of the cold atom space clock PHARAO. 102:287–294.

[92] T. Kovachy, P. Asenbaum, C. Overstreet, C. A. Donnelly, S. M. Dickerson, A. Sugarbaker, J. M. Hogan, and M. A. Kasevich. Quantum superposition at the half-metre scale. *Nature*, 528:530–533, 2015.

[93] Immanuel Bloch, Jean Dalibard, and Sylvain Nascimbène. Quantum simulations with ultracold quantum gases. *Nature Physics*, 8(4):267–276, 2012.

[94] C. Roux, A. Emmert, A. Lupascu, T. Nirrengarten, G. Nogues, M. Brune, J.-M. Raimond, and S. Haroche. Bose-einstein condensation on a superconducting atom chip. *Europhysics Letters*, 81(5):56004, 2008.

[95] S. Bernon, H. Hattermann, D. Bothner, M. Knufinke, P. Weiss, F. Jessen, D. Cano, M. Kemmler, R. Kleiner, D. Koelle, and J. Fortagh. Manipulation and coherence of ultra-cold atoms on a superconducting atom chip. *Nature Communications*, 4, 2013.

[96] K. Beloy, N. Hinkley, N. B. Phillips, J. A. Sherman, M. Schioppo, J. Lehman, A. Feldman, L. M. Hanssen, C. W. Oates, and A. D. Ludlow. Atomic clock with 1×10^{-18} room-temperature blackbody stark uncertainty. *Phys. Rev. Lett.*, 113:260801, Dec 2014.

[97] J. Kronjaeger R. Wiesendanger K. Bongs E. Y. Vedmedenko, M. Schult and K. Sengstock. Collective magnetism in arrays of spinor bose-einstein condensates. *New Journal of Physics*, 15(6):063033, 2013.

[98] Yuki Kawaguchi, Hiroki Saito, and Masahito Ueda. Can spinor dipolar effects be observed in bose-einstein condensates? *Phys. Rev. Lett.*, 98:110406, Mar 2007.

[99] Mingwu Lu, Seo Ho Youn, and Benjamin L. Lev. Trapping ultracold dysprosium: A highly magnetic gas for dipolar physics. *Phys. Rev. Lett.*, 104:063001, Feb 2010.

[100] A. Frisch, M. Mark, K. Aikawa, S. Baier, R. Grimm, A. Petrov, S. Kotochigova, G. Quéméner, M. Lepers, O. Dulieu, and F. Ferlaino. Ultracold dipolar molecules composed of strongly magnetic atoms. *Phys. Rev. Lett.*, 115:203201, Nov 2015.

[101] E. A. Donley, E. Hodby, L. Hollberg, and J. Kitching. Demonstration of high-performance compact magnetic shields for chip-scale atomic devices. *Review of Scientific Instruments*, 78(8):083102, 2007.

[102] Andrew R. Rouse and Arthur F. Gmitro. Multispectral imaging with a confocal microendoscope. *Opt. Lett.*, 25(23):1708–1710, Dec 2000.

[103] Hyun-Joon Shin, Mark C. Pierce, Daesung Lee, Hyejun Ra, Olav Solgaard, and Rebecca Richards-Kortum. Fiber-optic confocal microscope using a mems scanner and miniature objective lens. *Opt. Express*, 15(15):9113–9122, Jul 2007.

[104] Benjamin A Flusberg, Eric D Cocker, Wibool Piyawattanametha, Juergen C Jung, Eunice L M Cheung, and Mark J Schnitzer. Fiber-optic fluorescence imaging. 2(12):941–950.

[105] Arthur F. Gmitro and David Aziz. Confocal microscopy through a fiber-optic imaging bundle. *Opt. Lett.*, 18(8):565–567, Apr 1993.

[106] Tuqiang Xie, David Mukai, Shuguang Guo, Matthew Brenner, and Zhongping Chen. Fiber-optic-bundle-based optical coherence tomography. *Opt. Lett.*, 30(14):1803–1805, Jul 2005.

[107] Werner Göbel, Jason N. D. Kerr, Axel Nimmerjahn, and Fritjof Helmchen. Miniaturized two-photon microscope based on a flexible coherent fiber bundle and a gradient-index lens objective. *Opt. Lett.*, 29(21):2521–2523, Nov 2004.

[108] Kung-Bin Sung, Rebecca Richards-Kortum, Michele Follen, Anais Malpica, Chen Liang, and Michael R. Descour. Fiber optic confocal reflectance microscopy: a new real-time technique to view nuclear morphology in cervical squamous epithelium in vivo. *Opt. Express*, 11(24):3171–3181, Dec 2003.

[109] J.-H. Han and J. U. Kang. Effect of multimodal coupling in imaging micro-endoscopic fiber bundle on optical coherence tomography. *Applied Physics B*, 106(3):635–643, 2012.

[110] Xianpei Chen, Kristen L. Reichenbach, and Chris Xu. Experimental and theoretical analysis of core-to-core coupling on fiber bundle imaging. *Optics Express*, 16(26):21598, 2008-12-22.

[111] Joshua Anthony Udovich, Nathaniel D. Kirkpatrick, Angelique Kano, Anthony Tanbakuchi, Urs Utzinger, and Arthur F. Gmitro. Spectral background and transmission characteristics of fiber optic imaging bundles. *Applied Optics*, 47(25):4560, 2008.

[112] Rudolf Grimm, Matthias Weidemüller, and Yurii B. Ovchinnikov. Optical dipole traps for neutral atoms. In *Advances In Atomic, Molecular, and Optical Physics*, volume 42, pages 95–170. 2000.

[113] J. Kronjäger, C. Becker, M. Brinkmann, R. Walser, P. Navez, K. Bongs, and K. Sengstock. Evolution of a spinor condensate: Coherent dynamics, dephasing, and revivals. *Phys. Rev. A*, 72:063619, Dec 2005.

[114] Ming-Shien Chang, Qishu Qin, Wenxian Zhang, Li You, and Michael S. Chapman. Coherent spinor dynamics in a spin-1 Bose condensate. *Nature Physics*, 1(2):111–116, October 2005.

[115] J. Kronjäger, C. Becker, P. Navez, K. Bongs, and K. Sengstock. Magnetically tuned spin dynamics resonance. *Phys. Rev. Lett.*, 97:110404, Sep 2006.

[116] C. Frapolli, T. Zibold, A. Invernizzi, K. Jiménez-García, J. Dalibard, and F. Gerbier. Stepwise bose-einstein condensation in a spinor gas. *Phys. Rev. Lett.*, 119:050404, Aug 2017.

[117] D. M. Stamper-Kurn and W. Ketterle. *Spinor Condensates and Light Scattering from Bose-Einstein Condensates*, pages 139–217. Springer Berlin Heidelberg, Berlin, Heidelberg, 2001.

[118] Guillaume Lang and Emilia Witkowska. Thermodynamics of a spin-1 bose gas with fixed magnetization. *Phys. Rev. A*, 90:043609, Oct 2014.

[119] Nguyen Thanh Phuc, Yuki Kawaguchi, and Masahito Ueda. Effects of thermal and quantum fluctuations on the phase diagram of a spin-1 ^{87}rb bose-einstein condensate. *Phys. Rev. A*, 84:043645, Oct 2011.

[120] M. Köhl, M. J. Davis, C. W. Gardiner, T. W. Hänsch, and T. Esslinger. Growth of bose-einstein condensates from thermal vapor. *Phys. Rev. Lett.*, 88:080402, Feb 2002.

[121] H.-J. Miesner, D. M. Stamper-Kurn, M. R. Andrews, D. S. Durfee, S. Inouye, and W. Ketterle. Bosonic stimulation in the formation of a bose-einstein condensate. *Science*, 279(5353):1005–1007, 1998.

[122] Marek Tylutki, Lev P. Pitaevskii, Alessio Recati, and Sandro Stringari. Confinement and precession of vortex pairs in coherently coupled bose-einstein condensates. *Phys. Rev. A*, 93:043623, Apr 2016.

[123] Oren Lahav, Amir Itah, Alex Blumkin, Carmit Gordon, Shahar Rinott, Alona Zayats, and Jeff Steinhauer. Realization of a sonic black hole analog in a bose-einstein condensate. *Phys. Rev. Lett.*, 105:240401, Dec 2010.

[124] A. Recati, N. Pavloff, and I. Carusotto. Bogoliubov theory of acoustic hawking radiation in bose-einstein condensates. *Phys. Rev. A*, 80:043603, Oct 2009.